Technische Universität München
Fakultät für Mathematik
Lehrstuhl für Numerischen Methoden der Plasmaphysik

Max-Planck-Institut für Plasmaphysik

Scattering and reflection of microwave beams in fusion plasmas

Numerical analysis with semiclassical methods

Lorenzo Guidi

Vollständiger Abdruck der von der Fakultät für Mathematik der Technischen Universität München zur Erlangung des akademischen Grades eines

Doktors der Naturwissenschaften (dr. rer. nat.)

genehmigten Dissertation.

Vorsitzender:		Prof. Dr. Massimo Fornasier
Prüfende der Dissertation:	1.	Prof. Dr. Eric Sonnendrücker
	2.	Prof. Dr. Caroline Lasser *(schriftliche Beurteilung)*
	3.	Prof. Dr. Olivier Lafitte

Die Dissertation wurde am 17.01.2019 bei der Technischen Universität München eingereicht und durch die Fakultät für Mathematik am 07.05.2019 angenommen.

Max-Planck-Institut für Plasmaphysik
Abteilung Numerischen Methoden der Plasmaphysik

Technische Universität München

Scattering and reflection of microwave beams in fusion plasmas

Numerical analysis with semiclassical methods

Author: Lorenzo Guidi
Supervisor: Prof. Dr. Eric Sonnendrücker
Advisor: Dr. Omar Maj

Abstract

Microwave beams have a broad range of applications in nuclear fusion, and a rigorous mathematical modeling of their propagation in plasmas is of great interest. In the mathematical framework of semiclassical methods, recent progresses in both code development (the IPP code WKBeam) and theory (Hagedorn wave packets) open the possibility to address and finally solve two open problems: (I) the effects of plasma turbulence on wave beams and (II) the efficient numerical simulation of cut-off reflections.

Zusammenfassung

Mikrowellenstrahlung hat viele Anwendungen in der Kernfusion, und eine rigorose Modellierung ihrer Ausbreitung in Plasmen ist von großem Interesse. Im mathematischen Rahmen semiklassischer Methoden eröffnen die neuenten Fortschritte sowohl in der Codeentwicklung (IPP-Code WKBeam) als auch in der Theorie (Hagedorn-Wellenpakete) die Möglichkeit, zwei offene Probleme letztendlich zu lösen: (I) die Auswirkungen von Plasma-Turbulenzen auf die Strahlung und (II) die effiziente numerische Simulation von cut-off Reflexionen.

This work has been carried out within the framework of the EUROfusion Consortium and has received funding from the European Union's Horizon 2020 research and innovation programme under grant agreement 633053. The views and opinions expressed herein do not necessarily reflect those of the European Commission.

Structure of this work

This work is structured in three parts: Part 0 provides a general introduction to the treated topics, collocating them in the relevant applications and theory context. Part I and Part II are reasonably self-contained and they can be read independently. Each of the two parts has the same structure: Chapter 1 provides a heuristic introduction to the problem, Chapter 2 is dedicated to a revision of the mathematical techniques used, while Chapters 3 and 4 contain the theoretical and numerical results, respectively. The scheme below should be of help to the reader.

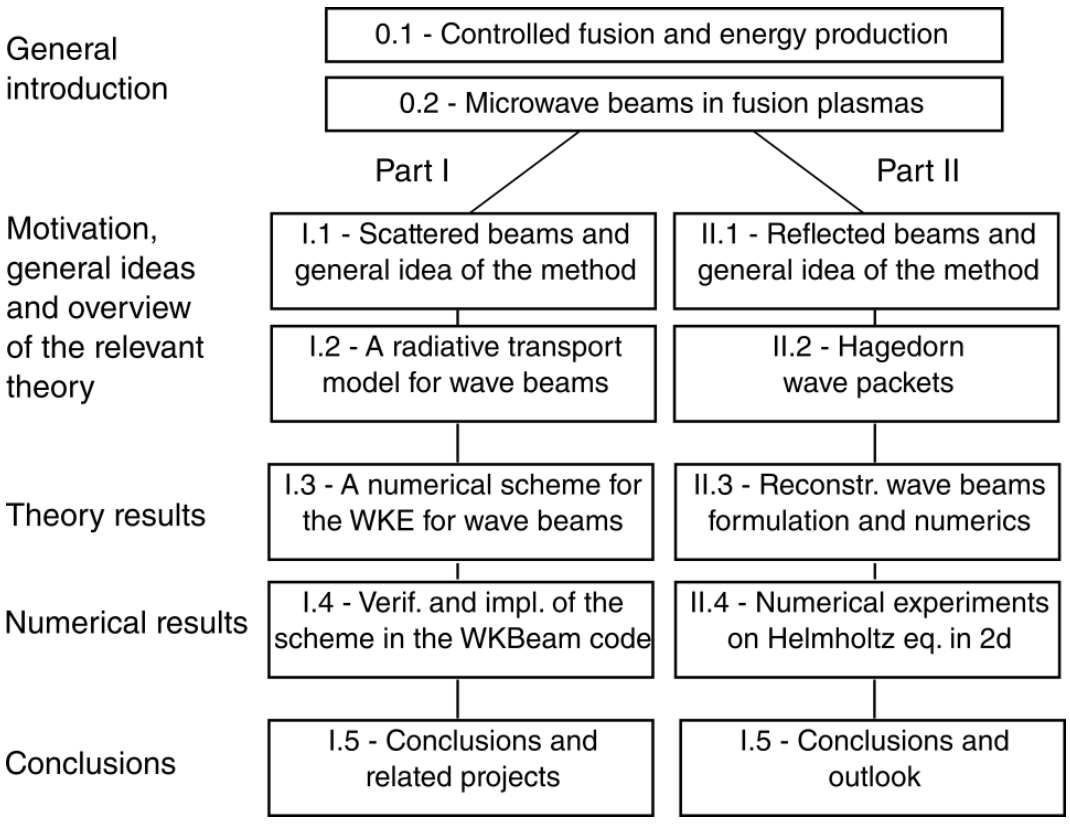

Contents

Part 0

Theory and applications: context of this work

0.1 Controlled fusion for energy production

One of the biggest challenges of our society is to confront the need of an increasing amount of usable energy, overcoming the limitations of today available sources. Figure 0.1.1 shows how fossil fuels (e.g., coal, oil) still by far provide the largest portion of the yearly energy production worldwide, and despite their constant growth in the last four decades "alternative" sources (e.g., wind, solar) did not affect this predominance.

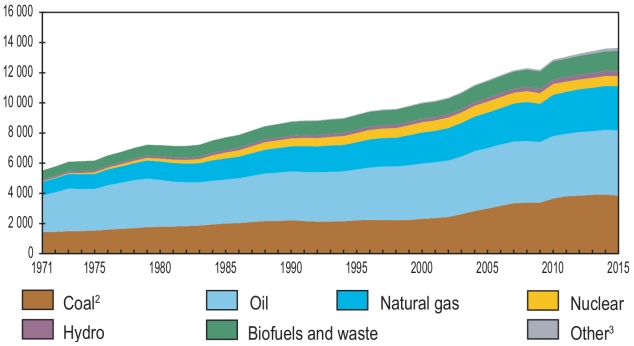

Figure 0.1.1: World total primary energy supply by fuel.
Graphics: International Energy Agency [32].

The problems related to fossil fuels are well known (limited availability, environmental damage), and major technological issues prevent renewable sources from playing a major role in the above picture. Nuclear energy based on fission reactions is also subject to discussions and criticism - an analysis of which is beyond the scope of the present work - mostly related to environmental (radioactive waste) and safety (rare but large impact accidents) issues.

Having these elements in mind, one could easily define a set of criteria that an ideal energy source should satisfy: large (virtually unlimited) availability, full control on the usability, low environmental impact, safety. None of the today available sources seems to fulfill all of the criteria, making the search of a new mean of energy production a fundamental challenge for our society. Controlled thermonuclear fusion appears to reasonably satisfy the above requirements, and for this reason its actual realization has been collecting the efforts of the scientific community since the 1950s, still offering today a series of open problems in different fields such as applied mathematics, physics and engineering. In order to understand the complexity of the problem a short introduction to the basic concepts of controlled fusion is given in this chapter, which will help collocating this work in the larger applicative context.

0.1.1 Nuclear fusion power

The fact that the fusion of the nuclei of light elements can lead to the release of large amounts of energy is a direct consequence of the mass-energy equivalence formula, provided that the product of the reaction has a mass smaller than the sum of the masses of the original elements. The acknowledgement of the actual presence of this process in stars dates back to the first half of last century, and it is at the origin of the idea of exploiting fusion reactions to produce energy.

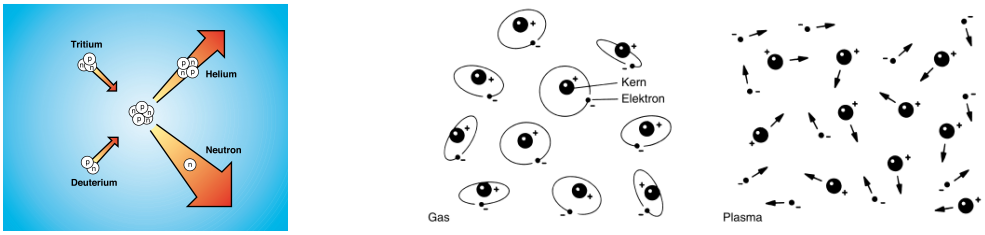

(a) (b)

Figure 0.1.2: (a) An example of D-T fusion reaction. (b) Representation of matter in the gas and plasma states in terms of organization of the atoms. *Graphics: IPP.*

An example of reaction is represented in Figure 0.1.2a, involving two iso-

topes of hydrogen (deuterium and tritium, D-T), whose nuclei recombine into an atom of helium-4, releasing a neutron which carries a large amount of energy. This reaction is the strongest candidate for future fusion power plants, due to the large cross-section, which makes fusion reactions more likely to happen. Moreover the fueling atoms are available in nature (deuterium) or producible in laboratory (tritium) in almost unlimited quantities [21]. In order to create the conditions favorable to the realization of such reaction though, matter needs to be in a specific state called plasma. Such state (see Figure 0.1.2b) is reached by ionization of a gas, meaning that the negatively-charged electrons of the atoms are stripped away from the positively-charged nuclei. The result is a globally neutral compound of free charged particles, in which the high energy of the particles wins over the electric forces that normally would prevent them from interacting, and fusion reactions are therefore possible. Matter in the state of plasma is generally not present on the Earth surface, due to the high temperatures required to reach such a state. Nevertheless, it is estimated that around 99% of the presently known matter in the universe is in the state of plasma, and plasmas are commonly produced artificially for a variety of applications (e.g., lasers, neon lights, plasma screens). In order to reach the conditions which trigger fusion reactions though, the temperatures and densities required are so high (see Figure 0.1.3a) that realizing them in a controlled way is highly challenging.

0.1.2 Magnetic confinement

The need for high temperatures comes from the necessity to overcome electric forces, while in order to maximize the likelihood of the nuclei interacting with each other triggering a fusion reaction, a relatively high density is required. Controlling on earth matter at temperatures of hundreds of millions degrees Celsius constitutes one of the main problems of achieving controlled fusion, but the electromagnetic properties of plasmas come to help: being constituted by charged particles, a plasma can be shaped without the need of a physical

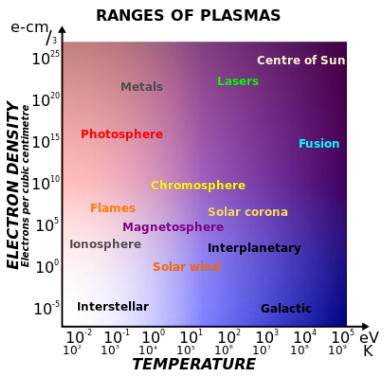

(a) Various astrophysical and laboratory plasmas. *Graphics: Wikipedia.*

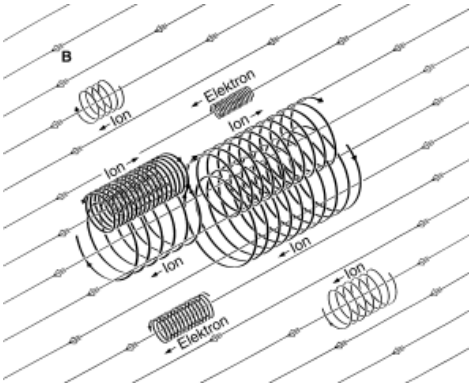

(b) Representation of charged particles in a magnetic field. *Graphics: IPP.*

Figure 0.1.3

container, immersing it instead in a strong-enough magnetic field. As illustrated in Figure 0.1.3b, in presence of a magnetic field the charged particles will move orbiting around the field lines, so that intuitively, if such lines are closed, our plasma will be confined in the region delimited by such lines. This basic idea is at the core of the presently most developed concepts of fusion devices, tokamaks and stellarators, which are characterized by different concepts of how to compensate the fact that - mostly due to drift forces that deviate the particles trajectories - simple circular magnetic field lines fail to effectively confine the plasma (see Figure 0.1.4).

Most of the existing experiments do not actually operate with fusion plasmas (e.g., deuterium-tritium), but are rather dedicated to generate and study the properties of a single-element (e.g., deuterium) plasma in temperature and density regimes that are comparable to those of a fusion reactor. In order to conduct such experiments huge amounts of energy are required, mostly for heating the plasma and generating the strong confinement magnetic fields. So far, none of the few actual fusion experiments conducted has reached the goal of producing more energy than what is needed to operate the machine. The tokamak ITER [34] - currently under construction as an international collaboration between China, EU, India, Japan, Korea, Russia and USA - should be able to achieve the goal of actually producing energy: a gain factor

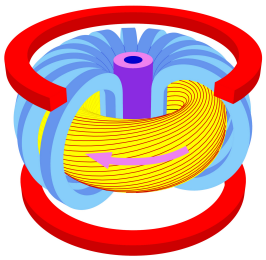

(a) In a tokamak the magnetic field lines generate a plasma characterized by nested magnetic flux surfaces, and such that the properties of the plasma on different poloidal sections are the same (axisymmetry). A toroidal current is generated in order to achieve confinement (pulsed operation).

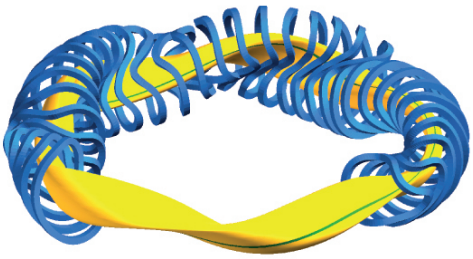

(b) In a stellarator magnetic confinement of the plasma is obtained without introducing any toroidal current (steady-state operation). As a consequence, strong constraints on the magnetic field geometry must be imposed in order to actually achieve confinement, and the axisymmetric structure is lost.

Figure 0.1.4: An example of (a) tokamak and (b) stellarator, the most diffused concepts of fusion devices nowadays. *Graphics: IPP.*

of 10 is foreseen, and in case of success the possibility of effectively using controlled nuclear fusion as a source of energy will be established.

In the meanwhile, there are still a number of physics phenomena taking place in the plasma whose understanding is crucial before taking further steps towards fusion experiments: experimental campaigns are extremely costly, and a theoretical understanding of such phenomena is more than just an entertaining exercise. There is a strong need for reliable mathematical models and fast numerical simulations of what goes on in a fusion device, and the variety of physics phenomena involved makes plasma physics and fusion research an ideal framework for the development of new mathematics and for the application of existing techniques to new problems. A full overview of such possibilities is out of the scope of the present work, which focuses on problems related to electromagnetic high-frequency waves propagation. In the next chapter such problems will be shortly presented, explaining their relevance to nuclear fusion and introducing their basic mathematical formulation.

0.2 Microwave beams in fusion plasmas

As mentioned in the previous chapter, a plasma basically consists of charged particles, and therefore it interacts with electromagnetic fields. A nuclear fusion experiment is characterized by a variety of these fields, which are either imposed externally (e.g., confinement field, electromagnetic heating sources etc.), or generated by the plasma itself. This corresponds to a great variety of wave phenomena within the plasma, whose mathematical modeling requires different techniques according to the different physics regimes. A comprehensive description of the "plasma wave zoo" is beyond the scope of this work, and one can refer to the classics on the subject like Brambilla [8], Stix [88] or Swanson [89]. This works focuses on electromagnetic waves which are:

- injected by an external source (wave guide / antenna system);
- in the *electron cyclotron* frequency range, i.e.,

$$\omega \approx \omega_{ce} = \frac{eB_0}{m_e c},$$

  so that the wave frequency ω is of the order of the electron cyclotron frequency ω_{ce}, given in terms of the electron charge e, the intensity of the confinement magnetic field B_0, the electron mass m_e and the speed of light in free-space c [6].

The main applications of these waves in fusion research are briefly presented, followed by a brief introduction to the relevant equations and the possible numerical approaches to their solution.

0.2.1 Short overview of the applications

Electron cyclotron waves have three main domains of application in fusion research:

1. **Resonant heating (ECRH).** ECRH exploits the fact that EC waves are absorbed at the electron cyclotron resonance, so that they transfer their energy to the electrons, which then heat the ions as well by collisions [6, 67]. Notice that electromagnetic radiation at lower frequencies can be used to directly heat the ions (ICRH).

2. **Current drive (ECCD).** ECCD is also based on the mechanism of resonant absorption, but the main goal is to deliver power at specific locations in the electron phase-space, in order to tailor a local electric current with the aim of suppressing local instabilities that arise during operations [31]. Several physics studies are dedicated to the understanding of this mechanism [104, 41, 106, 77, 36, and references therein], and the precision of the beam on its target is a key element of the whole machinery. The first part of this work is related to this application, as the main goal is to provide a method able to predict how the propagation through a turbulent plasma might spoil the beam structure and determine a loss of precision.

3. **Plasma diagnostics.** Several diagnostic tools used in fusion experiments in order to measure different quantities in the plasma [27] are based on EC emission. Reflectometry [51, 45, 14, 28, and references therein] is one of these: a wave beam is injected in the plasma, and gets reflected when it reaches the so called cut-off density. The reflected signal is then compared to the injected one, and important properties of the plasma (e.g., density, turbulence spectrum) can be deduced. Scanning over the wave frequency allows one to access the plasma at different radial positions, since waves with higher frequencies penetrate to regions of higher electron density. The second part of this work is related to this

type of applications, as an idea for a numerical method that efficiently reconstructs reflected beams near the cut-off is presented.

0.2.2 Formal mathematical description

In general terms high-frequency electromagnetic waves in a stationary medium can be described by means of an equation for the electric field of the form

$$P^\kappa(x, -\mathrm{i}\kappa^{-1}\nabla)E^\kappa(x) = 0, \quad x \in \Omega \subseteq \mathbb{R}^d,\ \kappa \gg 1, \tag{0.2.1}$$

where $E^\kappa : \Omega \to \mathbb{C}^m$ and the operator $P^\kappa = P^\kappa(x, N) \in C^{m\times m}$ is a symbol, i.e., a smooth function with all derivatives bounded by a polynomial in $N \in \mathbb{R}^d$. It is natural for the intended applications to consider the case of $d \geq 2$ and a domain of the form

$$\begin{aligned} \Omega &= \mathbb{R}_+ \times \mathbb{R}^{d-1}, \\ \Sigma &= \{(0, y) \mid y \in \mathbb{R}^{d-1}\}. \end{aligned} \tag{0.2.2}$$

By an abuse of notation points on Σ will always be denoted by y. On the hypersurface Σ - which typically represents an antenna / wave-guide system - the incident field

$$E^\kappa_{in}(x)|_\Sigma = E^\kappa_0(y) \tag{0.2.3}$$

is known from the experimental set-up, and in the applications the datum E^κ_0 is generally given in the form of a Gaussian beam (cf., Section 0.2.4).

From a mathematical point of view the condition (0.2.3) does not in general determine a unique solution of equation (0.2.1). Additional conditions will be provided for the specific cases treated in this work, depending on the solution method and application. More generally one can refer to the literature on scattering problems ([58] and references therein) or to works in microlocal analysis ([17] and references therein). The two special cases of (0.2.1) treated in this work are:

- In Part I, the wave equation

$$\frac{1}{\kappa^2}\nabla \times (\nabla \times E^\kappa) - \epsilon E^\kappa = 0, \quad x \in \Omega \subseteq \mathbb{R}^3 \; E^\kappa = E^\kappa(x) \in \mathbb{C}^3,$$

  is considered, where ϵ is an operator describing the medium. Electron cyclotron waves in a magnetically confined plasma can be fully described by means of an equation of this type, with $\epsilon = \epsilon(x, -\mathrm{i}\kappa^{-1}\nabla)$ an integro-differential operator.

- In Part II, the scalar Helmholtz equation

$$\frac{1}{\kappa^2}\Delta E^\kappa - V E^\kappa = 0, \quad x \in \Omega \subseteq \mathbb{R}^2 \; E^\kappa = E^\kappa(x) \in \mathbb{C},$$

  is considered, where $V = V(x)$ is a function accounting for the properties of the medium. This is a simplified model, and it generally provides a good test-case for new methods in wave propagation while still describing interesting physics.

A precise definition of the terms appearing in the equations will be given later in this work, at the moment of entering the details of each problem.

0.2.3 Different numerical approaches

In general analytic solutions for the problems introduced in the previous section cannot be found, especially if non-trivial geometries and physics phenomena are taken into account. Therefore, one needs to rely on numerical solutions, which need to be accurate and fast, as the goal is to be predictive with respect to unexplored experimental scenarios, or to be able to use the simulations to have a real-time control on ongoing experiments. Two main classes of methods can be identified, each with its advantages and limitations.

Full-wave methods

Numerical methods that rely on standard discretization techniques, like finite differences or finite elements, are often addressed in the plasma physics community as "full-wave". The full physics model is generally accounted for, by discretizing Maxwell's equations, which provide a complete description of electromagnetic phenomena. This can be done in different forms (in time or frequency domain) and in general if the discretization technique is chosen opportunely full-wave methods are able to reproduce accurately a solution of the problem and its conservation laws. Several techniques have been implemented in fusion-dedicated codes [37, 16, 1, 76, and references therein], which account for the relevant geometry and plasma parameters. Usually full-wave methods rely on:

1. Yee scheme [105] for Maxwell's equations. This scheme is based on a staggered grid, and it is an energy-preserving, variational multi-symplectic scheme [87].

2. A suitable coupling with the current equation coming from the cold-plasma model [15].

Direct discretization approaches present some limitations. In fact for typical scenarios of electron cyclotron waves in fusion plasmas on has to deal with:

- Short wavelengths, typically of the order of the millimeter;
- Large propagation domains, up to the order of the meter.
- Integral operators with highly oscillatory kernels (arising in the kinetic theory of plasma waves), e.g., the operator $\epsilon = \epsilon(x, -\mathrm{i}\kappa^{-1}\nabla)$ mentioned in Section 0.2.2.

The first two points imply that that a highly resolved large grid is necessary in order to include the short scales. Moreover, no viable numerical method is known that allows to solve the third point, so that full-wave methods cannot account properly for resonant absorption. Nevertheless, for some problems

standard discretization is still the only (or the most) reliable method, and more in general full-wave codes provide a solid tool for verification of other numerical methods. This is particularly the case for diagnostic applications.

Semiclassical methods

Wave propagation problems in plasmas (but not only) are often treated with another class of methods, namely, semiclassical methods [62, 20, 68, 101, 65, and references therein]. The philosophy of this approach is to take advantage of the presence of multiple scales in the physics model, which is a limitation for full-wave methods: if the medium is slowly varying with respect to the wavelength, one can identify the large "semiclassical" parameter κ, given by

$$\kappa = \frac{\omega L}{c} \gg 1, \tag{0.2.4}$$

where ω is the wave frequency, c is the speed of light in free-space and L denotes the (large) typical scale of variation of the medium. The typical work-flow then will be:

1. Make an *ansatz* on the solution as an asymptotic series [7] in (integers or fractional) powers of the parameter κ;

2. Plug the *ansatz* into the original problem, and derive a new set of equations by separating the terms corresponding to different powers of κ;

3. Solve (a subset of) the new set of equations in order to reconstruct an approximated solution of the original problem with a reminder of order κ^q, for some $q \in \mathbb{Q}$ which depends on the specific method.

The idea is that the new set of equations is simpler and faster to solve than the original problem, so that at the price of an approximation error, a gain in terms of performance is obtained. The formulation of the *ansatz* should take into account the physics that one wants to describe, and the same applies to the order at which one decides to truncate the asymptotic series. The presentation here is extremely simplified, and one can refer to the textbook by Martinez [52]

for a general treatment, and to [38, 54, 2, 95, and references therein] for a more method-specific approach. In order to better understand the general idea, an example of application of ray-tracing to a simple model is presented here.

Example 0.2.3.1 (Ray-tracing for Helmholtz in a linear medium)**.** *Consider the 2d problem*

$$\frac{1}{\kappa^2}\Delta u^\kappa(x) + (1 - x_1)u^\kappa(x) = 0, \quad x = (x_1, y) \in \mathbb{R}_+ \times \mathbb{R},$$

and assume that the wave field is known on $\Sigma = \{(0, y),\ y \in \mathbb{R}\}$*, i.e.,*

$$u^\kappa(0, y) = u_0^\kappa(y).$$

The boundary datum u_0^κ *is taken Gaussian, namely,*

$$u_0^\kappa(y) = A_0 \mathrm{e}^{-\left(\frac{y}{w_0}\right)^2 + \mathrm{i}\kappa\frac{y^2}{2R}}, \quad A_0, w_0 > 0,\ R \neq 0.$$

The geometrical optics ansatz *corresponds to look for a solution of the form*

$$u^\kappa(x) = a^\kappa(x)\mathrm{e}^{\mathrm{i}\kappa\phi(x)}, \quad a^\kappa(x) \sim \sum_{j\geq 0} \kappa^{-j} a_j(x),$$

so that the amplitude a^κ *is given by an asymptotic series (cf., [52, 7] as described above. By substitution in the equation, and separation by powers of* κ *one obtains the following recursive set of equations for the phase* ϕ *and the amplitudes* a_j*:*

$$\begin{aligned} 1 - x_1 - |\nabla\phi|^2 = 0, &\qquad \mathcal{O}(1), \\ 2\nabla a_0 \cdot \nabla\phi + a_0\Delta\phi = 0, &\qquad \mathcal{O}(\kappa^{-1}), \\ 2\mathrm{i}\nabla a_j \cdot \nabla\phi + a_j\Delta\phi = -\Delta a_{j-1}, &\qquad \mathcal{O}(\kappa^{-j}), j \geq 2. \end{aligned}$$

Usually the first two equations are solved, giving an approximation of the solution with an error of $\mathcal{O}(\kappa^{-1})$*.*

The first equation - called eikonal *equation - gives the phase* ϕ*. One can*

define $N = \nabla\phi$ *and* $H = N^2 - x_1 - 1$*, and use the method of characteristics to solve it. Specifically one solves the equations*

$$\dot{x}(t) = \partial_N H(x(t), N(t)), \quad \dot{N}(t) = -\partial_x H(x(t), N(t)), \quad H = 0,$$

and then reconstruct the phase by means of the line integral

$$\phi(x(t)) = \phi(x(0)) + \int_0^t N(s)dx(s).$$

The initial condition for the position $x(0)$ *is taken on the boundary, while that for the momentum* $N(0)$ *is deduced by the phase of the boundary condition and the dispersion relation* $N^2 = 1$ *(plus some additional boundary condition not specified here that selects the positive branch of the square root), so that for the considered case*

$$N(0) = \begin{pmatrix} \sqrt{1 - y_0^2/R^2} \\ y_0/R \end{pmatrix}, \quad x(0) = \begin{pmatrix} 0 \\ y_0 \end{pmatrix},$$

from which one can compute

$$N(t) = \begin{pmatrix} \sqrt{1 - y_0^2/R^2} - t \\ y_0/R \end{pmatrix}, \quad x(t) = \begin{pmatrix} 2t\sqrt{1 - y_0^2/R^2} - t^2 \\ y_0 + 2ty_0/R) \end{pmatrix}.$$

The trajectories in position space $x(t)$*, called* rays*, are parabolas that intersect each other, so that they cannot be inverted and the phase cannot be reconstructed in the whole domain (cf., Figure 0.2.1a). In the case of a homogeneous medium (e.g., no* x_1 *multiplication in the equation),* $N(t) = N(0)$ *for all* $t > 0$*, and the rays are straight lines, which still intersect if* $1/R \neq 0$ *(focused beam, cf., Figure 0.2.1b). In the simple case of zero initial phase (*$1/R = 0$*) the rays are parallel lines, and the amplitude can be computed in the whole space, giving solution is*

$$u_{GO}^{\kappa}(x) = u_0^{\kappa}(y)\mathrm{e}^{\mathrm{i}\kappa x_1} + \mathcal{O}(\kappa^{-1}).$$

Even in this very simple case there is a substantial difference with respect to

the exact solution (cf., Section II.3.1), which translates into the fact that the GO solution only describes the "near-field", i.e., the error grows linearly with x_1, for large x_1/w_0.

Already for a simple problem ray-tracing does not reproduce correctly the exact solution, but more sophisticated techniques can be derived in the same spirit, in order to build more suitable approximations that include more physics. For what concerns the applications of interest for this work, two main issues arise for what concerns standard semiclassical methods (e.g., ray tracing, complex WKB, beam tracing):

1. *Smoothness of the medium.* The assumption of the medium to be slowly varying, or equivalently of L to be large, is not always met in the envisaged applications scenarios: a turbulent plasma might develop local structures whose size is comparable to the wavelength, breaking the limits of validity of the asymptotic expansion.

2. *Caustics.* Physics phenomena like focuses and turning points constitute singularities for most semiclassical methods (see Figure 0.2.1). In Example 0.2.3.1 caustics correspond to the non-invertibility of the characteristic flow.

0.2.4 Diffracting wave beam solutions

For focused beams diffraction effects can be accounted for by several methods. Wave beam solutions are of particular interest for what concerns the considered wave problem. A wave beam is a monochromatic wave field localized around a certain path, and a brief description of such solutions is given here, together with the relevant boundary conditions.

Under certain assumptions on the medium - which will be clarified for the specific cases treated later on in this work - paraxial techniques [69, 46, 62, 54, 49, and reference therein] can be used in order to obtain asymptotic solutions

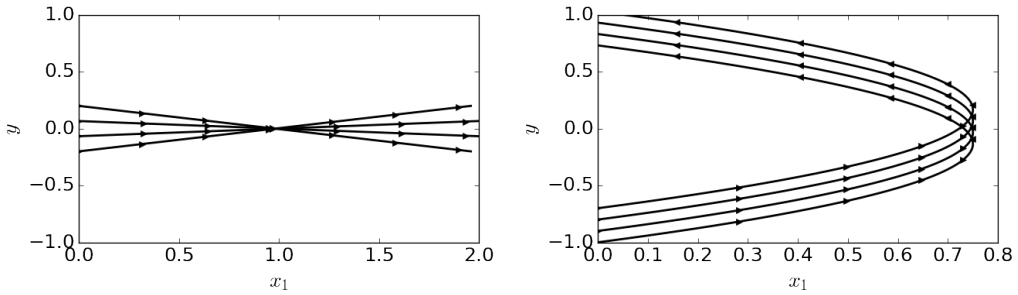

(a) (b)

Figure 0.2.1: (a) In the case considered in Example 0.2.3.1, a non-zero phase at the boundary determines rays which intersect one another (focus). Therefore, the phase cannot be reconstructed univocally at each point in space. (b) In the case of a linear medium (cf., Section II.3.2), the rays define parabolic trajectories. In the region near the turning point the wave field cannot be reconstructed.

in the limit $\kappa \to +\infty$ for the wave field of a beam in the form

$$E^\kappa(\omega, x) = \sum_{\alpha \in M} e_\alpha\big(x, \nabla S_\alpha(x)\big) A_\alpha(x) e^{\mathrm{i}\kappa S_\alpha(x) - \kappa\phi_\alpha(x)} + O(1/\sqrt{\kappa}), \qquad (0.2.5)$$

where for each component (or mode) α, the polarization is given by the corresponding eigenvector $e_\alpha = e_\alpha(x, N) \in \mathbb{C}^m$, $A_\alpha = A_\alpha(x)$ is the electric field scalar amplitude, $S_\alpha = S_\alpha(x)$ is the phase, and $\phi_\alpha = \phi_\alpha(x) \geq 0$ is a non-negative function which describes the power distribution in the beam cross-section. Specifically, the wave field defined by equation (0.2.5) is exponentially small where $\phi_\alpha > 0$, and thus concentrates near the zero-level set $\phi_\alpha = 0$, in the limit as $\kappa \to +\infty$. One obtains that the zero-level set of ϕ_α is a curve $x = x_\alpha(\tau)$ determined together with $N_\alpha(\tau) = \nabla S_\alpha\big(x_\alpha(\tau)\big)$ by Hamilton's equation of geometric optics (ray equations),

$$\frac{dx_\alpha}{d\tau} = \frac{\partial H_\alpha}{\partial N}, \quad \frac{dN_\alpha}{d\tau} = -\frac{\partial H_\alpha}{\partial x}, \quad H_\alpha(x_\alpha, N_\alpha) = 0, \qquad (0.2.6)$$

where the geometrical-optics Hamiltonian $H_\alpha = H_\alpha(x, N)$ is defined for $(x, N) \in \Omega \times \mathbb{R}^d$ and depends on the considered wave operator. The curve $x = x_\alpha(\tau)$ in

the spatial domain Ω is called reference ray of the beam. Around the reference ray the complex phase $\psi_\alpha = S_\alpha + i\phi_\alpha$ is determined, in the form

$$\psi_\alpha(x) = \sigma_\alpha(\tau) + N_\alpha(\tau) \cdot \tilde{x} + +\frac{1}{2}\tilde{x} \cdot \Psi_\alpha(\tau)\tilde{x},$$

where $\tilde{x} = x - x_\alpha(\tau)$ is usually chosen orthogonal to $dx_\alpha/d\tau$; ordinary differential equations for real-valued phase $\sigma_\alpha(\tau)$, the symmetric matrix $\Psi_\alpha(\tau)$, and the amplitude $a_\alpha(\tau) = A_\alpha\big(x_\alpha(\tau)\big)$ are solved together with rays equations (0.2.6). The solution of such ordinary differential equations is sufficient to reconstruct the beam wave-field within an error of $\mathcal{O}(1/\sqrt{\kappa})$ via (0.2.5).

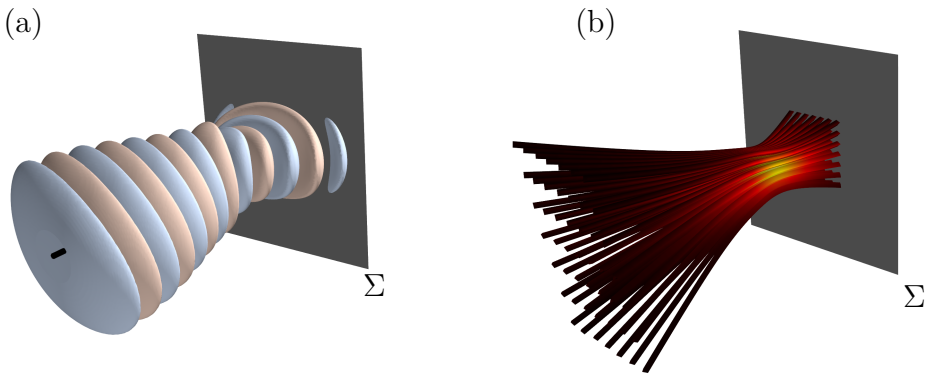

Figure 0.2.2: Example of wave beam in 3d, reconstructed according to equation (0.2.5) in free space. Panel (a) displays two contours of the wave field (at ±0.3 of the launched peak amplitude). The beam has an elliptical cross-section and curved phase fronts with misaligned axes of curvature, with consequent rotation of the cross-section (astigmatism). For the same beam, panel (b) shows energy-flux lines, that define a twisted flux tube for the wave energy.

As mentioned before, typically from the experimental setup the electric field is known on a plane $\Sigma \subset \mathbb{R}^3$. Physically Σ represents a mirror in the waveguide system which launches the beam, and the Poynting flux (energy flux)

on Σ is such that the beam in injected into one of the two half-spaces defined by the plane Σ. The phase and amplitude of the electric field yields the initial conditions $x_\alpha(0)$, $\sigma_\alpha(0)$, $\Psi_\alpha(0)$, and $a_\alpha(0)$, if $\tau = 0$ on Σ. The phase of the initial condition also provides the component of $N_\alpha(0)$ parallel to the launching plane Σ, and using the dispersion relation $H_\alpha(x_\alpha, N_\alpha) = 0$ and the Poynting flux direction one reconstructs the full vector $N_\alpha(0)$.

Figure 0.2.2 gives a representation of a Gaussian beam launched from a plane Σ in free space.

In general the wave field (0.2.5) does not belong to $L^2(\mathbb{R}^d)$, i.e., beams are not finite-energy solutions. However, the restriction of the beam to a plane orthogonal to the trajectory does belong to $L^2(\mathbb{R}^{d-1})$. Physically a beam represents a steady injection of waves from some external source; the energy flux is finite and bounded along the propagation path of the beam. This type of solutions are successfully employed on modeling heating beams in fusion devices [66, 20], retaining diffraction effects and focusing. Nevertheless, the following limitations still hold:

I. In presence of short-scale density fluctuations, existing methods are not applicable. The effect of such turbulent structures on the wave beam is of great interest for the applications [96], and in Part I a method for this problem is presented, based on a statistical approach.

II. For what concerns turning points, beam tracing methods fail in general (see Section II.1.2 for more details), and the existing unfolding techniques [18, 53] are difficult to apply in practice. Part II of this work is dedicated to the derivation and implementation of a method for cut-off reflections which is able to reconstruct the wave field near the turning point.

Part I

Numerical calculation of the Wigner measure for wave beams in turbulent plasmas

I.1 Scattered beams and general idea of the method

In most applications of high-frequency electromagnetic waves in fusion plasmas (cf., Chapter 0.2) it is crucial that the energy is deposited with extreme precision at its target. This means that any factor that could spoil the beam structure must be carefully taken into account, in order to prevent large amounts of energy from being deposited in undesired regions, with all the possible direct and indirect detrimental consequences for the plasma stability or the machine components.

Fluctuations of the plasma electron density are among the factors that may determine substantial modifications of the wave beam. In the last few years the efforts of the scientific community to model this effect have grown, and a variety of models and numerical tools have been developed [4, 64, 90, 40, 70, 33]. In fact for the new generation of tokamaks (e.g., ITER) density fluctuations seem to possibly determine important changes of the beam parameters (e.g., the beam width [96]).

An accurate and efficient numerical simulation of the phenomenon under physically relevant conditions cannot be achieved by existing beam-tracing methods [65, and references therein]. On the side of standard discretization techniques for Maxwell equations (e.g., finite differences, finite elements), the number of wavelengths to resolve in the physical domain is a major computational obstacle, while fundamental assumptions on which most of semiclassical methods rely (e.g., ray tracing, beam tracing), are not met in many scenarios relevant for the applications.

I.1.1 Presentation of the problem

Figure I.1.1a helps visualizing what the effect of density fluctuations on a wave beam could be: the wave field, originated on the right-hand side, propagates towards the left-hand side, and gets scattered by a turbulent layer, which one can think of as characterized by a number of density blobs.

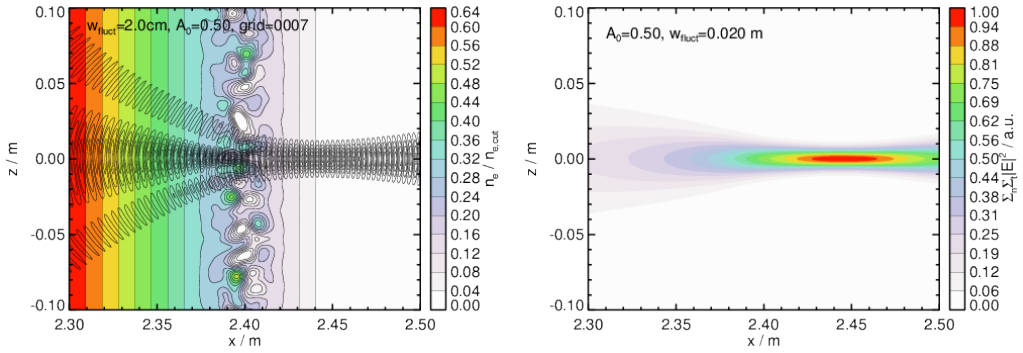

(a) (b)

Figure I.1.1: FDTD simulation of a wave beam in a plasma, in presence of fluctuations of the electron density, with the full-wave code IPF-FDMC [39]. (a) A wave beam is launched from the right-hand side through a medium characterized by the presence of density fluctuations localized in a strip. (b) Averaged wave beam, where the average was performed on $\sim 10^3$ independent samples of the type of (a).

The actual picture is more complex, as the turbulent structures evolve in time, so that in principle the dynamics of the medium should be coupled to that of the wave field. This complexity is generally avoided though, by means of some (physically motivated) assumptions that can be expressed synthetically by the following inequalities:

$$\tau_p = l/c \ll \tau_c \ll \tau_{obs}, \tag{I.1.1}$$

where τ_p is the propagation time of the wave in the domain of interest (whose size is denoted by l), τ_c denotes the correlation time of turbulence, and τ_{obs} is the time window of experimental observation when the beam is active. The

first inequality resumes what is typically called "frozen turbulence approximation", and implies that the wave propagates fast enough from the antenna not to see any variation in the medium. As for the second inequality, it basically means that the wave beam lives in the medium long enough that the effect of a single turbulence snapshot is not representative of the whole experiment duration. Intermittent events like the one represented in Figure I.1.1a might still be relevant for some applications, but the average effect shown in Figure I.1.1b provides more interesting information for ECCD and ECRH applications: several snapshots similar to that in Figure I.1.1a were generated, at a time distance from one another greater than τ_c, so that they can be considered mutually independent, and the average beam was computed. In this way, the (physical) time-evolving medium is treated (mathematically) as a random medium, and what in principle should have been a time average is replaced by an ensemble average over several independent realizations.

In this context the standard discretization techniques do not appear as the ideal method to compute the average beam, as the already high computational cost of one simulation should be multiplied by a number of realizations large enough for it to be statistically significant (typically, about 10^3). This would not be an issue for existing semiclassical methods (e.g., beam tracing, complex geometrical optics), whose computational cost is way lower. Such methods though are not applicable to the case of short-scale fluctuations (namely, of the same order of magnitude as the wavelength), which are indeed possible in the realistic scenarios. Wave propagation in random media can be successfully described by means of radiative transport models [35, 56, 75], where the statistics of the medium is accounted for directly in the equation for the wave field.

I.1.2 Stochastic trajectories

In this section the general idea of this Part is presented in a heuristic way, in order to provide a visual understanding of the concepts formalized in the

following chapters. As mentioned before, radiative transport models are commonly used to describe wave propagation in random media. In general terms, the idea is to derive an equation for the average wave field in phase-space. Assuming the random medium to be characterized by stochastic perturbations of an equilibrium, the resulting equation will consists in three blocks, describing respectively:

(i) the transport of the wave field in the unperturbed medium;

(ii) the effect of the random perturbations on the wave field;

(iii) (weak) dissipation due to resonant absorption.

In general the wave field has multiple components (modes), and the random perturbations (turbulence) modify it in two ways:

1. by changing the momentum of each mode, which might result in a *broadening* of the wave beam;

2. by coupling the different modes, with possible energy exchange among them. This is called here *cross-polarization scattering*.

Both effects can be particularly detrimental for the intended applications, as broadening reflects in a loss of localization in the power deposition, and cross-polarization scattering might result in a loss of energy from the desired mode. In order to facilitate the qualitative understanding of the proposed method, the case of a scalar field in a non-dissipative medium is considered in the discussion that follows. The main result of this Part though is obtained for the general case of the multi-component field, and accounts for weak dissipation (cf., Chapter I.3).

Quiet medium

In absence of the stochastic perturbation (quiet medium), the model roughly described above reduces to an equation in phase-space describing the transport of the wave field energy density. The field can be reconstructed by opportunely

tracing a number of "rays", which are trajectories obtained by solving certain deterministic ODEs (cf., Figure I.1.2).

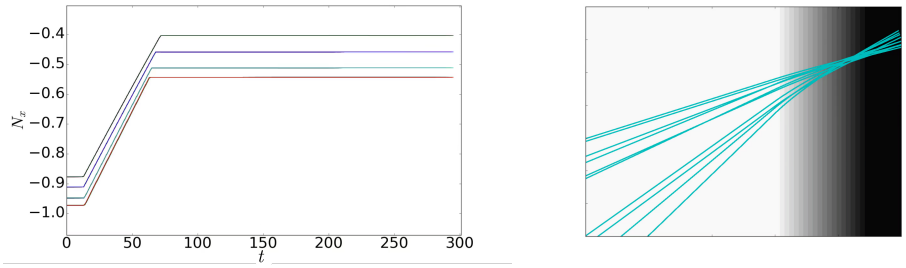

(a) (b)

Figure I.1.2: Example of deterministic rays. The momentum N_x (top) evolves in time following the dynamics described by standard ODEs. The projection of the rays in the physical 2d-space (bottom) is only affected by the quiet medium (background gradient).

Random medium

In presence of perturbations of the medium, Monte-Carlo methods offer an appropriate tool to solve the problem (cf., [43]). The method proposed here consists in a representation of the field in terms of a number of phase-space "particles", which are initialized by a suitable sampling and whose dynamics is described in terms of a stochastic process (cf., Figure I.1.3). The stochastic variables will represent the momentum and the mode of the particle.

For the derivation of a radiative transport model for wave beams one can refer to [101, 102], where a solution in the case of a scalar wave field is also presented. For the case of multiple modes, no rigorously derived numerical scheme has been developed yet. To this purpose, the following steps will be undertaken in this work:

- definition of a suitable stochastic process for the multiple-modes problem;
- construction of a Monte-Carlo scheme based on the stochastic process.

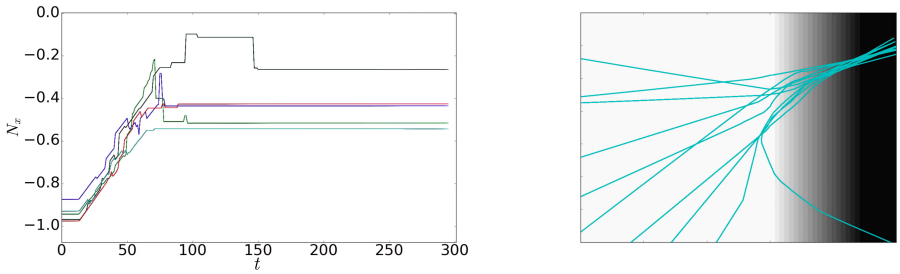

(a) (b)

Figure I.1.3: Example of stochastic particles. The momentum N_x (top) evolves in time following the dynamics described by a stochastic process. The projection in the physical 2d-space (bottom) is affected by the random perturbations (not represented) of the quiet medium (background gradient).

The first point is the main result of this work, and will be addressed in Chapter I.3, followed by the definition and tests of the numerical scheme in Chapter I.4. At last, in Section I.4.2 the implementation of the scheme in a code for realistic simulations is presented. Before presenting the results an overview of the radiative transport model for waves in plasmas derived by Weber [101] is given in Chapter I.2.

I.2 A radiative transport model for wave beams

Linear electromagnetic waves in dispersive stationary media are described by Maxwell's equations in the frequency domain, which can be reduced to a second-order equation for the wave electric field of the form of 0.2.1, i.e.,

$$\nabla \times (\nabla \times E^\kappa)(\omega, x) - \kappa^2 \mathrm{Op}^\kappa(\varepsilon^\kappa(\omega, \cdot))E^\kappa(\omega, x) = 0, \qquad \text{(I.2.1)}$$

equipped with suitable boundary conditions. In equation (I.2.1) spatial coordinates $x \in \mathbb{R}^d$, $d = 3$, are normalized to the scale L of the medium inhomogeneity, $\kappa = \omega L/c \gg 1$ is a large parameter, $\omega > 0$ is the frequency and c is the speed of light in free space. The unknown $E^\kappa = E^\kappa(\omega, x)$ is the electric field Fourier-transformed in time and depends on the large parameter κ through the equation. The dielectric operator $\mathrm{Op}^\kappa(\varepsilon^\kappa(\omega, \cdot))$ accounts for the properties of the medium. It is assumed to be the pseudo-differential operator [92, 52] obtained by Weyl quantization of the matrix-valued symbol $\varepsilon^\kappa = \big(\varepsilon^\kappa_{ij}(\omega, x, N)\big)$, which is a function of frequency ω, position x, and refractive index vector N; the latter plays the role of the coordinate dual to x in phase space and is defined so that $(\omega/c)N$ is the wave vector. The matrix-valued function $\varepsilon^\kappa(\omega, \cdot)$ is assumed to be a symbol [52] in the sense that $\varepsilon^\kappa(\omega, \cdot)$ belongs to C^∞ and is bounded by a polynomial in N together with all its derivatives. The Weyl quantization of a matrix-valued symbol A with semiclassical parameter $1/\kappa$ is the operator $\mathrm{Op}^\kappa(A)$ acting on smooth rapidly decreasing vector-valued

functions $u = u(x)$ as

$$\mathrm{Op}^\kappa(A)u(x) = \Big(\frac{\kappa}{2\pi}\Big)^d \int \mathrm{e}^{\mathrm{i}\kappa(x-x')\cdot N} A\big(\tfrac{x+x'}{2}, N\big)u(x')dx'dN.$$

The symbol ε^κ, in particular, is referred to as dielectric tensor in the physics literature. When $\varepsilon^\kappa(\omega, x, N)$ depends on N in a non-trivial way, the corresponding operator is non-local and the medium is said to be spatially non-dispersive. The use of Weyl symbol calculus for electromagnetic waves in plasmas was initially proposed by Kaufman and McDonald [57, 55].

Equation (I.2.1), divided by κ^2, can be written in terms of pseudo-differential operators as

$$\mathrm{Op}^\kappa(D^\kappa(\omega, \cdot))E^\kappa(\omega, x) = 0, \tag{I.2.2}$$

with Weyl symbol

$$D^\kappa(\omega, x, N) = N^2\mathbb{I} - N \otimes N - \varepsilon^\kappa(\omega, x, N), \tag{I.2.3}$$

where $\mathbb{I}$ is the identity matrix.

In presence of turbulent fluctuations, the medium can no longer be considered stationary and equation (I.2.1) does not apply. Nonetheless, as introduced heuristically in Chapter I.1, in a statistical representation of turbulence time-evolving fluctuations are replaced by a time-independent random field, thus recovering equation (I.2.1) with dielectric tensor of the form

$$\varepsilon^\kappa(\omega, x, N) = \varepsilon_0(x, N) + \frac{1}{\sqrt{\kappa}}\eta(x)\delta n(x) + \frac{\mathrm{i}}{\kappa}\varepsilon_1(x, N), \tag{I.2.4}$$

where $\varepsilon_0, \varepsilon_1$ are smooth Hermitian matrices, η is a smooth matrix-valued function depending only on frequency and position, and δn is a random field. All matrices ε_0, ε_1 and η in general have a residual dependence on the frequency ω which is implied in the notation, but are independent of the large parameter κ. One should notice the typical scaling $\propto 1/\sqrt{\kappa}$ of the random perturbation [75]. We have assumed that η is independent on N, i.e., the random perturbation is spatially non-dispersive: this is in general a restrictive assumption, but it is

sufficient for the envisaged applications and greatly simplifies the derivations [56]. The first-order term is anti-Hermitian and accounts for weak dispersive absorption.

I.2.1 Separation of the dispersion manifolds

With (I.2.3) and (I.2.4), the leading order term in D^κ as $\kappa \to +\infty$ amounts to

$$D_0(x, N) = N^2\mathbb{I} - N \otimes N - \varepsilon_0(x, N), \tag{I.2.5}$$

which is referred to as the semiclassical principal symbol of the operator (or dispersion tensor in the physics literature). It is a Hermitian matrix and thus it can be diagonalized pointwise,

$$D_0(x, N)e_\alpha(x, N) = H_\alpha(x, N)e_\alpha(x, N), \tag{I.2.6}$$

with real eigenvalues $H_\alpha(x, N)$ and complex unit eigenvectors $e_\alpha(x, N)$ labeled by Greek index $\alpha \in \{1, \dots, d\}$. The characteristic variety of equation (I.2.1) is defined as

$$\mathcal{C} = \{(x, N) \in \mathbb{R}^d \times \mathbb{R}^d \mid \det D_0(x, N) = 0\}, \tag{I.2.7}$$

and with plasma physics applications in mind, the following is assumed:

Assumption I.1. *The characteristic variety of equation (I.2.1) is not empty and*

$$\mathcal{C}_\alpha = \{(x, N) \in \mathbb{R}^d \times \mathbb{R}^d \ : \ H_\alpha(x, N) = 0\},$$

is either an empty set or a smooth co-dimension-one surface in $\mathbb{R}^d \times (\mathbb{R}^d \setminus \{0\})$. *The set of indices* α *for which* $\mathcal{C}_\alpha \neq \emptyset$ *is denoted by* M *and the surfaces* $\mathcal{C}_\alpha$ *are well separated, i.e.,*

$$\big|H_\alpha(x, N) - H_\beta(x, N)\big| \geq c_{\alpha,\beta}, \quad \alpha, \beta \in M, \quad \alpha \neq \beta,$$

for strictly positive constants $c_{\alpha,\beta} > 0$.

The fact that $\det D_0$ vanishes ensures the existence of propagative wave modes labeled by $\alpha \in M$, and the surface $\mathcal{C}_\alpha$ represents the dispersion manifold of the mode $\alpha \in M$. Notice that since the characteristic variety is non-empty, there is at least one index in M.

Assumption I.1 implies that all eigenvalues H_α for $\alpha \in M$ are simple and isolated. Hence the eigenprojectors

$$\pi_\alpha(x, N) = e_\alpha(x, N) e_\alpha(x, N)^*$$

and the eigenvalues H_α depend smoothly on (x, N) [72, Chapter II, sec. 1].

Physically the separation of the eigenvalues excludes the possibility of linear mode conversion [95]. Even though, as mentioned in Chapter I.1, some other coupling of the modes will be introduced as a consequence of the medium perturbations, this coupling (cross-polarization scattering) should not be confused with mode conversion. This is a strong assumption which might limit some applications of the radiative transport model, but this will not be addressed in this work.

I.2.2 Wigner measure in the semiclassical limit

In a quiet medium ($\delta n = 0$) and under assumption I.1, paraxial techniques can be used in order to compute a wave beam solution (0.2.5) of equations (I.2.2)-(I.2.4), as described in Section 0.2.4.

In general though, a solution of equations (I.2.2)-(I.2.4) amounts to a random electric field $E = E^\kappa(\omega, x)$ since the equation contains the random coefficient δn. In order to treat this term opportunely, the statistically averaged Wigner function of the field is introduced, namely,

$$W^\kappa(\omega, x, N) = \int \mathrm{e}^{-\mathrm{i}\kappa N\cdot s} \mathbb{E}\Big[E^\kappa\Big(\omega, x + \frac{s}{2}\Big) E^\kappa\Big(\omega, x - \frac{s}{2}\Big)^*\Big] ds. \tag{I.2.8}$$

Apart from the presence of the expectation-value operator $\mathbb{E}$, this is the Wigner

transform (as defined for instance by Gérard et al. [22]) applied to the electric field. Notice that the Wigner transform is invertible, therefore the self-correlation of the electric field can be computed, and thus the average electric energy density, from the knowledge of the Wigner matrix W.

On following Karal, Keller and McDonald [35, 56], a *formal* semiclassical expansion of the Wigner function is obtained in the form (cf. Weber et al. [102] for a sketch of the derivation)

$$W^{\kappa}(\omega, x, N) = \sum_{\alpha \in M} w_{\alpha}(x, N)\pi_{\alpha}(x, N) + O(\kappa^{-1}). \tag{I.2.9}$$

The leading order term is then diagonal on the basis of the polarization eigenprojectors π_{α}, which is the basis that diagonalizes the operator D_0 (cf., equation I.2.6). The sum (I.2.9) spans only the indices that belong to M, i.e., that corresponds to a propagation mode, cf. section I.2.1. In general the entries of the Wigner matrices are tempered distributions [22], but is is sufficient to restrict to cases in which the diagonal entries w_{α} can be identified with measures. The measure corresponding to the distribution w_{α} will be denoted by $w_{\alpha}(dx, dN)$ (the dependence on frequency of w_{α} is implied). An equation for the measures w_{α} can be derived, called wave kinetic equation:

$$\begin{cases} \{H_{\alpha}, w_{\alpha}\} = -2\gamma_{\alpha} w_{\alpha} + \sum\nolimits_{\beta} \mathcal{S}_{\alpha\beta}(w), \\ H_{\alpha} w_{\alpha} = 0, \end{cases} \tag{I.2.10}$$

where $\{f, g\} = \nabla_N f \cdot \nabla_x g - \nabla_x f \cdot \nabla_N g$ is the canonical Poisson bracket associated to the Hamiltonian system

$$\frac{dx_{\alpha}}{d\tau} = \frac{\partial H_{\alpha}}{\partial N}, \quad \frac{dN_{\alpha}}{d\tau} = -\frac{\partial H_{\alpha}}{\partial x}, \tag{I.2.11}$$

$\gamma_\alpha = \mathrm{tr}(\varepsilon_1 \pi_\alpha)$ is the absorption coefficient, and

$$\mathcal{S}_{\alpha\beta}(w)(dx, dN) = \int_{\mathbb{R}^d} \big[\sigma_{\beta\alpha}(x, N', dN) w_\beta(dx, dN') - \sigma_{\alpha\beta}(x, N, dN') w_\alpha(dx, dN)\big],$$

is referred to as the scattering operator. The cross section $\sigma_{\alpha\beta}(x, N, dN')$ is an (x, N)-dependent measure on $\mathbb{R}^d$ related to the probability of transition from the state (x, N, α) to the state (x, N', β), so that it accounts for the stochasticity of both the refractive index (momentum) and the wave mode (cf., Chapter I.1). From the derivation [101, 102], one can observe that $\sigma_{\alpha\beta}$ satisfies automatically the important

Assumption I.2. *For every point (x, N) fixed, the measure $\sigma_{\alpha\beta}(x, N, dN')$ is supported on $\mathcal{C}_\beta \cap \{x\}$ in the sense that*

$$\int_{\mathbb{R}^d} f(N') \sigma_{\alpha\beta}(x, N, dN') = 0,$$

for any function $f \in C_0(\mathbb{R}^d)$ that vanishes when $H_\beta(x, N') = 0$.

Physically assumption I.2 means that the new state (x, N', β) must satisfy the dispersion relation of the new mode β. The scattering operator, in agreement with the heuristic discussion in Chapter I.1, is responsible of two different types of physics phenomena. On one side, due to scattering of the refractive index vector N, a broadening of the beam in momentum space can be produced. This is then translated into a spatial broadening of the beam cross-section via the transport term $\{H_\alpha, w_\alpha\}$, a mechanism which is referred to as hypocoercivity [98]. On the other, due to the coupling of different polarization modes, energy may be exchanged between different modes, determining what is referred to as cross-polarization scattering. The measures w_α provide the average energy density carried by the wave field, which is - according to the informal discussion of Chapter I.1 - a quantity of particular interest for the envisaged fusion applications. The idea is to write a suitable boundary-value

problem for equation (I.2.10), which is mathematically well posed and at the same time describes correctly the envisaged physics applications.

I.2.3 Boundary value problem for the wke

Consider the hypersurface in the physical space, (cf. section 0.2.4)

$$\Sigma = \{x = (y, z) \in \mathbb{R}^{d-1} \times \mathbb{R} \mid z = 0\}, \tag{I.2.12}$$

together with the domain $\Omega \subset \mathbb{R}^d$ defined as

$$\Omega = \{x = (y, z) \in \mathbb{R}^{d-1} \times \mathbb{R} \mid z > 0\}, \tag{I.2.13}$$

so that $\Sigma = \partial\Omega$. Let n_Ω be the outward normal to Ω, so that $n_\Omega = (0, \ldots, 0, -1)$. In what follows, the phase-space extension of Σ

$$\Sigma_+ := \{(y, z, N_y, N_z) \in \mathbb{R}^{d-1} \times \mathbb{R} \times \mathbb{R}^{d-1} \times \mathbb{R} \mid z = 0,\ N_z > 0\} \tag{I.2.14}$$

is considered. If H_α is an eigenvalue of the dispersion tensor as defined in Section I.2.1, then the group velocity of the corresponding wave mode α is given by $\nabla_N H_\alpha$. It is assumed in the rest of this work that

$$\nabla_N H_\alpha|_{\Sigma_+} \cdot n_\Omega < 0, \quad \alpha \in M, \tag{I.2.15}$$

which implies in particular that $\partial_{N_z} H_\alpha|_{\Sigma^+} > 0$. Physically it means that on Σ_+ all wave modes propagate towards the interior of Ω.

In order to define a boundary value problem for (I.2.10), the following definitions are needed:

Definition I.1. *Let $\mu(dy, dz)$ be a measure on $Y \times Z$. Then:*

(i) μ is continuous in z if there exists $\mu_z(dy)$ such that $z \mapsto \mu_z(g)$ is contin-

uous $\forall g \in C_0(Y)$*, and*

$$\mu(f) = \int_{Y\times Z} \mu_z(f(\cdot, z))dz$$

for every $f \in C_0(X \times Y)$*.*

(ii) If μ *is continuous in* z*, then the restriction of* μ *on* $\Sigma = \{(y, 0) \mid y \in Y\}$ *is defined as*

$$\mu|_\Sigma(g) = \mu_0(g)$$

for all $g \in C_0(Y)$*.*

With these definitions, one can seek for measures $w = (w_\alpha)$ on $\mathbb{R}^d \times \mathbb{R}^d \times M$, such that

- each w_α is continuous in z in Σ_+, so that the restriction $w|_{\Sigma_+}$ is well defined;
- $w = \{w_\alpha\}$ satisfies *in the sense of distributions* the constrained radiative transport problem [101, 102]

$$\begin{cases} \{H_\alpha, w_\alpha\} = -2\gamma_\alpha w_\alpha + \sum_\beta \mathcal{S}_{\alpha\beta}(w), & \text{(I.2.16a)} \\ H_\alpha w_\alpha = 0, & \text{(I.2.16b)} \\ w_\alpha|_{\Sigma_+} = w^0_\alpha. & \text{(I.2.16c)} \end{cases}$$

Equation (I.2.16c) provides the boundary conditions on the phase-space subset Σ_+ for each w_α, and boundary data of the form

$$w^0_\alpha(y, dN) = f_\alpha(y, N_y)dN_y \times \delta_{n_\alpha(y,N_y)}(dN_z) \tag{I.2.17}$$

are considered, where $N = (N_y, N_z)$ with $N_y \in \mathbb{R}^{d-1}$ its component tangent to Σ and N_z normal to it. The positive function $f_\alpha \in C^\infty(\mathbb{R}^{d-1} \times \mathbb{R}^{d-1})$ describes the beam cross-section in phase space and thus is rapidly decreasing at infinity. The datum is singular only in the component N_z of the refractive

index orthogonal to the plane Σ, with a Dirac measure centered on $N_z = n_\alpha(y, N_y)$ obtained by solving the local dispersion relation

$$H_\alpha(y, 0, N) = 0, \quad N = (N_y, N_z),$$

for N_z. It follows, in particular, that $w_\alpha|_{\Sigma_+}$ for $y \in \Sigma$ is supported on the dispersion manifold $\mathcal{C}_\alpha$. Notice that the condition (I.2.16c) is imposed on Σ_+, so that positive values of N_z are selected. Physically this means that the boundary datum w^0_α only provides the incident field: energy on Σ coming from a reflection would have negative N_z, and therefore does not belong to Σ_+. Therefore, the formulation of (I.2.16c) is in agreement with the general discussion of Section 0.2.2.

When the Hamiltonian H_α is such that the dispersion equation can be solved analytically for one of the components of N globally over the relevant spatial domain, the singular part of the solution w_α can be factored out and the kinetic equation (I.2.16) is therefore greatly simplified. For particularly simple models of medium and without scattering one can even find analytic solutions [48]. For realistic situations however a global analytically solution of the dispersion equation is not available. Rather then patching together local solutions, the general problem (I.2.16) is addressed directly.

I.2.4 Computation of physical quantities

It is important to point out how the statistically averaged Wigner measure can be used to reconstruct physical quantities which are of great interest for the envisaged applications. In general, if $\mathcal{U} \subseteq \mathbb{R}^d$ is a domain, the average value of a certain observable f over a phase-space subset $\{(x, N) \mid x \in \mathcal{U},\ N \in \mathcal{V}\}$ will be given as the integral of f over $\mathcal{U} \times \mathcal{V}$, weighted by the Wigner measure. For a more detailed discussion on may refer to [101] or [43], while here some examples are provided:

- The energy carried by the mode α in a region $\mathcal{U} \subseteq \mathbb{R}^d$ is given by

$$\mathcal{E}_\alpha(\mathcal{U}) = \left(\frac{\kappa}{2\pi}\right)^d \int_{\mathcal{U}\times\mathbb{R}^d} \frac{w_\alpha}{4\pi}\, dx\, dN. \tag{I.2.18}$$

- The power deposited in $\mathcal{U}$ by the wave mode α can be computed as

$$\mathcal{P}_\alpha(\mathcal{U}) = \left(\frac{\kappa}{2\pi}\right)^d \int_{\mathcal{U}\times\mathbb{R}^d} \frac{c w_\alpha}{4\pi}\gamma_\alpha\, dx\, dN. \tag{I.2.19}$$

A correct quantification of (I.2.19) in realistic scenarios is among the main goals of the `WKBeam` code [101, 102] (cf., Section I.4.2), which computes a numerical solution of the wave kinetic equation (I.2.16) by means of the method presented in the next chapters.

I.3 A numerical scheme for the wave kinetic equation for wave beams

The boundary-value problem (I.2.16) with singular data and constraints is not easily addressed directly. In such situations it is usually more convenient to introduce an artificial time-variable and consider an auxiliary Cauchy problem [43]. Specifically, a collection of time dependent measures $u = \{u_\alpha\}$ is considered, that solve the unconstrained Cauchy problem

$$\begin{cases} \partial_t u_\alpha + \{H_\alpha, u_\alpha\} = -2\gamma_\alpha u_\alpha + \sum\nolimits_\beta \mathcal{S}_{\alpha\beta}(u), \\ u_\alpha|_{t=0} = u^0_\alpha, \end{cases} \tag{I.3.1}$$

where the initial condition is obtained from the boundary datum (I.2.17) by concentrating it on the initial plane Σ, namely,

$$u^0_\alpha(dx, dN) = C_\alpha(y, N)dy \times \delta(dz) \times w^0_\alpha(y, dN), \tag{I.3.2}$$

with $x = (y, z)$, $y \in \mathbb{R}^{d-1}$ and $z \in \mathbb{R}$, being Cartesian coordinates such that $\Sigma = \{z = 0\}$ and $\delta(dz)$ the Dirac's measure on $\mathbb{R}$ concentrated at $z = 0$. The choice of the function $C_\alpha(y, N)$ is discussed in Section I.3.3.4. Throughout this work the following assumption on the Hamiltonians and the coefficients of the scattering operator are made:

Assumption I.3. *For each $\alpha \in M$,*

1. *The Hamiltonian field of H_α is complete on the considered domain.*
2. *The function $\sum_{\beta\in M}\int_{\mathbb{R}^d}\sigma_{\alpha\beta}(x,N,dN')$ is bounded.*
3. *$\sigma_{\alpha\beta}(x,N,dN')/\sum_{\beta\in M}\int_{\mathbb{R}^d}\sigma_{\alpha\beta}(x,N,dN')$ is a probability measure.*

I.3.1 Definition of the stochastic process

The aim of this work is to derive a rigorous numerical scheme for the solution of (I.3.1) and then apply it to the solution of (I.2.16). The natural framework for this purpose appears to be that of Monte-Carlo methods for transport equation based on jump Markov processes [43, 85].

The continuous-time stochastic process

$$\{(X(t),\mathcal{N}(t),a(t));t\geq 0\}\subseteq\mathbb{R}^d\times\mathbb{R}^d\times M$$

is considered, namely, a one-parameter family of random variables

$$(X(t),\mathcal{N}(t),a(t))\in\mathbb{R}^d\times\mathbb{R}^d\times M,$$

where $(X(t),\mathcal{N}(t))$ takes values in the geometrical optics phase space $\mathbb{R}^d\times\mathbb{R}^d$, and $a(t)$ models the polarization mode, varying on a finite set M, cf. assumption I.1. In particular, it will be a jump process defined in terms of

- a bounded and positive-definite function $\lambda:\mathbb{R}^d\times\mathbb{R}^d\times M\to\mathbb{R}$;
- a family of probability measures $\{\Pi(x,N,\alpha;dN',\beta)\}$ on the set $\mathbb{R}^d\times M$, parametrized by points $(x,N,\alpha)\in\mathbb{R}^d\times\mathbb{R}^d\times M$;
- a collection of *complete* vector fields over $\mathbb{R}^d\times\mathbb{R}^d$ parametrized by M, that is, a map $b:\mathbb{R}^d\times\mathbb{R}^d\times M\to\mathbb{R}^d\times\mathbb{R}^d$ such that $b(\cdot,\alpha)$ is a complete C^1 vector field.

For any sequence of points $\{T_j\geq 0;j=1,2,\ldots\}$, the following notation is

introduced,

$$x_j^{\pm} = \lim_{t \to T_j^{\pm}} X(t), \quad N_j^{\pm} = \lim_{t \to T_j^{\pm}} \mathcal{N}(t), \quad \alpha_j^{\pm} = \lim_{t \to T_j^{\pm}} a(t), \tag{I.3.3}$$

when the limits exist.

The jump process is defined by the following conditions [43]:

1. There is a sequence of "time of jumps" $0 < T_1 < \ldots < T_j < \ldots$ extracted from a Poisson distribution of parameter $\bar{\lambda} = \sup \lambda$.

2. For any $t \in [T_j, T_{j+1})$, $a(t) = \alpha_j^+ \in M$ is constant, while $(X(t), \mathcal{N}(t))$ is the solution of the ordinary differential equation

$$\begin{aligned} &\frac{d}{dt}(X(t), \mathcal{N}(t)) = b(X(t), \mathcal{N}(t), \alpha_j^+), \\ &(X(T_j), \mathcal{N}(T_j)) = (x_j^+, N_j^+). \end{aligned} \tag{I.3.4}$$

   The solution of (I.3.4) exists for all t since by hypothesis $b(\cdot, \alpha_j^+)$ is complete, and $X, \mathcal{N} \in C^1([T_j, T_{j+1}))$.

3. At time T_j, $j \geq 1$, a "jump" occurs with probability

$$P_j = \lambda(x_j^-, N_j^-, \alpha_j^-)/\bar{\lambda} \leq 1.$$

4. If a "jump" occurs, then

   a) $x_j^+ = x_j^-$;

   b) $\alpha_j^+ = \beta$ with β extracted from the discrete probability distribution

$$p_j(\beta) = \int_{\mathbb{R}^d} \Pi(x_j^-, N_j^-, \alpha_j^-; dN', \beta);$$

   c) N_j^+ is extracted from the probability measure

$$\rho_j(dN') = \Pi(x_j^-, N_j^-, \alpha_j^-; dN', \alpha_j^+).$$

Otherwise the process is continuous at T_j.

Remark I.3.1.1. *The notation $C_b^k(\mathbb{R}^d \times \mathbb{R}^d \times M)$ for $k \geq 0$ will refer to the space $[C_b^k(\mathbb{R}^d \times \mathbb{R}^d)]^m$ where m is the cardinality of the finite set of modes M and C_b^k is the space of C^k-functions bounded with all derivatives up to the order k. Analogously one can define $C_0^k(\mathbb{R}^d \times \mathbb{R}^d \times M)$, where C_0^k is the space of C^k-functions of compact support. Hence for $f \in C_b^k(\mathbb{R}^d \times \mathbb{R}^d \times M)$ one can write $f(x, N, \alpha) = f_\alpha(x, N)$ depending on the context. Analogously, a time dependent measure u_t over $\mathbb{R}^d \times \mathbb{R}^d \times M$ is identified with the collection of measures $\{u_\alpha(t); \alpha \in M, t \geq 0\}$.*

I.3.2 Statement of the results

In order to establish a link between the stochastic process and equation I.3.8, the concepts of infinitesimal generator and probability law of the stochastic process need to be introduced. The definitions are here recalled, following Lapeyre et al. [43].

Definition I.2. *The* infinitesimal generator *of the process is defined as the operator*

$$\begin{aligned} \mathcal{A} : C_b^1(\mathbb{R}^d \times \mathbb{R}^d \times M) &\longrightarrow C_b^0(\mathbb{R}^d \times \mathbb{R}^d \times M), \\ f &\longmapsto \mathcal{A}f, \end{aligned}$$

given by [43]

$$(\mathcal{A}f)(x, N, \alpha) = \lim_{h \to 0^+} \frac{1}{h} \Big[\mathbb{E}_{x,N,\alpha} \big[f\big(X(h), \mathcal{N}(h), a(h)\big) \big] - f(x, N, \alpha) \Big], \quad \text{(I.3.5)}$$

where $\mathbb{E}_z[Z(t)]$ is the conditional expectation of the random variable $Z(t)$ given that $Z(0) = z$.

Definition I.3. *The* probability law *of the process is defined as*

$$\begin{aligned}\mu_t : \mathcal{B}_d \times \mathcal{B}_d \times M &\longrightarrow [0,1],\\ (B_x, B_N, \alpha) &\longmapsto \mathbb{P}(X(t) \in B_x, \mathcal{N}(t) \in B_N, a(t) = \alpha),\end{aligned}$$

where $\mathcal{B}_d$ is the σ-algebra of Borel sets in $\mathbb{R}^d$ and $\mathbb{P}$ indicates the joint probability.

In virtue of Riesz-Markov-Kakutani representation Theorem [74, Theorem 2.14] the measure μ_t can be identified with a continuous linear functional on $C_0(\mathbb{R}^d \times \mathbb{R}^d \times M)$, whose action on a test-function f is given by

$$\mu_t(f) = \sum_{\alpha \in M} \int_{\mathbb{R}^d \times \mathbb{R}^d} f(x, N, \alpha) \mu_t(dx, dN, \alpha), \tag{I.3.6}$$

This can also be expressed in term of the stochastic process in the form

$$\mu_t(f) = \sum_{\alpha \in M} \int_{\mathbb{R}^d \times \mathbb{R}^d} \mathbb{E}_{x,N,\alpha}[f(X(t), \mathcal{N}(t), a(t))] \mu_0(dx, dN, \alpha), \tag{I.3.7}$$

where μ_0 is the probability law of $(X(0), \mathcal{N}(0), a(0))$. The following result relates the infinitesimal generator to the probability law of a process at a given time.

Proposition I.3.1 (proposition 2.3.2 of Lapeyre et al. [43])**.** *The probability law $\{\mu_t, t \geq 0\}$ of a continuous-time Markov process satisfies*

$$\mu_t(f) = \mu_0(f) + \int_0^t \mu_s(\mathcal{A}f) ds, \quad \forall f \in C_b^1(\mathbb{R}^d \times \mathbb{R}^d \times M), \tag{I.3.8}$$

where μ_0 is the probability law of $(X(0), \mathcal{N}(0), a(0))$.

Moreover, if the measures μ_t are absolutely continuous with respect to the Lebesgue measure, that is, there exists a function $p(t, \cdot) \in L^1$ such that

$\mu_t(dx, dN, \alpha) = p(t, x, N, \alpha)dx\, dN$, and p is sufficiently regular, then

$$\begin{cases} \dfrac{\partial p}{\partial t} = \mathcal{A}^* p, \quad t > 0, \\ p|_{t=0} = p_0 \end{cases} \tag{I.3.9}$$

for suitable initial condition, where $\mathcal{A}^*$ is the formal adjoint of $\mathcal{A}$.

The idea is to use these results to build a solution of (I.3.1), by exploiting the fact that equation (I.3.8) amounts to a weak formulation of problem (I.3.1) with $\gamma_\alpha = 0$, with the elements that characterize the process (λ, Π, b) being opportunely defined in terms of $\sigma_{\alpha\beta}$ and H_α:

- The advecting field is taken as

$$b(x, N, \alpha) = \left(\nabla_N H_\alpha(x, N), -\nabla_x H_\alpha(x, N)\right). \tag{I.3.10}$$

- As total cross-section, one can take

$$\lambda(x, N, \alpha) = \sum_\beta \int_{\mathbb{R}^d} \sigma_{\alpha\beta}(x, N, dN'). \tag{I.3.11}$$

- The family of probability measures is taken as

$$\Pi(x, N, \alpha; dN', \beta) = \frac{\sigma_{\alpha\beta}(x, N, dN')}{\lambda(x, N, \alpha)}. \tag{I.3.12}$$

In view of assumption I.3, b, λ and Π satisfy the requirements of Section I.3.1.

For the infinitesimal generator the following result will be proven in Section I.3.3.1:

Theorem I.1. *The infinitesimal generator of the described process acts on* $f \in C_b^1(\mathbb{R}^d \times \mathbb{R}^d \times M)$ *as* $\mathcal{A}f = b \cdot \nabla f + \lambda\left[\mathcal{J}f - f\right]$, *where*

$$\mathcal{J}f(x, N, \alpha) = \sum_{\beta \in M} \int_{\mathbb{R}^d} f(x, N', \beta)\Pi(x, N, \alpha; dN', \beta).$$

With b, λ, and Π defined in equations (I.3.10)-(I.3.12), the formal adjoint of the infinitesimal generator computed in Theorem I.1 amounts to

$$\mathcal{A}^* f_\alpha = -\{H_\alpha, f_\alpha\} + \sum_{\beta \in M} \mathcal{S}_{\alpha\beta}(f), \quad f = \{f_\alpha\}, \tag{I.3.13}$$

which is the same operator entering the wave-kinetic equation (I.3.1). Therefore, equations (I.3.8) and (I.3.9) correspond to the weak and the strong formulation of problem (I.3.1) with $\gamma_\alpha = 0$. In order to account for weak dissipation (i.e., $\gamma_\alpha \neq 0$), one can define from μ_t a new measure $\tilde{\mu}_t$. If $f \in C_b(\mathbb{R}^d \times \mathbb{R}^d \times M)$ and

$$F_\gamma(X(t), \mathcal{N}(t), a(t)) := \mathrm{e}^{-2\int_0^t \gamma(X(s),\mathcal{N}(s),a(s))ds} f(X(t), \mathcal{N}(t), a(t)), \tag{I.3.14}$$

the action of $\tilde{\mu}_t$ on f is given by

$$\begin{aligned} \tilde{\mu}_t(f) &= \mathbb{E}_{0,\mu_0}\left[F_\gamma(X(t), \mathcal{N}(t), a(t))\right] \\ &:= \sum_{\alpha \in M} \int_{\mathbb{R}^d \times \mathbb{R}^d} \mathbb{E}_{x,N,\alpha}\left[F_\gamma(X(t), \mathcal{N}(t), a(t))\right] \mu_0(dx, dN), \end{aligned} \tag{I.3.15}$$

The following will be proven in Section I.3.3.2

Proposition I.3.2. *Let $\tilde{\mu}_t$ be as defined in (I.3.15)-(I.3.14). Then, for every $f \in C_b^1(\mathbb{R}^d \times \mathbb{R}^d \times M)$ and for every $t > 0$,*

$$\tilde{\mu}_t(f) = \tilde{\mu}_0(f) + \int_0^t \tilde{\mu}_s(\mathcal{A}f - 2\gamma f)ds. \tag{I.3.16}$$

Notice that if $\tilde{\mu}_t$ is absolutely continuous with respect to the Lebesgue measure, with a C^1 Radon-Nikodym derivative $\tilde{p}(t, x, N)$, then

$$\begin{cases} \dfrac{\partial \tilde{p}}{\partial t} = \mathcal{A}^* \tilde{p} - 2\gamma \tilde{p}, \quad t > 0, \\ \tilde{p}|_{t=0} = \tilde{p}_0, \end{cases} \tag{I.3.17}$$

where the right-hand side corresponds to the operator entering the wave kinetic

equation.

From the last presented result one can construct a weak solution of problem (I.3.1) from the measure $\tilde{\mu}_t$ obtained from the probability law of the process μ_t, exploiting the linearity of the infinitesimal generator $\mathcal{A}$.

Corollary 1. *Let $\tilde{\mu}_t$ be as defined in (I.3.15), where μ_t is the law of the process with advecting field b, total cross-section λ, and Π defined by equations (I.3.10)-(I.3.12). Then for every non-negative measure u_0 such that $C := u_0(\mathbb{R}^d \times \mathbb{R}^d \times M) < \infty$, the rescaled measure*

$$u_t = C\tilde{\mu}_t,$$

is non-negative and it satisfies

$$u_t(f) = u_0(f) + \int_0^t u_s(\mathcal{A}f - 2\gamma f)ds, \tag{I.3.18}$$

which means that u_t is a weak solution of (I.3.1) with initial condition u_0.

At last, the weak solution u_t of (I.3.1) is used to construct a solution of the wave kinetic equation (I.2.16). First the dispersion relation is addressed. Under assumption I.2, the stochastic process preserves the characteristic variety of the operator, i.e., the dispersion relation of the individual modes. More specifically, as it will be proven in Section I.3.3.3,

Theorem I.2. *If the cross-section $\sigma_{\alpha\beta}$ satisfies assumption I.2, any sample trajectory $\{(X(t), \mathcal{N}(t), a(t)); t \geq 0\}$ with*

$$(X(0), \mathcal{N}(0), a(0)) \in \mathcal{C} = \bigcup_\alpha \mathcal{C}_\alpha,$$

satisfies $H(X(t), \mathcal{N}(t), a(t)) = 0$ for every $t > 0$ almost surely.

Thanks to all the previous results, one can finally find a solution of (I.2.16). If Σ, Ω and Σ_+ are as defined in (I.2.12)-(I.2.14), then:

Definition I.4 (Solution of (I.2.16))**.** *A measure $w = w(dx, dN, \alpha)$ on $\mathbb{R}^d \times \mathbb{R}^d \times M$ is a weak solution of (I.2.16) if:*

(a) w satisfies (I.2.16a) in the sense of distributions in $\Omega \times \mathbb{R}^d \times M$. Specifically,

$$w(\mathcal{A}f - 2\gamma f) = 0, \quad \forall f \in C_0^1(\Omega \times \mathbb{R}^d \times M).$$

(b) The dispersion relation (I.2.16b) is satisfied in the weak form

$$w(Hf) = 0 \quad \forall f \in C_0(\mathbb{R}^d \times \mathbb{R}^d \times M).$$

(c) w is continuous z in a neighborhood of Σ_+ in $\bar{\Omega} \times \mathbb{R}^{d-1} \times \mathbb{R}_+$, and the boundary condition (I.2.16c) is satisfied in the sense that

$$w_\alpha|_{\Sigma_+}(g) = w_\alpha^0(g), \quad \alpha \in M, \;\; g \in C_0(\Sigma_+).$$

The main result of this section can now be stated. This allows one to construct a weak solution of the boundary value problem (I.2.16) for the wave kinetic equation, and a proof is provided in Section I.3.3.4:

Theorem I.3. *Let the coefficients H_α, $\sigma_{\alpha\beta}$ and γ_α of the wave kinetic equation (I.2.16a) be such that*

1. *H_α and $\sigma_{\alpha\beta}$ satisfy assumptions I.2 and I.3.*
2. *There exists $z^* > 0$ such that, being*

$$U = \{(y, z, N_y, N_z) \in \mathbb{R}^{d-1} \times \mathbb{R} \times \mathbb{R}^{d-1} \times \mathbb{R} \mid z < z^*, \; N_z > 0\},$$

$\sigma_{\alpha\beta} = 0$, $\nabla_x H_\alpha = 0$ and $\partial_{N_z} H_\alpha > 0$ in U for all $\alpha, \beta \in M$.

3. *The absorption coefficients are bounded from below, i.e., $\gamma_\alpha \geq \Gamma > 0$, $\alpha \in M$.*

Let u_t be the solution constructed in Corollary 1 with initial condition u_0 given in the form (I.3.2). Then,

(i) For every $f \in C_b(\mathbb{R}^d \times \mathbb{R}^d \times M)$, the function $t \mapsto u_t(f)$ is in $L^1(\mathbb{R}_+)$, and the map

$$f \longmapsto w(f) = \int_0^{+\infty} u_t(f)dt$$

defines a non-negative measure $w(dx, dN, \alpha)$ on $\mathbb{R}^d \times \mathbb{R}^d \times M$.

(ii) The measure $w(dx, dN, \alpha)$ is a solution of the radiative transport model (I.2.16) in the sense of Definition I.4.

Remark I.3.2.1 (Physics interpretation)**.** *The assumptions in Theorem I.3 are compatible with the typical experimental setup of the physics applications envisaged by this work: $\sigma_{\alpha\beta} = 0$ and $\nabla_x H_\alpha = 0$ in U translate into the fact that the antenna / wave-guide system Σ is located in free-space, which is the case for electron-cyclotron waves. In particular, by definition of U, the whole half-space $\{z \leq 0\}$ is fully located in free-space, which excludes closed orbits and eigenmodes. The assumption on the hamiltonian flow $\partial_{N_z} H_\alpha > 0$ implies that there is a non-zero energy flow in the direction orthogonal to Σ, and selects a direction of propagation for the wave, which is therefore injected into Ω. The assumption on the coefficients γ_α is common for this type of problems, and it ensures some coercivity property of the wave operator on the side of Maxwell's equations [81]. In the practical numerical applications γ_α is not strictly positive, being usually set to zero in a large portion of the domain. The beam parameters though are such that it points at a resonant surface, where its energy is completely absorbed, so that the first statement in Theorem I.3 is still valid. Therefore, the necessary restrictions for the derivation on the mathematics side do not affect the possibility to apply this result to realistic plasma physics scenarios.*

I.3.3 Proof of the results

Proofs of the results stated in Section I.3.2 are reported here in details.

I.3.3.1 Computation of the infinitesimal generator

Theorem I.1 will be addressed first, by directly computing the infinitesimal generator as defined in (I.3.5). The notion of *transition semigroup* of a jump Markov process will be used, defined as follows:

Definition I.5. *Given a jump Markov process* $\{V(t); t \geq 0\}$*, its transition semigroup* Q_t *is defined as the conditional probability*

$$Q_t(v; B) = \mathbb{P}_v \left(V(t) \in B \right),$$

where B *is a measurable set and* $\mathbb{P}_v$ *is the probability of* B *conditioned to the initial condition* $V(0) = v$*. The transition semigroup defines an operator, also denoted as* Q_t*, that acts on a measurable function* f *as*

$$(Q_t f)(v) := \mathbb{E}_v \left[f(V(t) \right] = \int f(v') Q_t(v; dv').$$

The family of operators $\{Q_t, t \geq 0\}$ *has the semigroup property, which means*

$$(Q_{t+s} f)(v) = (Q_t(Q_s f))(v), \tag{I.3.19}$$

In order to proceed with the proof one needs to further characterize the process, in particular for what concerns its momentum component $\mathcal{N}(t)$. The idea is to decompose $\mathcal{N}$ as the sum of a pure jump process and a continuous one. In order to achieve this, one can define a process $\{\tilde{\mathcal{N}}(t); t \geq 0\}$ as

- $\tilde{\mathcal{N}}(0) = \mathcal{N}(0)$;
- For $t \in [T_j, T_{j+1})$, where $(T_j)_{j \geq 1}$ are the times of the jumps,

$$\tilde{\mathcal{N}}(t) = \tilde{\mathcal{N}}(0) + \sum_{\kappa=1}^{j} (N_k^+ - N_k^-),$$

where N_j^- and N_j^+ denote the value of the process $\mathcal{N}$ at $t = T_j$ before and after the jump, respectively (cf., (I.3.3)), where the jumps are given as in the previous section.

The process $\tilde{\mathcal{N}}(t)$ is therefore a pure jump process, and it is built in such a way that the process

$$\mathtt{N}(t) = \mathcal{N}(t) - \tilde{\mathcal{N}}(t)$$

is $C^0(\mathbb{R}_+)$ and $\mathtt{N}(0) = 0$.

All the ingredients necessary to prove Theorem I.1 have now been defined, and the proof will be preceded by some intermediate steps. Consider, for every $x \in \mathbb{R}^d$ the pure jump process in $\mathbb{R}^d \times M$,

$$(\tilde{\mathcal{N}}(t), a(t)) := \pi\left((X(t), \tilde{\mathcal{N}}(t), a(t))\right),$$

where $x = X(0)$ and the projection π is defined as

$$\begin{aligned} \pi : \mathbb{R}^d \times \mathbb{R}^d \times M &\longrightarrow \mathbb{R}^d \times M \\ (x, N, \alpha) &\longmapsto (N, \alpha). \end{aligned}$$

The following holds:

Lemma I.3.1. *Consider, for every $x \in \mathbb{R}^d$, the process $\left\{\tilde{\mathcal{N}}(t), a(t)\right\}$ defined above. Then,*

(i) The transition semigroup of the process is given by

$$\begin{aligned} Q_t(x, N, \alpha; A, \alpha') = \mathrm{e}^{-\bar{\lambda}t}\Big(&\delta_N(A)\delta_{\alpha,\alpha'} \\ &+ \lambda(x_1^-, N_1^-, \alpha_1^-)\Pi(x_1^-, N_1^-, \alpha_1^-; A, \alpha')t \\ &+ (\bar{\lambda}t)^2\tilde{Q}_t(x, N, \alpha; A, \alpha')\Big), \end{aligned} \tag{I.3.20}$$

where $A \subseteq \mathbb{R}^d$ is a measurable set, $(x_1^-, N_1^-, \alpha_1^-)$ is defined in (I.3.3) and $\tilde{Q}_0$ is bounded.

(ii) The infinitesimal generator of the process acts on a function $f \in C_b^1(\mathbb{R}^d \times \mathbb{R}^d \times M)$ as $\tilde{\mathcal{A}}f = \lambda\left[\mathcal{J}f - f\right]$, where $\lambda = \lambda(x, N, \alpha)$ and

$$\mathcal{J}f(x, N, \alpha) = \sum_\beta \int_{\mathbb{R}^d} f(x, N', \beta)\Pi(x, N, \alpha; dN', \beta) \tag{I.3.21}$$

Proof. The two points are proven separately:

(i) Let $\{T_n\}_{n\in\mathbb{N}_0}$ be the times of jump of the whole process $\{(X(t),\mathcal{N}(t),a(t))\}$, with $T_0 = 0$. Recalling the definition of Q_t, for a measurable set $A \subseteq \mathbb{R}^d \times M$, and for every $t > 0$, one has:

$$\begin{aligned} Q_t(x,N,\alpha;A,\alpha') &= \mathbb{P}_{x,N,\alpha}(\tilde{\mathcal{N}}(t) \in A, a(t) = \alpha') \\ &= \sum_{n\geq 0} \mathbb{P}(T_n < t, T_{n+1} \geq t) \\ &\qquad \times \mathbb{P}_{x,N,\alpha}(\tilde{\mathcal{N}}(t) \in A, a(t) = \alpha' \mid T_n < t, T_{n+1} \geq t) \\ &= \mathrm{e}^{-\bar{\lambda}t} \sum_{n\geq 0} \frac{(\bar{\lambda}t)^n}{n!} \mathbb{P}_{x,N,\alpha}(\tilde{\mathcal{N}}_n^+ \in A, \alpha_n^+ = \alpha'), \end{aligned}$$

where the second step follows from the definition of the sequence (T_n) in section I.3.4. One can compute the first two terms of the series, namely:

$(n = 0)$ - No jumps occur, so that the corresponding term in the above series reads

$$\mathbb{P}_{x,N,\alpha}(N \in A, \alpha = \alpha') = \delta_N(A)\delta_{\alpha,\alpha'}.$$

$(n = 1)$ - Recalling the definitions in (I.3.3) and the definition of $\tilde{\mathcal{N}}$, one has

$$\begin{aligned} &\bar{\lambda}\mathbb{P}_{x,N,\alpha}(\tilde{\mathcal{N}}_1^+ \in A, \alpha_1^+ = \alpha')t \\ &\qquad = \bar{\lambda}\frac{\lambda(x_1^-,N_1^-,\alpha_1^-)}{\bar{\lambda}} \mathbb{P}_{x,N,\alpha}(N_1^+ \in A, \alpha_1^+ = \alpha')t \\ &\qquad\qquad = \lambda(x_1^-,N_1^-,\alpha_1^-)\Pi(x_1^-,N_1^-,\alpha_1^-;A,\alpha')t, \end{aligned}$$

where Π is the probability measure that defines the whole process $\{(X(t),\mathcal{N}(t),a(t))\}$. Notice that by the definition given in (I.3.3), the dependency on t and x of the expression obtained above is hidden in the points x_1^-, N_1^-, α_1^-.

$(n \geq 2)$ - The remaining terms of the series provide

$$\sum_{n\geq 2} \frac{(\bar{\lambda}t)^n}{n!} \mathbb{P}_{x,N,\alpha}(\tilde{\mathcal{N}}_n^+ \in A, \alpha_n^+ = \alpha')$$
$$= (\bar{\lambda}t)^2 \sum_{n\geq 0} \frac{(\bar{\lambda}t)^n}{(n+2)!} \mathbb{P}_{x,N,\alpha}(\tilde{\mathcal{N}}_{n+2}^+ \in A, \alpha_{n+2}^+ = \alpha')$$
$$:= \frac{(\bar{\lambda}t)^2}{2} \tilde{Q}_t(x, N, \alpha; A, \alpha'),$$

and one can observe that by definition Q_0 is finite.

(ii) By definition of infinitesimal generator, one has to compute the limit

$$\lim_{h\to 0^+} \frac{1}{h} \left[\mathbb{E}_{N,\alpha} f\left(\tilde{\mathcal{N}}(h), a(h)\right) - f(N,\alpha) \right],$$

where $\mathbb{E}_{x,N,\alpha}$ denotes the conditional expectation with respect to $X(0) = x$, $\tilde{\mathcal{N}}(0) = N$ and $a(0) = \alpha$. Being Q_t the transition semigroup as computed in point (i),

$$\frac{1}{h} \left[\mathbb{E}_{x,N,\alpha} f\left(x, \tilde{\mathcal{N}}(h), a(h)\right) - f(x,N,\alpha) \right]$$
$$= \frac{1}{h} \sum_\beta \int_{\mathbb{R}^d} Q_t(x, N, \alpha, dN', \beta)[f(x, N', \beta) - f(x, N, \alpha)]$$
$$= \Bigg(\frac{1}{h} \sum_\beta \int_{\mathbb{R}^d} [f(x, N', \beta) - f(x, N, \alpha)] \delta_N(dN') \delta_{\alpha,\beta}$$
$$+ \lambda(x_1^-, N_1^-, \alpha_1^-) \sum_\beta \int_{\mathbb{R}^d} [f(x, N', \beta) - f(x, N, \alpha)] \Pi(x_1^-, N_1^-, \alpha_1^-; dN', \beta)$$
$$+ \frac{1}{h} (\bar{\lambda}h)^2 \sum_\beta \int_{\mathbb{R}^d} [f(x, N', \beta) - f(x, N, \alpha)] \tilde{Q}_h(x, N, \alpha; dN', \beta) \Bigg) \mathrm{e}^{-\bar{\lambda}h}$$

The first term is zero, while the last one goes to zero for $h \to 0^+$. The limit $h \to 0^+$ of the second term gives $\lambda[\mathcal{J}f - f]$, as from the definitions in (I.3.3) one can observe that $(x_1^-, N_1^-, \alpha_1^-) \to (x, N, \alpha)$ for $h \to 0^+$.

□

Given now a function $f \in C_b^1(\mathbb{R}^d \times \mathbb{R}^d \times E)$, one can perform, for small t, a Taylor expansion of f around $\tilde{\mathcal{N}}(t)$,

$$\begin{aligned} f(x, \mathcal{N}(t), a(t)) &= f\left(x, \tilde{\mathcal{N}}(t) + \mathtt{N}(t), a(t)\right) \\ &= f\left(x, \tilde{\mathcal{N}}(t), a(t)\right) + \mathtt{N}(t) \cdot \int_0^1 \nabla_N f(x, \sigma\tilde{\mathcal{N}}(t) + (1-\sigma)\mathtt{N}(t), a(t)) d\sigma. \end{aligned} \tag{I.3.22}$$

thanks to the fact that $\mathtt{N} \in C^0$ and $\mathtt{N}(0) = 0$ for how it was constructed.

Lemma I.3.2. *Let T_1 be the time of the first jump of $\{(X(t), \mathcal{N}(t), a(t)); t \geq 0\}$. Then for every $f \in C_b^1(\mathbb{R}^d \times \mathbb{R}^d \times M)$,*

$$\lim_{h \to 0^+} \frac{1}{h} \mathbb{E}_{x,N,\alpha} \left\{ \left[f\left(x, \mathcal{N}(h), a(h)\right) - f(x, N, \alpha) \right] \mathbf{1}_{\{T_1 \leq h\}} \right\} = \tilde{\mathcal{A}} f(x, N, \alpha).$$

Proof. Thanks to the splitting discussed above, one can write

$$\begin{aligned} &\frac{1}{h} \mathbb{E}_{x,N,\alpha} \left\{ \left[f\left(x, \mathcal{N}(h), a(h)\right) - f(x, N, \alpha) \right] \mathbf{1}_{\{T_1 \leq h\}} \right\} \\ &\qquad = \frac{1}{h} \mathbb{E}_{x,N,\alpha} \left\{ \left[f\left(x, \tilde{\mathcal{N}}(h), a(h)\right) - f(x, N, \alpha) \right] \mathbf{1}_{\{T_1 \leq h\}} \right\} \\ &\qquad + \frac{1}{h} \mathbb{E}_{x,N,\alpha} \left\{ \left[\mathtt{N}(t) \cdot \int_0^1 \nabla_N f(x, \sigma\tilde{\mathcal{N}}(t) + (1-\sigma)\mathtt{N}(t), a(t)) d\sigma \right] \mathbf{1}_{\{T_1 \leq h\}} \right\}. \end{aligned}$$

One can now treat the limits of the two factors separately. For the first term, Lemma I.3.1 can be applied, from which it follows that

$$\lim_{h \to 0^+} \frac{1}{h} \mathbb{E}_{x,N,\alpha} \left\{ \left[f\left(x, \tilde{\mathcal{N}}(h), a(h)\right) - f(x, N, \alpha) \right] \mathbf{1}_{\{T_1 \leq h\}} \right\} = \tilde{\mathcal{A}} f(x, N, \alpha).$$

For what concerns the second one, its absolute is bounded by

$$\begin{aligned}
&\frac{1}{h}\left|\mathbb{E}_{x,N,\alpha}\left\{\left[\mathtt{N}(t)\cdot\int_0^1\nabla_N f(x,\sigma\tilde{\mathcal{N}}(t)+(1-\sigma)\mathtt{N}(t),a(t))d\sigma\right]\mathbf{1}_{\{T_1\le h\}}\right\}\right|\\
\le&\frac{1}{h}|\sup_{x,N,\alpha}|\nabla_N f(x,N,\alpha)|\mathbb{E}_{x,N,\alpha}\left\{|\mathtt{N}(h)|\,\mathbf{1}_{\{T_1\le h\}}\right\}|\\
\le&\frac{1}{h}\sup_{x,N,\alpha}|\nabla_N f(x,N,\alpha)|\mathbb{E}_{x,N,\alpha}\{|\mathtt{N}(h)|^2\}^{1/2}\mathbb{P}_{x,N,\alpha}(T_1\le h)^{1/2}\\
\le&C\mathbb{P}(T_1\le h)^{1/2},
\end{aligned}$$

where $\mathbb{P}_{x,N,\alpha}$ is the conditional probability with respect to initial values x, N and α, C is a constant, and Hölder's inequality was used to bound the L^1-norm in the second line with the product of L^2-norms in the third one. The last term in the former expression goes to zero as $h\to 0^+$, which concludes the proof. □

Proof of Theorem I.1. One needs to compute the limit

$$\lim_{h\to 0^+}\frac{1}{h}\left[\mathbb{E}_{x,N,\alpha}f\left(X(h),\mathcal{N}(h),a(h)\right)-f(x,N,\alpha)\right].$$

By standard properties of the conditional expectation,

$$\begin{aligned}
\frac{1}{h}&[\mathbb{E}_{x,N,\alpha}f\left(X(h),\mathcal{N}(h),a(h)\right)-f(x,N,\alpha)]=\\
&\frac{1}{h}\mathbb{E}_{x,N,\alpha}\left\{\left[f\left(X(h),\mathcal{N}(h),a(h)\right)-f(x,N,\alpha)\right]\mathbf{1}_{\{T_1>h\}}\right\} &\textit{(i)}\\
&+\frac{1}{h}\mathbb{E}_{x,N,\alpha}\left\{\left[f\left(x,\mathcal{N}(h),a(h)\right)-f(x,N,\alpha)\right]\mathbf{1}_{\{T_1\le h\}}\right\} &\textit{(ii)}\\
&+\frac{1}{h}\mathbb{E}_{x,N,\alpha}\left\{\left[f\left(X(h),\mathcal{N}(h),a(h)\right)-f(x,\mathcal{N}(h),a(h))\right]\mathbf{1}_{\{T_1\le h\}}\right\}, &\textit{(iii)}
\end{aligned}$$

where T_1 is the time of the first jump of the process. First of all, observe that for Lemma I.3.2, *(ii)* tends to $\tilde{\mathcal{A}}f=\lambda[\mathcal{J}f-f]$ as $h\to 0^+$. For what concerns *(iii)*, it is bounded in absolute value by

$$\frac{1}{h}\sup_{x,N,\alpha}|\nabla_x f(x,N,\alpha)|\cdot\mathbb{E}_{x,N,\alpha}\left\{|X(h)-x|^2\right\}^{1/2}\cdot\mathbb{P}_{x,N,\alpha}(T_1\le h)^{1/2}.$$

As $X(t)$ is continuous, $|X(h)-x|$ goes to zero for $h\to 0^+$, and therefore the

above expression is bounded by $C \cdot \mathbb{P}_{x,N,\alpha}(T_1 \leq h)^{1/2}$ for some constant C, which goes to zero for $h \to 0^+$. For *(i)*, observe that as there are no jumps in the interval we are looking at, $a(t)$ is constant and equals to α, while $X(t)$ and $\mathcal{N}(t)$ are solution of

$$\left(\dot{X}(t), \dot{\mathcal{N}}(t)\right) = b\left(X(t), \mathcal{N}(t), \alpha\right)$$
$$(X(0), \mathcal{N}(0)) = (x, N).$$

Therefore,

$$\frac{1}{h}\mathbb{E}_{x,N,\alpha}\left\{\left[f\left(X(h), \mathcal{N}(h), a(h)\right) - f(x, N, \alpha)\right] \mathbf{1}_{\{T_1 > h\}}\right\}$$
$$= \frac{1}{h}\int_0^h b(X(s), \mathcal{N}(s), \alpha) \cdot \nabla_{x,N} f\left(X(s), \mathcal{N}(s), \alpha\right) ds \, \mathbb{P}_{x,N,\alpha}(T_1 > h),$$

which converges to $b(x, N, \alpha) \cdot \nabla_{x,N} f(x, N, \alpha)$ as $h \to 0^+$, since $\mathbb{P}_{x,N,\alpha}(T_1 > h) \to 1$. □

I.3.3.2 Solution of the time-dependent kinetic equation

Proposition I.3.2 can now be proved. Together with Corollary 1 it establishes a correspondence between the Cauchy problem (I.3.1) and the Fokker-Plank equation (I.3.8).

Proof of Proposition I.3.2. Consider the stochastic process $\{V(t), W(t); t \geq 0\}$, where

1. $V(t) = \left(X(t), \mathcal{N}(t), a(t)\right)$ is the process defined in the previous section;
2. $W(t)$ is defined as

$$\dot{W}(t) = 2\gamma(V(t)), \quad W(0) = 0, \tag{I.3.23}$$

and such that it is continuous for all $t > 0$, which implies

$$W(t) = 2\int_0^t \gamma(V(s))ds.$$

Notice that the hypothesis $\gamma \geq \Gamma > 0$ implies that $W(t) \geq 0$. With analogous techniques to those used in the proof of Theorem I.1 one can compute the infinitesimal generator $\mathcal{A}_\gamma$ of $\{V(t), W(t)\}$, which acts on functions $\varphi \in C_b^1(\mathbb{R}^d \times \mathbb{R}^d \times M \times [0, +\infty))$ as

$$\mathcal{A}_\gamma \varphi(v, w) = \mathcal{A}\varphi(v, w) + 2\gamma(v)\frac{\partial \varphi}{\partial w}(v, w). \tag{I.3.24}$$

Proposition I.3.1 implies that the probability law ν_t of the process $\{V(t), W(t)\}$ satisfies

$$\nu_t(\varphi) = \nu_0(\varphi) + \int_0^t \nu_s(\mathcal{A}_\gamma \varphi) ds,$$

where the action of ν_t on a test function φ is given by

$$\nu_t(\varphi) = \mathbb{E}_{0,\nu_0}[\varphi(V(t), W(t))].$$

For $f \in C_b^1(\mathbb{R}^d \times \mathbb{R}^d \times M)$, consider now a test function φ of the form

$$\varphi(v, w) = \mathrm{e}^{-w} f(v),$$

which is in C_b^1 since $w \in [0, +\infty)$. Then the above equation for ν_t implies that

$$\begin{aligned} &\mathbb{E}_{0,\nu_0}\left[\mathrm{e}^{-2\int_0^t \gamma(V(s))ds} f(V(t))\right] \\ &\quad = \nu_0(f) + \int_0^t \mathbb{E}_{0,\nu_0}\left[\mathrm{e}^{-2\int_0^s \gamma(V(s'))ds'}\big(\mathcal{A}f(V(s)) - 2\gamma(V(s))f(V(s))\big)\right] ds. \end{aligned} \tag{I.3.25}$$

With the choice $\nu_0 = \mu_0 \times \delta_0$, the last expression above amounts to

$$\tilde{\mu}_t(f) = \tilde{\mu}_0(f) + \int_0^t \tilde{\mu}_s(\mathcal{A}f - 2\gamma f) ds,$$

which concludes the proof. □

Proof of Corollary 1. In view of Proposition I.3.1, $\tilde{\mu}_t$ satisfies equation (I.3.16) for every $f \in C_b^1(\mathbb{R}^d \times \mathbb{R}^d \times M)$. If one chooses in particular $f = C \cdot g$, where

$C = u_0(\mathbb{R}^d \times \mathbb{R}^d \times M)$ and $g \in C_b^1(\mathbb{R}^d \times \mathbb{R}^d \times M)$, one obtains, in view of the linearity of the operator $\mathcal{A}$,

$$u_t(g) = u_0(g) + \int_0^t u_s\big((\mathcal{A} - 2\gamma)g\big)ds. \tag{I.3.26}$$

Since $\tilde{\mu}$ is non-negative, and $C > 0$, then $u_t = C\tilde{\mu}_t$ is also non-negative. □

Notice that (I.3.26) amounts to a weak formulation of problem (I.3.1), in view of the definitions (I.3.10)-(I.3.12). Therefore, a direct correspondence between the weak formulation of (I.3.1) and (I.3.8) is established. If in addition $u_t = (u_{\alpha,t})$ is absolutely continuous with respect to the Lebesgue measure, one can show that

$$\mathcal{A}^* u_{\alpha,t} = -\{H_\alpha, u_{\alpha,t}\} + \sum_\beta \mathcal{S}_{\alpha\beta}(u_{\beta,t}),$$

where with an abuse of notation $u_{\alpha,t}$ also denotes the Radon-Nikodym derivative of the measure $u_{\alpha,t}$ with respect to the Lebesgue measure. This gives a correspondence between (I.3.1) and (I.3.17).

I.3.3.3 Conservation of the dispersion manifold

The considered stochastic process is a combination of Hamiltonian dynamics and a jump process. Under assumption I.2, the trajectories of the process enjoy the same energy conservation property as the underlying Hamiltonian system, provided that one accounts for the jumps properly. This property is critical for the construction of a solution of (I.2.16).

Proof of Theorem I.2. Let $\{T_j;\ j > 0\}$ be the sequence of the time of the jumps, with $T_0 = 0$. The result is proved by induction over the intervals $[T_j, T_{j+1})$:

(i) $H(X(0), \mathcal{N}(0), a(0)) = 0$ from the hypothesis of the Theorem. Then, for $t \in [0, T_1)$, $a(t) = a(0)$ and $(X(t), \mathcal{N}(t))$ are obtained by integration of

Hamilton equations with Hamiltonian H, so that

$$H(X(t), \mathcal{N}(t), a(t)) = 0, \quad t \in [0, T_1).$$

(ii) Assume now that the result holds for $t < T_j$. In particular, this means that

$$H(X_j^-, N_j, \alpha_j^-) = 0.$$

By definition of the stochastic process $X_j^+ = X_j^-$, while N_j^+ and α_j^+ are drawn from the probability distribution (I.3.12). Assumption I.2 implies that

$$(X_j^+, N_j^+, \alpha_j^+) \in \mathcal{C}, \tag{I.3.27}$$

By the same argument used for (i) one can show that $H(X(t), \mathcal{N}(t), a(t))$ is constant for $t \in [T_j, T_{j+1})$, and (I.3.27) implies that it is zero, which concludes the proof.

□

I.3.3.4 Solution of the radiative transport model for beams

At last, a solution of (I.2.16) can be constructed.

Proof of Theorem I.3. The two points can be proven:

(i) The assumption $\gamma \geq \Gamma > 0$ implies that

$$\int_0^t \gamma(X(s), \mathcal{N}(s), a(s)) ds \geq \Gamma t,$$

from which, being F_γ as in (I.3.14) for $f \in C_b(\mathbb{R}^d \times \mathbb{R}^d \times M)$, one obtains

$$\left| \mathbb{E}_{x,N,\alpha}[F_\gamma(X(t), \mathcal{N}(t), a(t))] \right| \leq \mathrm{e}^{-2\Gamma t} \|f\|_\infty.$$

Therefore, recalling that

$$u_t(f) = \sum_{\alpha\in M} \int_{\mathbb{R}^d\times\mathbb{R}^d} \mathbb{E}_{x,N,\alpha}[F_\gamma(X(t),\mathcal{N}(t),a(t))]u_0(dx,dN,\alpha),$$

one gets the estimate

$$\begin{aligned} |u_t(f)| &\leq \sum_{\alpha} \int_{\mathbb{R}^d\times\mathbb{R}^d} \left|\mathbb{E}_{x,N,\alpha}[F_\gamma(X(t),\mathcal{N}(t),a(t))]\right| u_0(dx,dN,\alpha) \\ &\leq \sum_{\alpha} \int_{\mathbb{R}^d\times\mathbb{R}^d} \mathrm{e}^{-2\Gamma t}\|f\|_\infty u_0(dx,dN,\alpha) = C\|f\|_\infty \mathrm{e}^{-2\Gamma t}, \end{aligned} \tag{I.3.28}$$

so that $t \mapsto u_t(f)$ is in $L^1(\mathbb{R}_+)$ for every $f \in C_b(\mathbb{R}^d\times\mathbb{R}^d\times M)$. The same inequality implies that the map $f \mapsto w(f)$ as defined in the statement is a continuous linear functional on $C_0 \subset C_b$, and therefore it defines a measure on $\mathbb{R}^d\times\mathbb{R}^d\times M$ in virtue of Riesz-Markov-Kakutani representation theorem (see for example [74, Theorem 2.14]).

(ii) The three different points in Definition I.4 can be proven separately:

(a) Consider a test function $f \in C_0^1(\Omega\times\mathbb{R}^d\times M)$, so that $u_0(f) = 0$, as u_0 is localized on Σ by the definition given in (I.3.2). Moreover, estimate (I.3.28) implies that

$$\lim_{t\to\infty} u_t(f) = 0,$$

and point (i) ensures that the integral in the definition of $w(f)$ is well defined, so that the limit for $t \to \infty$ of equation (I.3.18) gives

$$w(\mathcal{A}f - 2\gamma f) = 0,$$

which means that w satisfies (I.2.16a) in the sense of distributions.

(b) For what concerns the dispersion relation, since u_0 satisfies $(Hu_0)(f) = 0$, the initial condition $\{X(0),\mathcal{N}(0),a(0)\}$ of each trajectory, sampled from the measure u_0, necessarily belongs to $\{H(x,N,\alpha) = 0\}$.

As a consequence, in virtue of Theorem I.2, H is constant and equal to zero along the trajectories that originate at such points. But now (cf., [43, p.35]), for $f \in C_0^\infty(\mathbb{R}^d \times \mathbb{R}^d \times M)$,

$$u_t(Hf) = \sum_\alpha \int_{\mathbb{R}^d \times \mathbb{R}^d} \mathbb{E}_{x,N,\alpha}[H(X(t), \mathcal{N}(t), a(t)) \times F_\gamma(X(t), \mathcal{N}(t), a(t))] u_0(dx, dN, \alpha),$$

which is zero as $H(X(t), \mathcal{N}(t), a(t)) = 0$ for every $t \geq 0$. Therefore,

$$w(Hf) = \int_0^{+\infty} u_t(Hf)dt = 0,$$

and w satisfies the dispersion relation (I.2.16b) in the sense of distributions.

(c) Consider, for $f \in C_0^\infty(U \times M)$,

$$u_t(f) = \sum_{\alpha' \in M} \int_{\mathbb{R}^d \times \mathbb{R}^d} \mathbb{E}_{x',N',\alpha'}[\mathrm{e}^{-2\int_0^t \gamma(X(s),\mathcal{N}(s),a(s))ds} \times f(X(t), \mathcal{N}(t), a(t))] u_0(dx', dN', \alpha'),$$

so that the integrand is localized in U. The assumption $\sigma_{\alpha\beta} = 0$ in U implies that the trajectories of the markers are deterministic, and denoting

$$x = (y, z) \in \mathbb{R}^{d-1} \times \mathbb{R}, \quad N = (N_y, N_z) \in \mathbb{R}^{d-1} \times \mathbb{R},$$

the assumption $\nabla_x H_\alpha = 0$ leads to the following analytic expressions

$$\begin{aligned} X(t) &= (Y(t), Z(t)) = (y' + V_\alpha^y(N)t, z' + V_\alpha^z(N)t), \\ \mathcal{N}(t) &= (\mathcal{N}_y(t), \mathcal{N}_z(t)) = (N_y', N_z') = N', \\ a(t) &= \alpha', \end{aligned} \tag{I.3.29}$$

where $(V^y_\alpha(N), V^z_\alpha(N)) = (\nabla_{N_y} H_\alpha(N), \partial_{N_z} H_\alpha(N))$. Notice that the assumption $\partial_{N_z} H_\alpha > 0$ implies $V^z_\alpha > 0$. In particular the trajectories in U are straight lines, constant in N, so that

$$(X(t), \mathcal{N}(t), a(t)) \in U \times M \\ \Rightarrow (X(s), \mathcal{N}(s), a(s)) \in U \times M, \ \ \forall s < t, \quad \text{(I.3.30)}$$

as U contains the whole half-space $\{z < 0\}$, and $V^z_\alpha(N) > 0$. By *reductio ad absurdum* one can prove that (I.3.30) implies

$$(X(s), \mathcal{N}(s), a(s)) \notin U \times M \\ \Rightarrow (X(t), \mathcal{N}(t), a(t)) \notin U \times M \ \ \forall t > s, \quad \text{(I.3.31)}$$

so that if a trajectory exits $U \times M$ at a time $t = t^*$ (i.e., if $Z(t^*) \geq z^*$), it cannot enter it again. In particular this implies that one can plug the analytic expressions (I.3.29) in the expression for u_t for all $t > 0$, as the trajectories originate at points in U and f localizes the integrand. Recalling that $u_0 = (u^0_\alpha)_{\alpha \in M}$, where u^0_α is given by (I.3.2), one can write

$$u_t(f) = \sum_{\alpha \in M} \int \mathrm{e}^{-\psi(t,y',z',N,\alpha)} f(y' + V^y_\alpha(N)t, z' + V^z_\alpha(N)t, N, \alpha) \\ \times V^z_\alpha(N) dy' \times \delta(dz') \times w^0_\alpha(y', dN),$$

where the notation

$$\psi(t, y', z', N, \alpha) = 2 \int_0^t \gamma(y' + V^y_\alpha(N)s, z' + V^z_\alpha(N)s, \alpha) ds$$

was introduced to simplify the expression. At this point one can perform the change of coordinates

$$y = y' + V^y_\alpha(N)t, \quad z = z + V^y_\alpha(N)t,$$

which returns

$$u_t(f) = \sum_{\alpha\in M} \int \mathrm{e}^{-\tilde{\psi}(t,y,z,N,\alpha)} f(y,z,N,\alpha) V_\alpha^z(N) \\ \times dy \times \delta_{V_\alpha^z(N)t}(dz) \times w_\alpha^0(y - V_\alpha^y(N)t, dN),$$

where $\tilde{\psi}$ simply denotes ψ in the new coordinates. Plugging this last expression in the definition of w one obtains

$$\begin{aligned} w(f) &= \int_0^{+\infty} u_t(f) dt \\ &= \sum_{\alpha\in M} \int_0^{+\infty} \int \mathrm{e}^{-\tilde{\psi}(t,y,z,N,\alpha)} f(y,z,N,\alpha) \\ &\quad \times V_\alpha^z(N) dy \times \delta_{V_\alpha^z t}(dz) \times w_\alpha^0(y - V_\alpha^y(N)t, dN) \times dt \\ &= \sum_{\alpha\in M} \int_0^{+\infty} \int \mathrm{e}^{-\tilde{\psi}(\tau/V_\alpha^z(N),y,z,N,\alpha)} f(y,z,N,\alpha) \\ &\quad \times dy \times \delta_\tau(dz) \times w_\alpha^0(y - V_\alpha^y(N)/V_\alpha^z(N)\tau, dN) \times d\tau, \end{aligned}$$

where in the last step the change of coordinate

$$\tau = V_\alpha^z(N)t$$

was applied. One can observe that the integrand is absolutely integrable (cf., [91, Corollary 1.7.23] and therefore one can apply Fubini's theorem and exchange the order of integration. Defining

$$v_{\tau,z}(f) = \sum_{\alpha\in M} \int_{\mathbb{R}^{d-1}} \mathrm{e}^{-\tilde{\psi}(\tau/V_\alpha^z(N),y,z,N,\alpha)} f(y,z,N,\alpha) \\ \times w_\alpha^0(y - V_\alpha^y/V_\alpha^z(N)\tau, dN) \times dy,$$

one can write

$$w(f) = \int_{\mathbb{R}_+\times\mathbb{R}} v_{\tau,z}(f)\delta_\tau(dz)d\tau = \int_{\mathbb{R}_+\times\mathbb{R}} v_{\tau,z}(f)\delta_z(d\tau)dz$$
$$= \int_{\mathbb{R}_+\times\mathbb{R}_+} v_{\tau,z}(f)\delta_z(d\tau)dz$$

where the last step follows from the fact that $\tau > 0$ by construction.

Consider now $\tilde{U} = U \cap \bar{\Omega}$, where

$$\tilde{U} = U \cap \bar{\Omega} = \{(y, z, N_y, N_z) \in U \mid z \geq 0\}.$$

$\tilde{U}$ is a neighborhood of Σ_+ in $\bar{\Omega} \times \mathbb{R}^{d-1} \times \mathbb{R}_+$, and for test-functions $f \in C_0^\infty(\tilde{U} \times M)$ one can define

$$\tilde{w}_z(f) = v_{z,z}(f), \qquad z \geq 0. \tag{I.3.32}$$

The calculation above shows that

$$w(f) = \int_{\mathbb{R}_+} \tilde{w}_z(f)dz,$$

and moreover w depends smoothly on z, which proves the continuity of w in z in $\tilde{U}$, according to Definition I.1. This implies that the restriction of w to Σ_+ is well defined, namely, given $g \in C_0(\Sigma_+ \times M)$,

$$w|_{\Sigma^+}(g) = \tilde{w}_0(g).$$

Looking at a single component w_α acting on $g_\alpha = g(\cdot, \alpha)$, one gets

$$w_\alpha|_{\Sigma_+}(g) = \int_{\mathbb{R}^{d-1}\times\mathbb{R}_+\times\mathbb{R}^{d-1}} g_\alpha(y, N)w_\alpha^0(y, dN_y, dN_z) \times dy,$$

which is exactly the weak formulation of the boundary condition I.2.16c.

□

I.3.4 Definition of the numerical scheme

From the results and the discussion of the previous section, the structure of a numerical scheme suitable for the solution of the wave kinetic equation emerges naturally. The scheme can be resumed in the following steps:

S.1 The sequence $\{T_j, j \geq 0\}$ of the times of the jumps is taken as that of a Poisson process of parameter $\bar{\lambda} = \sup_{x,N,\alpha} \lambda(x, N, \alpha)$.

S.2 A number N_m of markers are sampled according to (I.2.16b) and (I.2.16c) (or equivalently, to the initial condition of (I.3.1)).

S.3 Each marker $\{(X_i(t), \mathcal{N}_i(t), a_i(t))\}$ follows, for $t \in [T_j, T_{j+1})$, the dynamics prescribed by the Hamiltonian H_α, with $\alpha = a_i(T_j)$ (cf., I.3.4).

S.4 The trajectory of each marker is weighted by a factor

$$g_{i,\alpha} = \exp\left(-2\int_{T_j}^{T_{j+1}} \gamma_\alpha(X(s), \mathcal{N}(s))ds\right), \quad \alpha = a(T_j).$$

S.5 At the time $t = T_{j+1}$ a jump occurs as described in Chapter I.3, and the new values α_{j+1}^+ and N_{j+1}^+ are extracted from the density $\sigma_{\alpha\beta}(x, N; dN')/\lambda_\alpha$.

S.6 The procedure is iterated in the interval $[T_{j+1}, T_{j+2})$ with the new initial condition.

Remark I.3.4.1 (Numerics.)**.** *Some steps in the procedure are non-trivial from the implementation point of view:*

- *Whether an event occurs, is decided comparing the probability of that event with a random number extracted from a uniform distribution over* $[0, 1]$.
- *Sampling from non-trivial distributions is done using Metropolis-Hastings algorithm [13].*

I.4 Verification of the scheme and implementation in the `WKBeam` code

The scheme presented in Section I.3.4 has been designed for being ultimately implemented in `WKBeam` [101, 102], a code for simulations of electron-cyclotron beams in fusion plasmas, which takes into account realistic axisymmetric machine geometries (e.g., ASDEX-Upgrade [97], ITER [34], TCV [93], TORPEX [94]). Before this step (cf. Section I.4.2.2), a stand-alone test model was developed in order to perform verification studies in a simpler framework, which still retains the structure of the general problem.

I.4.1 Stand-alone test model

In order to test the scheme, the analysis is focused on the following problem:

$$\begin{cases} \dfrac{\partial u_\alpha}{\partial t}(t,x,y) + \{H_\alpha, u_\alpha\}(t,x,y) = \displaystyle\sum_{\beta\in M} \tilde{\mathcal{S}}_{\alpha\beta}(u)(t,x,y), \quad x,y\in\mathbb{R}, t\in[0,T), \\ u_\alpha(0,x,y) = u^0_\alpha(x,y), \qquad\qquad \alpha\in M, \end{cases} \tag{I.4.1}$$

where x represents the position, y is the associated momentum and α,β model the polarization mode, varying over a finite set M. The Poisson bracket on

the left-hand side is given by

$$\{f, g\} = \frac{\partial f}{\partial y}\frac{\partial g}{\partial x} - \frac{\partial f}{\partial x}\frac{\partial g}{\partial y}.$$

For what concerns the scattering operator

$$\tilde{\mathcal{S}}_{\alpha\beta}(u)(t, x, y) = \int_{\mathbb{R}} \sigma_{\alpha\beta}(x, N', N) u_\beta(t, x, N') dN' \\ - \sigma_{\alpha\beta}(x, N, N') u_\alpha(t, x, N)] dN',$$

the cross-sections $\sigma_{\alpha\beta}$ are taken in the form

$$\sigma_{\alpha\beta}(x, y, y') = \sigma_{\alpha\beta}(x, y - y') = s_{\alpha\beta} \mathrm{e}^{-L_c^2 (y-y')^2},$$

where $s_{\alpha\beta}$ are constants that quantify the scattering intensity and L_c plays the role of a correlation length of the fluctuations of the medium. Under these assumptions, the scattering operator actually acts as a convolution, so that a pseudo-spectral solver can be used to build a highly resolved reference solution. A reconstruction of the measure of the stochastic process from the Monte-Carlo data is obtained through the kernel density estimation (KDE) [80].

I.4.1.1 Single mode

First of all, the case of a single polarization mode is considered, so that one is left with one equation and the indexes α, β can be omitted. A simple advection model is considered, where the Hamiltonian H is such that the associated Hamiltonian field is

$$b = (\partial_y H, -\partial_x H) = (-1, 0).$$

A Gaussian initial condition is considered,

$$u^0(x, y) = a_0 \exp\left[-\frac{(x - x_0)^2}{a_x^2} - \frac{(y - y_0)^2}{a_y^2} \right],$$

where the amplitude a_0 and the widths a_x, a_y are fixed and specified in Table I.4.1, together with the scattering intensity s and the correlation length L_c.

Quantity	**Symbol**	**Value**
Parameters of the model		
Hamiltonian field	$b = (\partial_y H, -\partial_x H)$	$(-1, 0)$
Scattering intensity	s	8
Correlation length	L_c	3
Initial condition		
Amplitude	a_0	2
Width	(a_x, a_y)	$(0.3, 1)$
Parameters of the numerical scheme		
Number of markers	N_m	$5 \cdot 10^{-5}$

Table I.4.1: Parameters of the numerical test for a single propagation mode.

In this case an analytic approximation of the solution can be found in the form

$$u(t, x, y) \approx U_0(x + t) \exp\left[-\frac{(y - y_0)^2}{\tilde{a}_y(t)^2}\right], \tag{I.4.2}$$

for some function U_0 independent of y, valid asymptotically in the limit $a_y L_c \to \infty$, where

$$\tilde{a}_y(t) = a_y \sqrt{1 + C/a_y^2 L_c^2},$$

with $C = (s\sqrt{\pi})/L_c$. In fact equation (I.4.1), with the assumptions above, amounts to

$$\partial_t u - \partial_x u = f * u - Cu,$$

where $f = f(y) = s \exp(-L_c^2 y^2)$ and $C = \int_{\mathbb{R}} f(y) dy$. Fourier transforming in y gives

$$\partial_t \hat{u} - \partial_x \hat{u} = (\hat{f} - C)\hat{u},$$

which can be solved with the method of characteristics, giving

$$\hat{u}(t, x, \eta) = \hat{u}_0(x + t, \eta) \exp\left((\hat{f} - C)t\right).$$

Substituting the expressions for $\hat{f}$ and $\hat{u_0}$ in this last expression, one gets

$$\hat{u}(t,x,\eta) = \exp\left(-\frac{(x+t-x_0)^2}{a_x^2} - \frac{a_y^2\eta^2}{4} + \mathrm{i}\eta y_0\right)\exp\left(C\big(\mathrm{e}^{-\frac{\eta^2}{4L_c^2}}-1\big)t\right).$$

Normalizing η to the width of the initial condition a_y, the argument of the second exponential can be approximated, in in the limit $a_y L_c \to \infty$, as

$$C\left(\exp\left(-\frac{\eta^2}{(a_y L_c)^2}\right)-1\right)t \approx -C\frac{\eta^2}{(a_y L_c)^2}t,$$

where with an abuse of notation η denotes now the normalized variable. The expression (I.4.2) follows by substituting this last approximation in the expression for $\hat{u}$ and by application of the inverse Fourier transform.

In Figure I.4.1 the initial condition (right-most contours in each figure) evolves towards the left-hand side, being scattered in the y-direction. One can observe a good qualitative agreement between the reference solution (left) and the one obtained with the presented scheme (right). The black curves in the plot are parametrized by

$$y(t) = y_0 \pm \tilde{a}_y(t),$$

and they match the contours $u(t,x,y) = \mathrm{e}^{-1}$ in both cases, showing good agreement between the Monte-Carlo solution and the analytic approximation.

I.4.1.2 Multiple modes

The case of two different polarization modes is now considered, namely, $\alpha \in M = \{0,1\}$. In absence of analytic solutions for this case, the only comparison will be with the pseudo-spectral solution. Again, a Gaussian initial conditions of the form

$$u_\alpha^0(x,y) = a_{0,\alpha}\exp\left[-\frac{(x-x_0)^2}{a_{x,\alpha}^2} - \frac{(y-y_0)^2}{a_{y,\alpha}^2}\right], \quad \alpha \in M$$

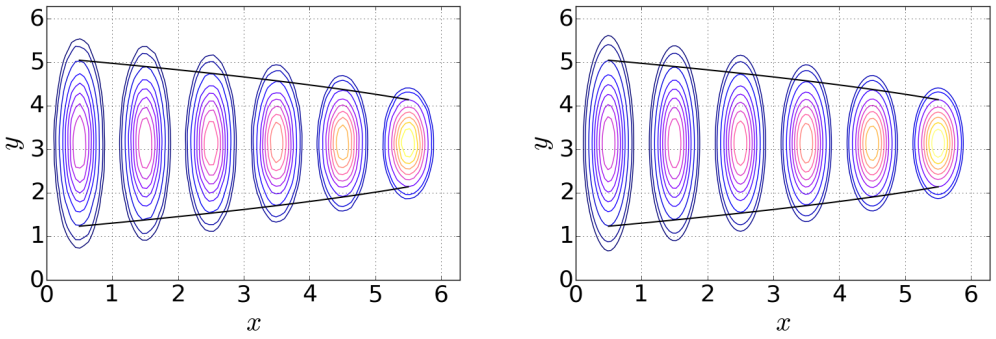

(a) Reference solution. (b) Monte-Carlo (KDE).

Figure I.4.1: Contours of the solution, propagating towards the left-hand side, at different times. The black curves refer to the analytic solution, and match the contours $u = \mathrm{e}^{-1}$ at any time. Note that the solution follows the Hamiltonian field $(-1, 0)$ in the x-direction, while scattering determines a broadening in the y-direction.

is considered. In what follows the choice $a_{0,0} = 1$ and $a_{0,1} = 0$ is made, so that the whole energy belongs initially to the mode $\alpha = 0$. This choice implies that the solution for the mode $\alpha = 1$, being zero at $t = 0$, is initially affected by Monte-Carlo noise. This kind of initial condition is also relevant from the point of view of the main application to waves in fusion plasmas, as typically waves with a selected polarization mode are used in the experiments. The Hamiltonians H_α are chosen in such a way that the Hamiltonian vector fields b_α are

$$b_0 = (\partial_y H_0, -\partial_x H_0) = (-1, -1/2),$$
$$b_1 = (\partial_y H_1, -\partial_x H_1) = (-1, +1/2),$$

so that the free propagation of the two modes is visibly different. The matrix of scattering coefficients has non-zero off-diagonal entries, so that there is a non-zero probability of energy exchange between the two modes. A summary of the parameters is reported in Table I.4.2.

In Figure I.4.2 good qualitative agreement between the Monte-Carlo solution

Quantity	Symbol	Value
Parameters of the model		
Hamiltonian fields	$b_0 = (\partial_y H_0, -\partial_x H_0)$	$(-1, -1/2)$
	$b_1 = (\partial_y H_1, -\partial_x H_1)$	$(-1, +1/2)$
Scattering matrix	$s = (s_{\alpha\beta})$	$\begin{pmatrix} 1 & 0.5 \\ 0.5 & 2 \end{pmatrix}$
Correlation length	L_c	1.5
Initial condition		
Amplitudes	$(a_{0,0}, a_{0,1})$	$(1, 0)$
Widths	$(a_{x,0}, a_{y,0})$	$(0.3, 1)$
	$(a_{x,1}, a_{y,1})$	$(0.3, 1)$
Parameters of the numerical scheme		
Number of markers	N_m	10^{-6}

Table I.4.2: Parameters of the numerical test for two propagation modes.

(right) and the reference one (left) can be observed, for both the initialized mode ($\alpha = 0$, top row) and the secondary one ($\alpha = 1$, bottom row). The contours represent the solution in phase-space at different times, where the propagation is towards the left-hand side. The mode $\alpha = 1$ is absent at $t = 0$, while it appears due to cross-polarization scattering for $t > 0$. Both modes follow the corresponding Hamiltonian field (grey lines), and scatter in the y-direction.

I.4.1.3 Convergence of the scheme

In order to perform a more quantitative analysis of the scheme, its convergence is now analyzed. This is done by computing the scaling of the error with respect to the number of markers sampled for the Monte-Carlo solution. In order to do that, a measure is associated to both the reference solution and the Monte-Carlo one, in the following way:

- For the reference pseudo-spectral solution u_α^{PS},

$$\mu_{\alpha,t}^{PS}(\Omega) = \int_\Omega u_\alpha^{PS}(t, x, y) dx\, dy. \tag{I.4.3}$$

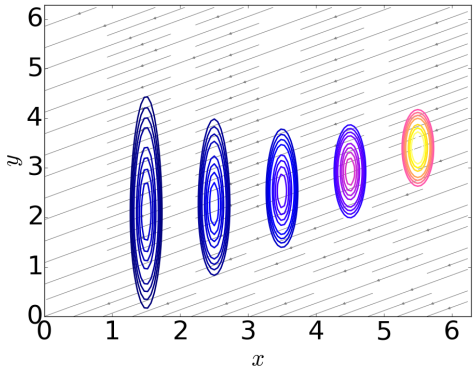

(a) Reference solution, mode $\alpha = 0$.

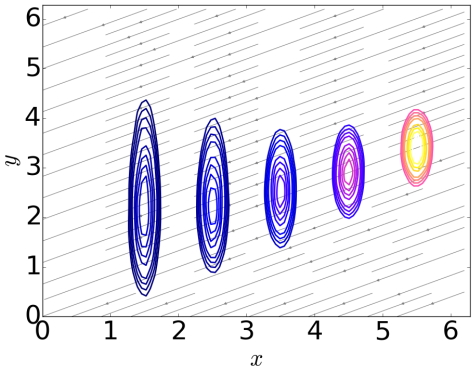

(b) Monte-Carlo (KDE), mode $\alpha = 0$

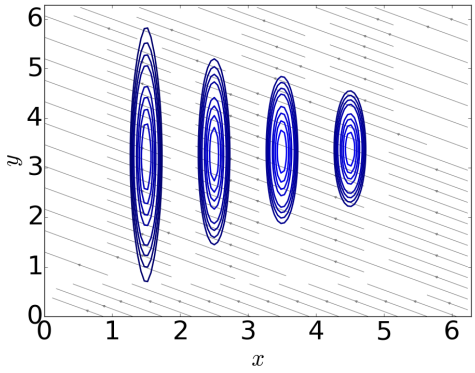

(c) Reference solution, mode $\alpha = 1$.

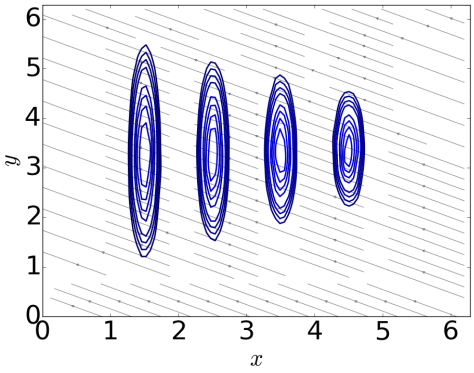

(d) Monte-Carlo (KDE), mode $\alpha = 1$

Figure I.4.2: Contours of the solution, propagating towards the left-hand side, at different times. The "secondary" mode appears for $t > 0$ due to scattering, which determines also a broadening in the y-direction.

- For the Monte-Carlo solution corresponding to N_m markers,

$$\mu_{\alpha,t}^{N_m}(\Omega) = \sum_{i=1}^{N_m} \delta_{(X_i(t),Y_i(t))}(\Omega)\delta_{a(t)}(\alpha), \tag{I.4.4}$$

  where $(X_i(t), Y_i(t))$ are the coordinates of the i-th marker at the time t and δ_z denotes the Dirac measure centered at z. The measure $\mu_{\alpha,t}^{N_m}$ counts the markers which at the time t belong to the mode α and are located in Ω.

For a fixed value of t, the error on each individual mode is defined as

$$\epsilon_{\alpha,t}(N_m) := \max_K \left| \mu^{N_m}_{\alpha,t}(K) - \mu^{PS}_{\alpha,t}(K) \right|,$$

where K runs over the cells of the dual grid of the pseudo-spectral solution. Analogously, one can define the error on the total energy as

$$\epsilon_t(N_m) := \max_K \left| \sum_\alpha (\mu^{N_m}_{\alpha,t}(K) - \mu^{PS}_{\alpha,t}(K)) \right|.$$

Figure I.4.3 shows how the error decays, as expected for a Monte-Carlo scheme,

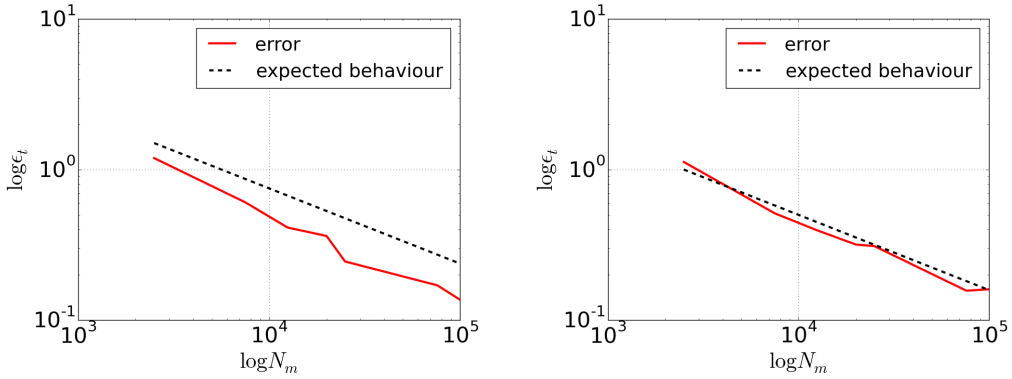

(a) Single mode, $s = -0.57$.

(b) Multiple modes, $s = -0.52$.

Figure I.4.3: Convergence tests at $t = 1$. (a) Convergence of the scheme in the case of one polarization mode. (b) Convergence for the case of two polarization modes, where the error was computed on the total energy. In both cases s represents the slope of the best linear fit in logarithmic scale, so that ϵ_t goes to zero as N_m^s.

as $1/\sqrt{N_m}$, in both the single mode and multiple modes cases, where left-advection was considered for all modes and the error on the total energy was considered (sum of the two modes). The expected convergence rate is achieved also if one considers the modes separately, provided that the statistics of each mode is sufficiently good, which is the case in this test-model for large values of t (cf., Figure I.4.4).

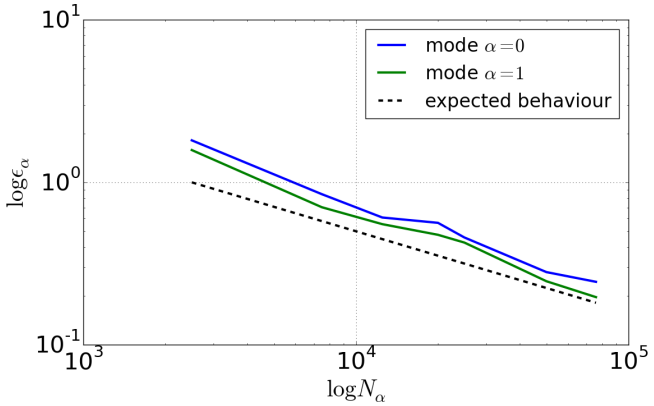

Figure I.4.4: Convergence for the two modes considered separately, at $t = 2$. Here the convergence rate (cf., I.4.3) is $s = -0.58$ for the mode $\alpha = 0$ and $s = -0.59$ for the mode $\alpha = 1$, with s defined as in Figure I.4.3.

I.4.2 Implementation in `WKBeam`

After the successful verification of the scheme and its convergence in the presented stand-alone test model, some realistic application of the wave kinetic equation and its solution can be showed, in the framework of the `WKBeam` code. This code is devoted to simulate the behaviour of electron-cyclotron beams in nuclear fusion relevant scenarios. Although, the scheme actually implemented in the physics code presents some differences with respect to the one derived in this work and used in the tests so far. Those differences will be motivated and analyzed before we presenting the actual application of `WKBeam`.

I.4.2.1 Heuristic approximation of the scheme

An example of numerical solution of the wave scattering problem based on the wave kinetic equation can be found in [82], where a single polarization mode propagating in an idealized tokamak is considered. The numerical scheme used in the cited work presents some differences with respect to the one described in this manuscript: instead of drawing a certain sequence of random times for the jumps, the scattering events are “accumulated” at the end of intervals of

fixed size. A generalization of such heuristic scheme to the case of multiple polarization modes would be the following:

S'.1 *The interval* $[0, T)$ *is divided in sub-intervals* $[T_j, T_{j+1})$ *of fixed size* Δt*.*

S'.2 A number N_m of markers are sampled (cf., **S.2**).

S'.3 Each marker $\{(X_i(t), \mathcal{N}_i(t), a(t))\}$ follows, for $t \in [T_j, T_{j+1})$, the Hamiltonian H_α (cf., **S.3**).

S'.4 The trajectory of each marker is weighted by a factor

$$g_{i,\alpha} = \exp\left(-2\int_{T_j}^{T_{j+1}} \gamma_\alpha(X(s), \mathcal{N}(s))ds\right), \quad \alpha = a(T_j),$$

as in **S.4**.

S'.5 *At the time of the jump* T_{j+1}*, the number of scattering events in the interval is extracted from a Poisson process of parameter* $\bar{\lambda}\Delta t$*.* For each of such events, it is decided whether scattering actually occurs, and the new values $a(T_{j+1}^+)$ and $\mathcal{N}(T_{j+1}^+)$ are decided as in **S.5**.

S'.6 The procedure is iterated (cf., **S.6**).

The steps in italic highlight the differences between the heuristic scheme and the rigorous one. This modified version of the scheme is the one actually implemented in `WKBeam`: the first version of the code, previous to this work, was limited to a single polarization mode, and previous works in the field (e.g., [82]) have been taken into account in the choice of the numerical scheme to implement. At the moment of extending the code to account for cross-polarization scattering, it was decided to test the heuristic scheme first, in order not to alter the original structure of the code. Therefore, the modified scheme described in this section was implemented. Numerical tests have been performed on the modified scheme, implementing it in the same stand-alone test model introduced in the previous section: a convergence study was portrayed in the exact same way as described in Section I.4.1.3, giving the same results for a

choice of $\Delta t = 10^{-2}$ [23, Figure 2]. Moreover, a scan over different values of Δt was performed, looking at the scaling of the following quantities:

1. The error of the approximated scheme with respect to the rigorous one, as a function of Δt, at different fixed values of t (Figure I.4.5a);

2. The error of both schemes with respect to the pseudo-spectral solution, as a function of t, for different values of Δt (I.4.5b).

For both tests the error is defined as for the convergence, with reference solution given by that obtained with the rigorous scheme in point 1., and the pseudo-spectral one in point 2. No significant divergence between the two schemes appears for values of Δt up to 10^{-1}. In conclusion, the two schemes agree if the parameter Δt is small enough so that, up to selecting this parameter carefully, the heuristic scheme can be used without major drawbacks.

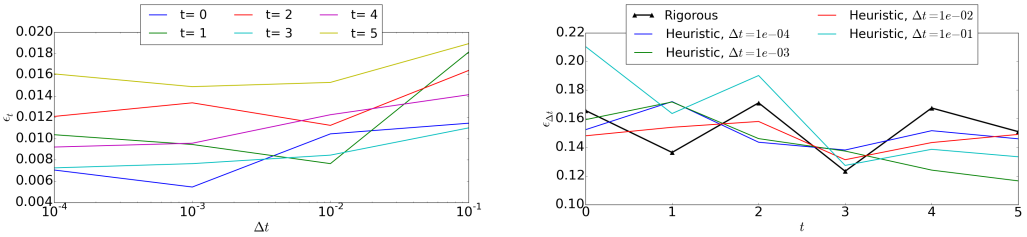

(a) Comparison between the heuristic scheme and the exact one: the error ϵ_t at a fixed time t is expressed as a function of Δt. Different values of t are represented. For all times considered the error is comparable to the sampling error ($t = 0$ case).

(b) Comparison of both schemes with the reference pseudo-spectral solution: the error $\epsilon_{\Delta t}$ at a fixed value of Δt is expressed as a function of t. For all considered cases the heuristic scheme is comparable to the rigorous one.

Figure I.4.5: Tests for the heuristic scheme at different values of Δt.

I.4.2.2 Application to the `WKBeam` code

Finally the application of the wave kinetic equation to nuclear-fusion-relevant problems can be shown. A case of propagation of electron-cyclotron waves in

a fusion plasma is presented, where "fusion plasma" denotes a plasma magnetically confined in a toroidal axisymmetric device (tokamak) (cf., Chapter 0.1 or [103] for more details). Axisymmetry ensures that the properties of the plasma are the same on each poloidal plane, so that the plasma equilibrium can be represented on a two-dimensional poloidal plane (characterized by a fixed value of the toroidal angle φ). Such plane is described by the coordinates (ρ, θ), where ρ plays the role of a radial coordinate and θ is the poloidal angle (cf., Figure I.4.6).

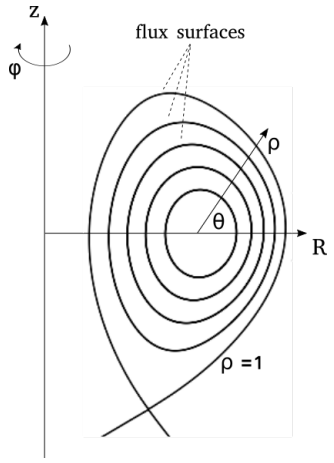

Figure I.4.6: Magnetic flux surfaces in a poloidal section of a tokamak machine. Note that the radial coordinate $\rho = \sqrt{\psi}$, where ψ is the so called magnetic poloidal flux, the contours of which are the flux surfaces represented in the figure. The surface $\rho = 1$ is the separatrix, as it is the last closed flux surface and it delimits the region in which the plasma is confined.

For fusion relevant simulations, a high-frequency beam propagating through a turbulent plasma is considered. As discussed in Chapter I.1, turbulence is modeled as a set of random perturbations of a background density profile, over which an *ensemble* average is performed, so that the averaged beam is described by the radiative transport model presented in Chapter I.2. The Hamiltonians in the transport term are derived from the cold-plasma model [88], and a derivation of the form implemented in the code can be found in [101]. For what concerns turbulence, it enters the equations through the scattering cross-section, which is determined from the two-points spatial correlation function of the density fluctuations. This is assumed to be of the form

$$\mathbb{E}[\delta n_e(x), \delta n_e(x')] = n_e(\rho)^2 F^2(\rho, \theta) \mathrm{e}^{-\frac{1}{2}(x-x')^T A (x-x')}, \tag{I.4.5}$$

where ρ and θ are evaluated at $(x+x')/2$. The matrix A contains information about the geometry of the turbulence, namely, the correlation length in the directions parallel and perpendicular to the magnetic field, which are given as an input. The envelope F is also an input parameter, for the choice of which the code allows maximum freedom. The value of F in the so called *edge* region - namely, in the neighborhood of the $\rho = 1$ surface - is one of the most influential factors in determining the relevance of scattering, for what concerns the possible broadening of the beam and cross-polarization effects. It is also the most uncertain element in the state-of-the-art understanding of fusion plasmas, and intensive work is currently being done on both the experimental and theoretical sides to have more reliable data for what concerns turbulence in the edge region.

In the example that is presented here, a standard scenario of the tokamak ITER [34] is considered. For the envelope F the chosen model was extrapolated from experimental data taken from other machines (cf., [107]), and it is represented in Figure I.4.7a, together with the background density and temperature profiles:

$$F(\rho,\theta) = F(\rho) = \begin{cases} 0.02 & \rho < 0.95 \\ 0.18(\rho - 0.95)/(0.05) + 0.02 & 0.95 \leq \rho < 1 \\ 0.2 & \rho \geq 1. \end{cases}$$

For what concerns the beam, an O-mode electron-cyclotron wave is considered [6], carrying 1.0 MW of power, injected from the upper-launcher (cf., [29]), propagating through the plasma and being absorbed at the resonance $\omega = \omega_{ce}(x)$. The beam is injected with angles of 20° and 46.8° in the toroidal and poloidal direction, respectively, which is a configuration designed for ECCD. The beam is therefore not axisymmetric, and the problem is posed on the full three-dimensional domain. The propagation is affected by the fluctuations, which determine both a significant broadening of the O-mode beam and a small energy transfer to the X-mode [6], which is reflected at the cut-off. In

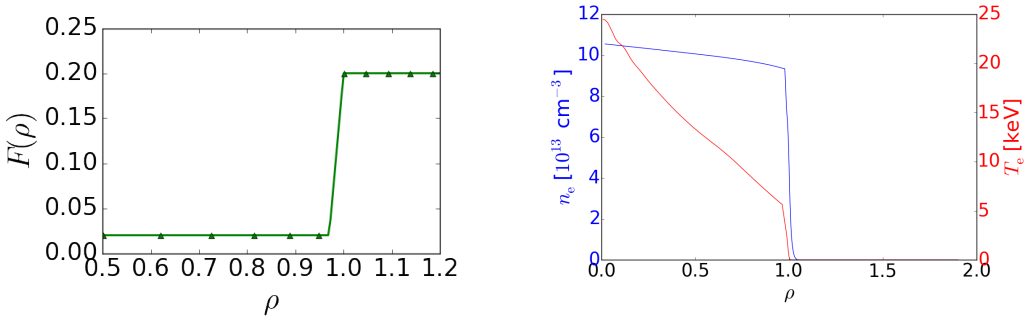

(a) (b)

Figure I.4.7: (a) Fluctuations envelope as a function of ρ. (b) Background density (red) and temperature (blue) profiles.

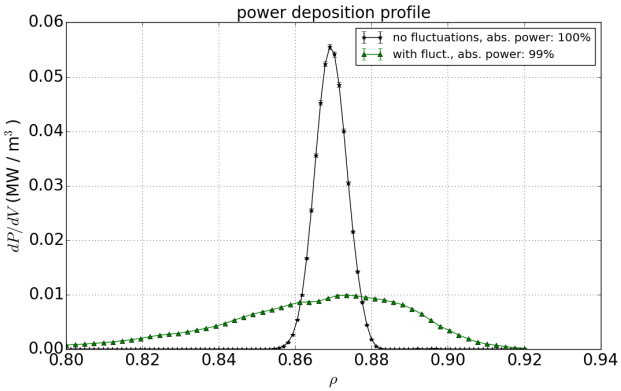

Figure I.4.8: Power deposition profile of the scattered beam, compared to the case where fluctuations are not taken into account. About 1% of the power is lost due to cross-polarization scattering.

Figure I.4.9 one can see a projection of the beam on the poloidal plane, and broadening can be clearly observed comparing the two cases of a turbulent and a quiet plasma (panel (b) and (a), respectively). Cross-polarization scattering instead is pretty small in this case (about 1 % of the injected power), and it is not visible in Figure I.4.9. The scattered power can be computed comparing the amount of power absorbed at the resonance (cf., equation (I.2.19)), to the injected power. Figure I.4.8) shows the power deposition profiles of a scattered beam and one propagating through a quiet plasma, together with a quantification of the fraction of absorbed power. Observe that in the scattered

case about 1% of the injected power is not absorbed at the resonance, providing evidence of a transfer of energy to the secondary mode (X-mode) due to cross-polarization scattering.

The value of these results from a physics point of view is purely qualitative, as part of the input parameters used for the calculation are not proven to reflect the actual physical conditions of ITER future operations. For more physically relevant applications of the code - and therefore, of the numerical scheme - one can refer to [83, 84].

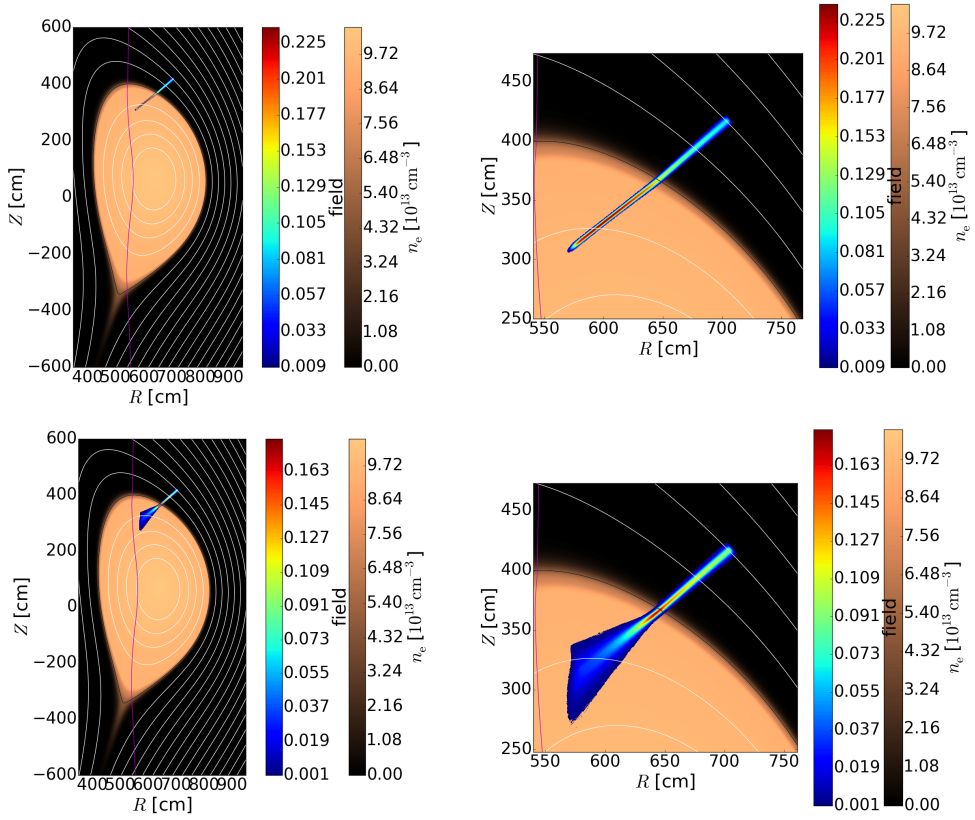

Figure I.4.9: Beam visualization in the poloidal plane (left) and zoom on the beam (right). The O-mode beams propagate towards the core and are absorbed at the resonance. Bottom row: turbulent plasma. The beam broadens significantly and a fraction of power is scattered to X-mode, which is reflected at its cut-off (not visible).

I.5 Conclusions and related projects

The results of this part lead to a rigorously derived and verified numerical scheme to solve a radiative transport model for wave beams in a random medium. The scheme (with some variations) is successfully implemented in the physics code `WKBeam`. Verification studies (benchmark) have been carried in order to determine the limits of validity of the approximations underlying the mathematical model behind WKBeam. Experimental validation of the code is part of the ongoing EUROfusion Enabling Research Project "Experimental, numerical and theoretical investigation of the physics of radio-frequency waves scattering by turbulent structures" (RFSCAT, Swiss Plasma Center, EPFL Lausanne).

Benchmark of the `WKBeam` code

For what concerns verification, a direct correspondence between the physics input and the validity conditions of the model in their mathematical formulation is not that easy to establish. A more practical way to deal with the problem is to compare the numerical results obtained from the radiative transport model with some other reliable solution, for different values of some critical parameters.

- *Fluctuations level (reference publication: [39]).*
  The derivation of (I.2.16) (cf., [35, 56, 101]) assumes the so called *Born scattering approximation* [5], which limits the applicability of the radiative transport model with respect to the amplitude of the density fluc-

tuations. In order to quantify the limits of validity of the Born approximation, an extensive benchmark of `WKBeam` with the finite-differences time-domain code IPF-FDMC [37] was done by Köhn: in the 2018 paper [39], it is shown how the radiative transport model can be trusted with fluctuations levels up to about 50% of the background density, which includes ITER nominal parameters.

- *Separation of dispersion manifolds (reference publication: [84]).* Assumption I.1 is crucial for the derivation of (I.2.16). On the other side, preliminary studies on cross-polarization scattering in the work by Snicker *et al.* [84] show that

$$\int \sigma_{\alpha\beta}(x, N, N')dN' \propto \mathrm{e}^{-(n_\alpha - n_\beta)^2},$$

with n_α as in Section I.2.3. This means that the effect is exponentially suppressed by the distance between the dispersion manifolds. Therefore cross-polarization scattering appears to be relevant only in the region where the modes degenerate. On the other hand by Assumption I.1 $|n_\alpha - n_\beta|$ must be bounded away from zero for the wave kinetic equation to be valid. This reflects in the first benchmark results: `WKBeam` tends to overestimate the effect, with respect to IPF-FDMC. The results obtained so far show how anyway this effect should not be significant in ITER-like scenarios [84].

Validation of `WKBeam`: the RF-SCAT project

The possibility to validate `WKBeam` with experimental data emerged in the context of the still ongoing EUROfusion Enabling Research project RFSCAT. The goal of the international collaboration coordinated by the SPC of EPFL, Lausanne, is to provide an experimental quantification of wave beam broadening due to scattering by density fluctuations in the tokamak TCV, with parameters that should reflect an ITER-relevant scenario. Direct measurements of these quantities has never been possible so far, while indirect measures have been attempted on the tokamak D-IIID [9, 10]. *Reference publications: [12, 11].*

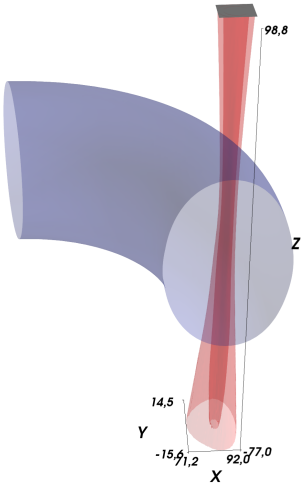

WKBeam simulation of the experimental setup at TCV [93] for the RF-SCAT project.

Part II

Reconstructing wave beams with Hagedorn packets

II.1 Reflected beams and general idea of the method

Section 0.2.3 provided a bried description of the singularities (caustics) which limit the applicability of semiclassical methods for reconstructing the wave-field in situations often encountered in the theory of electromagnetic waves in a plasma. The focus of this part will be on the special case of cut-off reflections, which is of great interest for plasma physicists: as mentioned in Section 0.2.1, reflectometry is a major diagnostic tool in fusion experiments, as it allows a direct access to the plasma and it makes it possible to deduce important properties (e.g., density, turbulence spectrum) of the plasma itself by comparing the signal of the reflected wave to the injected field. For this reason it is a priority to model properly the mechanism of cut-off reflections from a mathematical and numerical point of view, providing fast and reliable simulations of such phenomena.

On the side of Maxwell's equations the mechanism of cut-off reflections is well understood, and accurate numerical solutions can be computed, paying the price of a high cost in terms of computational resources, for the reasons mentioned in Section 0.2.3. On the other hand, semiclassical analysis has not yet succeeded in providing a solid alternative: beam-tracing methods break in certain situations, while traditional caustic unfolding methods [18, 53] are difficult to apply under realistic conditions, leaving the problem of finding a fast numerical solution for reflected beams open.

II.1.1 Presentation of the problem

Following what announced in Section 0.2.2, in this part a special case of (0.2.1) will be considered as working example. The domain

$$\Omega = \mathbb{R}_+ \times \mathbb{R}^{d-1}$$

is considered, and

$$\Sigma = \{(0, y) \mid y \in \mathbb{R}^{d-1}\}$$

will denote the hypersurface which on the applications side represents an antenna / wave-guide system. With an abuse of notation, $y \in \Sigma$ will be used in what follows, implying of course that $(0, y) \in \Sigma$. The equation considered in this part reads

$$\frac{1}{\kappa^2}\Delta E^\kappa - V E^\kappa = 0, \quad \text{in } \Omega \subseteq \mathbb{R}^d, \tag{II.1.1}$$

where $V \in C^\infty(\mathbb{R}^d)$ and $\kappa \gg 1$. The incident electric field is known on Σ, as discussed in Section 0.2.2, and it is expressed as

$$E^\kappa_{in}(x)|_\Sigma = E^\kappa_0(y), \quad y \in \Sigma. \tag{II.1.2}$$

Again, this condition does not identify a unique solution of (II.1.1), and additional conditions will be given in the next chapters for the specific considered cases.

A bounded solution $E^\kappa : \Omega \to \mathbb{C}$ of (II.1.1) is a scalar wave beam propagating in a medium whose characteristics are described by means of the potential V. One observes that for $V \geq c > 0$, the operator

$$\kappa^{-2}\Delta - V$$

is coercive on $H^1(\Omega)$, which implies that no wave propagation can occur. This suggests the following definition:

Definition II.1 (Cut-off points)**.** *The set of points*

$$\Omega_p := \{x \in \Omega \mid V(x) < 0\}$$

is called propagation region*. Analogously, the* evanescence region *is defined as*

$$\Omega_{ev} := \{x \in \Omega \mid V(x) > 0\}.$$

The set of points separating the two is called cut-off region*, namely,*

$$\Gamma := \{x \in \Omega \mid V(x) = 0\},$$

and its points are called cut-off points.

Cut-off points are of great interest as wave beams get reflected in their vicinity. Most semiclassical methods fail to reconstruct the field near the cut-off region, as discussed more in detail for beam-tracing in what follows.

II.1.2 Limitations of beam-tracing methods

A brief description of wave beams was given in Section 0.2.4, and the features exposed there can be used in order to build efficient numerical schemes that reconstruct a wave beam solution. Beam tracing (BT), or paraxial WKB approximation (pWKB) [61, 62], is among the most used methods for problems of wave propagation in plasma physics. In particular, the code `TORBEAM` [65] is based on the numerical solution of BT equations for electron-cyclotron waves in tokamaks, and it is successfully employed in current-drive calculations in several situations (e.g., [71, 99]). In [86] some reflectometry applications are presented, but the applicability of the method to this class of problems is limited to some particular cases. A qualitative description of these limitations is given in what follows, while a more detailed discussion on the topic can be found in [50]. Similar methods were developed in different branches of mathematical physics as well, and one can refer to [69, 3, 63, 46] and references

therein for an overview.

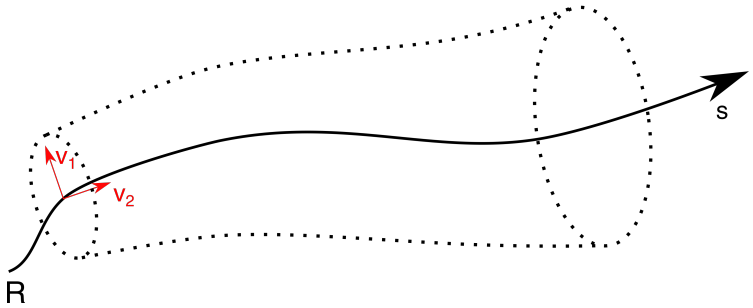

Figure II.1.1: Sketch of the geometrical setup for building the beam tracing solution: a system of coordinates (s, v_1, v_2) is defined locally on the reference ray $R = \{v_1 = v_2 = 0\}$. The beam is localized in a neighborhood of R (dotted lines), and the phase and amplitudes are described by ODEs in the local coordinates.

The main idea of beam tracing is to exploit the fact that wave beams are localized around a certain curve, which is referred to as *reference ray* and is usually identified with the beam axis (see Figure II.1.1 for a sketch). This means that, together with the usual short-wavelength approximation, a scale length is introduced also in the direction transverse to that of propagation. Both conditions are expressed in terms of the large parameter κ, namely,

$$\lambda/L \approx \kappa^{-1} \ll 1, \qquad w/L \approx \kappa^{-1/2} \ll 1,$$

where λ is the wavelength and w denotes the transverse beam width. Considering an ordering in semi-integer powers of the parameter κ amounts then to expanding the beam parameters around the above mentioned central trajectory (from which the name *paraxial* WKB). The result of this procedure is a set of ordinary differential equations describing the beam in terms of the reference ray, a local system of coordinates around it, and the evolution of the phase and amplitudes in this system of coordinates.

As long as the reference ray is smooth, and its length is finite, a coordinate system that covers a beam of width $w = o(\kappa^{-1/2})$ can always be constructed, in the semiclassical limit $\kappa \to \infty$. However, given a finite κ, this might not

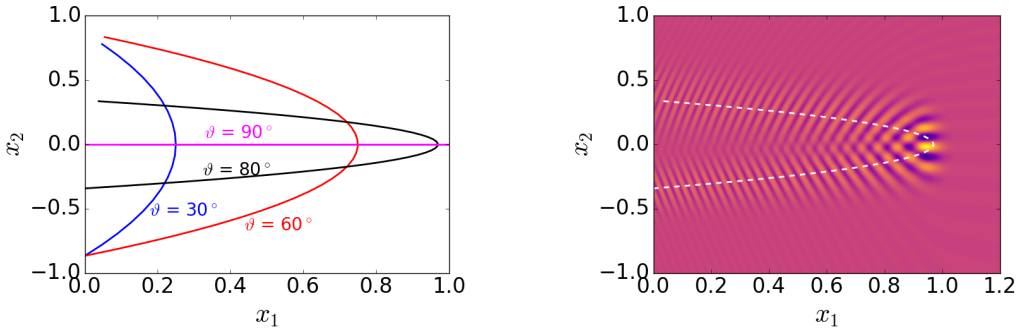

(a) Reference rays corresponding to wave beams launched at $x_1 = 0$ with different injection angles, in presence of a cut-off at $x_1 = 1$. The initial point of the ray is the one with $x_2 < 0$. The curvature radius decreases as the angle increases, until the parabolic trajectory degenerates into two overlapped segments for $\vartheta = 90°$.

(b) Analytic solution for the case of panel (a) with injection angle $\vartheta = 80°$. The incident and reflected branches of the wave beam interfere near the turning point, and in the interference region the beam tracing local coordinates cannot be defined in a sufficiently wide neighborhood of the reference ray (white dashed line).

Figure II.1.2: The plots refer to equation (II.1.1) with $d = 2$ and linear potential $V(x) = x_1 - 1$, which presents a cut-off at $x_1 = 1$.

be possible. The possibility of defining the local coordinates is key in order to build the beam tracing solution, and one could try to express this heuristically in terms of the radius of curvature of the reference ray R_{ray}, namely,

$$w/R_{ray} \approx \kappa^{-1/2} \ll 1,$$

where w denotes again the beam width. In fact beam tracing provides a good approximation of the wave solution in a strip of width w around the reference ray: in case of small R_{ray} the above ordering might break, and regions where the local coordinates are not well defined arise (see Figure II.1.2). In what follows the idea of how to overcome this difficulty is introduced in a heuristic manner, and its formal presentation is contained in the following chapters.

II.1.3 Unfolding the singularity in time

In order to avoid the issues related to the overlapping of the incoming and reflected wave shown in Figure II.1.2, which obstructs the possibility of opportunely defining local coordinates around the reference ray, the idea is to avoid such overlapping by introducing an extra nonphysical dimension to the problem. One can refer to this additional variable as "time", but it must not be confused with physical time. A similar idea for wave propagation problems in plasmas is presented in [73].

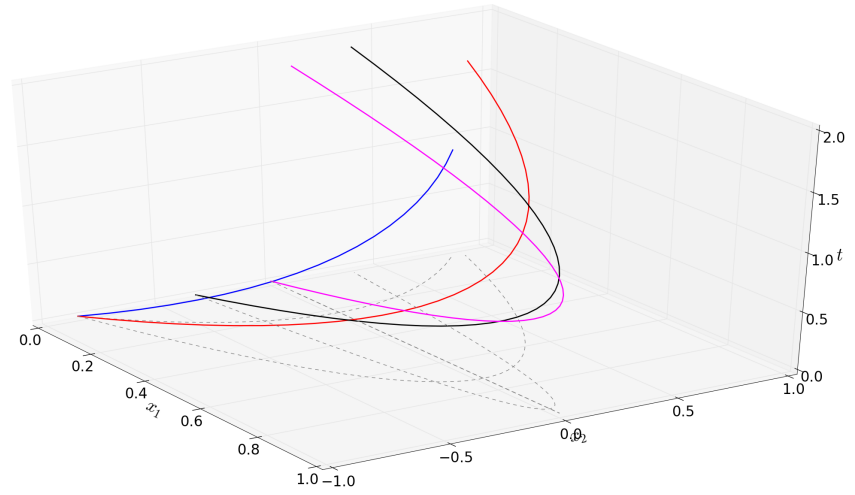

Figure II.1.3: Time-dependent reference rays (cf., Figure II.1.2a).

This procedure leads to the formulation of an evolution problem, to be solved with a method in some way similar to beam tracing, where the solution is opportunely approximated around a curve (again, usually the beam axis). The curve will depend on the newly introduced time variable, so that the critical region is "unwrapped" in the direction of the extra nonphysical dimension, as shown in Figure II.1.3. Specifically, the following initial value problem is considered:

$$\begin{cases} \dfrac{\mathrm{i}}{\kappa}\dfrac{\partial u^\kappa}{\partial t} + \dfrac{1}{\kappa^2}\Delta u^\kappa - V u^\kappa = 0, & t \in \mathbb{R}, \quad x \in \mathbb{R}^d, \qquad \text{(II.1.3a)} \\ u^\kappa(0,x) = u_0^\kappa(x), & x \in \mathbb{R}^d, \qquad \text{(II.1.3b)} \end{cases}$$

where $u_0^\kappa \in L^2(\mathbb{R}^d)$. In general the solution u^κ of this Schrödinger equation is in $C^1(\mathbb{R}, L^2(\mathbb{R}^d))$. The choice of u_0^κ plays a key role here, as it determines the possibility of a successful reconstruction of (II.1.1)-(II.1.2) from that of (II.1.3). In particular, it emerges that u_0^κ should have the following properties:

1. The corresponding solution u^κ is such that $t \mapsto u^\kappa(t,x)$ is in $L^1(\mathbb{R})$ for every $x \in \mathbb{R}^d$. In this way one can define

$$E^\kappa(x) = \int_{-\infty}^{\infty} u^\kappa(t,x)dt, \tag{II.1.4}$$

   and observe that (at least formally) it satisfies Helmholtz equation (II.1.1). This follows by formal integration of (II.1.3a) and commuting the Helmholtz operator with the integral.

2. Being $I \subseteq \mathbb{R}$ an interval such that

$$E^\kappa_{in}(x)|_\Sigma = \int_I u^\kappa(t,x)|_\Sigma dt,$$

   then the correct boundary condition is reconstructed, namely,

$$E^\kappa_0(y) = \int_I u^\kappa(t,x)|_\Sigma dt. \tag{II.1.5}$$

The ideas expressed above can be synthesized in three points which one needs to address in order to reconstruct a solution of the original stationary problem:

- Solve the initial value problem for a given general initial datum.
- Use the general solution to find the right initial condition.
- Integrate in time the solution of the initial value problem for each point in space to reconstruct the desired stationary solution.

For what concerns the first point, the idea is to use the method of Hagedorn wave packets [25, 26] in order to build an approximation of the solution. An

overview of the main features of this method is given in the next chapter, while the possibility of a successful solution of the other two points will be explored in Chapter II.3.

II.2 Hagedorn wave packets

This chapter is dedicated to illustrate the method based on the work of Hagedorn [25, 26] and its further developments [47, 19, 44]. The techniques illustrated here are used in the method proposed in this work to solve problem (II.1.1)-(II.1.2). Hagedorn's method was originally developed to solve problems in quantum mechanics, which are expressed in the form of Schrödinger-type equations like (II.1.3) with initial condition $u_0 \in L^2(\mathbb{R}^d)$ and regular potential $V \in C^\infty(\mathbb{R}^d)$.

II.2.1 Gaussian wave packets

An efficient way of building an approximated solution of (II.1.3) is to look for solutions which depend on a finite number of parameters, whose evolution is then described by an opportunely derived set of equations. One can consider, for example, a Gaussian packet of the form

$$\psi^\kappa(t,x) = a(t)\exp\left[\mathrm{i}\kappa\left(\frac{1}{2}(x-q(t))\cdot\Psi(t)(x-q(t)) + p(t)\cdot(x-q(t)) + S(t)\right)\right], \quad \text{(II.2.1)}$$

where $a(t) > 0$ is the amplitude, $q(t) \in \mathbb{R}^d$ and $p(t) \in \mathbb{R}^d$ represent the position and momentum of the center of mass of the packet respectively, $S(t)$ describes the phase and $\Psi(t) \in \mathbb{C}^{d\times d}$ is a real-symmetric complex matrix with positive definite imaginary part. In the semiclassical limit $\kappa \to \infty$, one can describe

the evolution of the parameters by means of the following set equations,

$$\begin{aligned}
\dot{q} &= 2p, \\
\dot{p} &= -\nabla V(q), \\
\dot{\Psi} &= -2\Psi^2 - D^2V(q), \\
\frac{\dot{a}}{a} &= -\mathrm{tr}\Psi, \\
\dot{S} &= p\dot{q} - p^2 - V(q)
\end{aligned}$$

where the dot denotes the derivative with respect to t and D^2 is the Hessian matrix. With this choice of the parameters the following holds (cf., [47], II.4.4):

Theorem II.1 (cf., [47], II.4.4)**.** *Consider the Gaussian wave packet defined above. If the smallest eigenvalue of $\Im\Psi(t)$ is bounded from below, and if $V \in C^3(\mathbb{R}^d)$ and $\partial^3 V$ is bounded, then*

$$\|\psi^\kappa(t,x) - u^\kappa(t,x)\|_{L^2(\mathbb{R}^d)} \leq c_0 t \kappa^{-1/2},$$

where $u^\kappa(t)$ is an exact solution of (II.1.3) with Gaussian initial data $u^\kappa(0,x) = \psi^\kappa(0,x)$, and c_0 is a constant depending only on the bounds in the assumptions.

This implies in particular that the Gaussian wave packet is an exact solution of Schrödinger equation in the case of a polynomial potential of degree $\nu \leq 2$.

II.2.2 Matrix decomposition and Hagedorn's parametrization

An important step in the development of Hagedorn's work on approximated solutions of problem (II.1.3) is the recognition of the advantages implied by a decomposition of the width matrix Ψ into two complex matrices with certain properties, as stated in the following:

Lemma II.2.1 (Symplectic decomposition, cf., [47], V.1)**.** *Let $Q, P \in \mathbb{C}^{d\times d}$ satisfy the so called* symplecticity *relations*

$$\begin{aligned} Q^tP - P^tQ &= 0, \\ Q^*P - P^*Q &= 2\mathrm{i}I, \end{aligned} \tag{II.2.2}$$

being I the identity matrix. Then, Q and P are invertible and $C = PQ^{-1}$ is complex symmetric with positive definite imaginary part

$$\Im C = (QQ^*)^{-1}.$$

Conversely, every complex symmetric matrix with positive definite imaginary part can be written as $C = PQ^{-1}$, where P and Q satisfy the symplecticity relations (II.2.2).

One refers to (II.2.2) as symplecticity relations as they are equivalent to

$$Y^tJY = J, \quad Y = \begin{pmatrix} \Re Q & \Im Q \\ \Re P & \Im P \end{pmatrix}, \quad J = \begin{pmatrix} 0 & -I \\ I & 0 \end{pmatrix}.$$

Assuming $\Im\Psi$ to have positive definite imaginary part, the matrix Ψ in (II.2.1) admits a symplectic decomposition. This leads to a simpler formulation of the equations describing the parameters of the packet itself. In particular, consider the following normalized d-dimensional Gaussian

$$\begin{aligned} \varphi_0^\kappa[q,p,Q,P](x) = \frac{\kappa^{d/4}}{\sqrt{\pi^{d/2}\det Q}} \exp\Bigg[&\frac{\mathrm{i}\kappa}{2}(x-q)\cdot PQ^{-1}(x-q) \\ &+ \mathrm{i}\kappa p\cdot(x-q)\Bigg], \end{aligned} \tag{II.2.3}$$

where $q, p \in \mathbb{R}^d$, and the matrices $Q, P \in \mathbb{C}^{d\times d}$ satisfy (II.2.2). One can then consider the classical equations of motions associated with problem (II.1.3),

$$\begin{aligned} \dot q &= 2p, \\ \dot p &= -\nabla V(q), \end{aligned} \tag{II.2.4}$$

their linearization around the curve $(q(t), p(t))$,

$$\begin{aligned} \dot{Q} &= 2P, \\ \dot{P} &= -D^2V(q)Q, \end{aligned} \tag{II.2.5}$$

where $D^2V(q)$ is the Hessian matrix, and the classical action

$$S(t) = \int_0^t \left(|p(s)|^2 - V\left(q(s)\right) \right) ds. \tag{II.2.6}$$

Then Theorem II.1 translates into the following result, providing a handy representation of Gaussian wave packets which exploits Hagedorn's matrix decomposition:

Theorem II.2 (cf., [24] or [47], V.1)**.** *Let V be a quadratic potential, and let $(q(t), p(t), Q(t), P(t))$ for $t \in [0, T]$ be a solution of (II.2.4)-(II.2.5) and $S(t)$ as in (II.2.6). If $Q(0)$ and $P(0)$ satisfy the symplecticity relations (II.2.2), then*

1. *$Q(t)$ and $P(t)$ satisfy (II.2.2) for all $t \in [0, T]$;*
2. *The Gaussian wave packet written as*

$$u^\kappa(t, x) = \mathrm{e}^{\mathrm{i}\kappa S(t)} \varphi_0^\kappa[q(t), p(t), Q(t), P(t)](x). \tag{II.2.7}$$

is an exact solution of equation (II.1.3).

Remark II.2.2.1 (Branch of the square root)**.** *The branch of the square root in the factor $\sqrt{\det Q}$ must be selected in such a way that the function $A \mapsto \sqrt{\det A}$ on complex matrices is holomorphic in a neighborhood of the space of real matrices (cf., [30], Section 3.4). This choice implies the continuity of $Q(t)$.*

Notice that (II.2.7) is equivalent to (II.2.1), with $a(t) = \kappa^{d/4}(\pi^d \det Q(t))^{1/2}$ and $\Psi(t) = PQ^{-1}$. The symplectic decomposition though notably simplifies the associated ODEs: the equations for the matrices P and Q are linear, resulting in a significant advantage with respect to the formulation in Section II.2.1,

where the matrix Ψ obeyed a non-linear equation of Riccati type. This result is the starting point of Hagedorn's idea to build a high-order asymptotic solution of problem (II.1.3).

II.2.3 Hagedorn semiclassical wave packets

For quadratic potentials in one dimension the basis of Hermite functions plays an important role in building approximated solutions of wave problems. Such functions can be constructed applying the so called *ladder* (or *raising* and *lowering*) operators to the eigenfunctions of the harmonic oscillator (see for example [47], III.1). The idea of Hagedorn is to generalize this procedure to higher dimensions, building similar operators in the multidimensional case as well, and taking the Gaussian (II.2.3) as starting point.

The multidimensional ladder operators are defined as follows. Given a multi-index $k = (k_1, \ldots, k_d) \in \mathbb{N}_0^d$,

$$\begin{aligned} \mathcal{R} = (\mathcal{R}_j) &= \mathrm{i}\sqrt{\frac{\kappa}{2}}\left(P^*(x-q) - Q^*\left(-\frac{\mathrm{i}}{\kappa}\nabla_x - p\right)\right) \\ \mathcal{L} = (\mathcal{L}_j) &= -\mathrm{i}\sqrt{\frac{\kappa}{2}}\left(P^T(x-q) - Q^T\left(-\frac{\mathrm{i}}{\kappa}\nabla_x - p\right)\right), \end{aligned} \tag{II.2.8}$$

where $\mathcal{R}$ is the raising operator and $\mathcal{L}$ the lowering. The reason behind this terminology is that one can build recursively the so called Hagedorn functions by subsequent application of them. In particular, the k-th Hagedorn function is obtained by the k-fold application of the raising operator to the normalized Gaussian function φ_0^κ,

$$\varphi_k^\kappa = \frac{1}{\sqrt{k!}}(\mathcal{R})^k \varphi_0^\kappa, \quad k \in \mathbb{N}_0^d. \tag{II.2.9}$$

Equivalently, being $\langle j \rangle = (0, \ldots, 1, \ldots, 0)$ the j-th unit vector, the following

recursive relation holds:

$$\varphi^{\kappa}_{k+\langle j\rangle} = \frac{1}{\sqrt{k_j+1}}\mathcal{R}_j\varphi^{\kappa}_k,$$

so that the operator $\mathcal{R}$ "raises" the multi-index k. Conversely, one can "lower" the index through the action of the operator $\mathcal{L}$, which is,

$$\varphi^{\kappa}_{k-\langle j\rangle} = \frac{1}{\sqrt{k_j}}\mathcal{L}_j\varphi^{\kappa}_k. \tag{II.2.10}$$

It is possible to characterize the Hagedorn functions in terms of products of the Gaussian φ^{κ}_0 with a multivariate polynomial of degree $|k|$ (see [44], Proposition 2), and one can verify that in the one-dimensional case they are equivalent to shifted and scaled Hermite functions. Most notably, Hagedorn functions are a powerful tool for building an accurate approximation of solutions of (II.1.3). First of all, a result analogous to Theorem II.1 for a quadratic potential holds:

Theorem II.3 (cf., [47], V.2)**.** *Let V be polynomial of degree $\nu \leq 2$, and let $(q(t), p(t), Q(t), P(t))$ be a solution of (II.2.4)-(II.2.5) and $S(t)$ as in (II.2.6). Then, if $Q(0)$ and $P(0)$ satisfy (II.2.2), the Hagedorn wave packet*

$$\psi^{\kappa}_k(t,x) = \mathrm{e}^{\mathrm{i}\kappa S(t)}\varphi^{\kappa}_k[q(t),p(t),Q(t),P(t)](x) \tag{II.2.11}$$

is a solution of (II.1.3) for every multi-index k.

Moreover, the collection of Hagedorn functions has the following property, which makes it suitable for building approximated solutions in a variety of cases:

Theorem II.4. *The functions $\varphi^{\kappa}_k = \varphi^{\kappa}_k[q,p,Q,P](x)$ form a basis of $L^2(\mathbb{R}^d)$.*

In conclusion an important remark on the case of non-quadratic potentials can be done. In virtue of Theorem II.4, one can represent the solution of

Schrödinger equation (II.1.3) in the basis of Hagedorn functions as a series

$$u^\kappa(t,x) = \mathrm{e}^{\mathrm{i}\kappa S(t)} \sum_{k\in\mathbb{N}_0^d} a_k(t)\varphi_k^\kappa(t,x),$$

where $\varphi_k^\kappa(t,x) = \varphi_k^\kappa[q(t),p(t),Q(t),P(t)](x)$ with parameters satisfying (II.2.4)-(II.2.5), and action integral given by (II.2.6). Assuming a certain regularity of the potential (cf., [26], Theorem 3.6) one can determine a finite number of coefficients $c_k(t)$ such that the truncated series

$$u_{\mathcal{K}}^\kappa(t,x) = \mathrm{e}^{\mathrm{i}\kappa S(t)} \sum_{k\in\mathcal{K}} c_k(t)\varphi_k^\kappa(t,x), \tag{II.2.12}$$

with $\mathcal{K} \subset \mathbb{N}_0^d$ a finite multi-index set, is an approximation of the exact solution of (II.1.3) of asymptotic order $\mathcal{O}(\kappa^{-N/2})$ with arbitrary N (see [26, 47] for possible ways of determining the coefficients c_k).

II.3 Reconstructing wave beams: formulation and numerics

The results recalled in the previous chapter are the basis on which the method presented in this Part is built. The ideas expressed heuristically in Chapter II.1 can be now given a more precise formulation, in virtue of the method of Hagedorn wave packets introduced in the previous chapter.

The discussion in Section II.1.3 shows how the key point of the whole idea is to select the right initial condition for (II.1.3): if the corresponding solution satisfies certain properties, then the possibility to successfully reconstruct a solution of (II.1.1) follows immediately. This leads to the formulation of the following problem:

Problem II.1. *[Selecting the initial condition] Choose the initial condition u_0^κ in (II.1.3b) in such a way that, being u^κ the corresponding solution of (II.1.3a), the function $t \mapsto u^\kappa(t,x)$ is in $L^1(\mathbb{R})$ for every $x \in \Omega$, and the desired boundary value (II.1.2) is reconstructed, which is,*

$$\int_I u^\kappa(t,x)|_\Sigma dt = E_0(y), \quad y \in \Sigma, \tag{II.3.1}$$

where $I \subseteq \mathbb{R}$ is an interval such that integrating u^κ over it the incident field E_{in}^κ is selected at points on Σ.

After this problem is solved, a simple time-integration of u^κ would provide a solution of (II.1.1) satisfying the right boundary condition (II.1.2). No attempt is made to obtain rigorous results in general, but a solid theoretical statement can be done in the case of a two-dimensional Helmholtz equation

with constant or linear potential. For more general potentials the analysis is limited to the Poynting flux of the reconstructed solution and numerical tests (cf., Chapter II.4), for which an asymptotic reference solution can be computed based on the results presented in this chapter. A more complete analysis of the general problem, on both the theoretical and numerical side, will be object of future work.

II.3.1 Helmholtz equation in 2d with constant potential

The simplest case of problem (II.1.1) with $d = 2$ is here considered, namely, that of a constant potential $V(x) = -1$. This corresponds on the physics side to wave beams propagating in free-space, and it can be formulated as the following boundary value problem:

$$\begin{cases} \dfrac{1}{\kappa^2}\Delta E^\kappa(x) + E^\kappa(x) = 0, & x \in \Omega = \mathbb{R}_+ \times \mathbb{R}, \qquad \text{(II.3.2a)} \\ E^\kappa|_\Sigma = E_0^\kappa & \Sigma = \{(0, y) \mid y \in \mathbb{R}\}, \qquad \text{(II.3.2b)} \\ \mathcal{B}_{const} E^\kappa|_\Sigma = 0. & \qquad \text{(II.3.2c)} \end{cases}$$

The boundary datum E_0^κ is assumed to be in $\mathcal{W}_\kappa(\mathbb{R})$), where

$$\mathcal{S} \hookleftarrow \mathcal{W}_\kappa(\mathbb{R}) = \mathcal{F}_\kappa^{-1}\left(C_b^\infty(B_1(0))\right) \qquad \text{(II.3.3)}$$

is the subspace of $\mathcal{S}$ of functions whose semiclassical Fourier transform is smooth and bounded on the unit sphere, equipped with the topology

$$\phi_j \to \phi \text{ in } \mathcal{W}_\kappa(\mathbb{R}) \Leftrightarrow \hat{\phi}_j \to \hat{\phi} \text{ in } C_b^\infty(B_1(0)).$$

Even though this is not the most general setting for problem (II.3.2), it is sufficient in view of the intended applications of this work.

Let $f \in \mathcal{S}(\mathbb{R}^2)$ be a function such that $y \mapsto f(x_1, y)$ is in $\mathcal{W}_\kappa(\mathbb{R})$ for every

$x_1 \in \mathbb{R}_+$, then the action of $\mathcal{B}_{const}$ on f is given by

$$\mathcal{B}_{const} f = \mathcal{F}_\kappa^{-1} \left(\partial_{x_1} f - \mathrm{i}\kappa (1 - N_y^2)^{1/2} f \right), \tag{II.3.4}$$

with $\mathcal{F}_\kappa$ the semiclassical Fourier transform in y and N_y the corresponding conjugate variable. The following holds:

Proposition II.3.1. *Problem (II.3.2) admits a unique solution $E^\kappa \in C_b^\infty(\Omega)$, such that $y \mapsto E^\kappa(x_1, y)$ is in $\mathcal{W}_\kappa(\mathbb{R})$ for every $x_1 \in \mathbb{R}_+$. The solution is*

$$E^\kappa(x_1, y) = \mathcal{F}_\kappa^{-1} \left[\mathrm{e}^{\mathrm{i}\kappa (1 - N_y^2)^{1/2} x_1} \hat{E}_0^\kappa(N_y) \right] \tag{II.3.5}$$

with $\hat{E}_0^\kappa(N_y) = \mathcal{F}_\kappa(E_0^\kappa(y))$.

Proof. If a solution $E^\kappa \in C_b^\infty$ of (II.3.2a) exists, than its spectrum can be written as

$$\hat{E}^\kappa(x_1, N_y) = A_1(N_y) \mathrm{e}^{\mathrm{i}\kappa (1 - N_y^2)^{1/2} x_1} + A_2(N_y) \mathrm{e}^{-\mathrm{i}\kappa (1 - N_y^2)^{1/2} x_1}. \tag{II.3.6}$$

Condition (II.3.2c) implies that $A_2 = 0$, and therefore from (II.3.2b) one can deduce that $A_1(N_y) = \hat{E}_0^\kappa(N_y)$, which defines univocally the solution. □

The formulation given here is consistent with the heuristic one provided in the form of (II.1.2). Looking at (II.3.6) in fact, one can identify the incident field E_{in}^κ as the first term on the right hand side, and the boundary operator $\mathcal{B}_{const}$ ensures that the $E_{in}^\kappa|_\Sigma = E_0^\kappa$.

The associated initial value problem reads

$$\begin{cases} \dfrac{\mathrm{i}}{\kappa} \dfrac{\partial u^\kappa}{\partial t} + \dfrac{1}{\kappa^2} \Delta u^\kappa + u^\kappa = 0, & t \in \mathbb{R}, \qquad \text{(II.3.7a)} \\ u^\kappa(0, x) = u_0^\kappa(x), & x = (x_1, y) \in \mathbb{R}^2, \qquad \text{(II.3.7b)} \end{cases}$$

which admits a unique solution $u^\kappa \in C^1(\mathbb{R}, L^2(\mathbb{R}^2))$ for every $u_0^\kappa \in L^2(\mathbb{R}^2)$. For initial data $u_0^\kappa \in \mathcal{S}$ problem (II.3.7) is also well-posed, and in general the

solution u^κ is such that $u^\kappa(t,\cdot) \in \mathcal{S}(\mathbb{R}^2)$ for every t. The following holds, providing a solution of Problem II.1 for this particular case:

Theorem II.5. *There exists $u_0^\kappa \in \mathcal{S}(\mathbb{R}^2)$ such that, being u^κ the corresponding solution of (II.3.7a),*

1. *For every $x \in \mathbb{R}^2$, $\int u^\kappa(t,x)dt$ is defined in the sense of oscillatory integrals.*

2. *$\int_{-\infty}^{+\infty} u^\kappa(t,x)dt = E^\kappa(x)$ for every $x \in \Omega$, with E^κ the unique solution (II.3.5) of (II.3.2).*

Proof. Consider an initial condition of the form

$$u_0^\kappa(x_1,y) = E_0^\kappa(y)v^\kappa(x_1),$$

where $E_0^\kappa \in \mathcal{W}_\kappa(\mathbb{R})$ is the boundary condition of (II.3.2) and $v^\kappa \in \mathcal{S}(\mathbb{R})$ is such that its Fourier transform satisfies

$$\begin{aligned} &\operatorname{supp}(\hat{v}^\kappa) \Subset \{N_{x_1} > 0\}, \\ &\int_{\mathbb{R}} \hat{v}^\kappa(N_{x_1})dN_{x_1} = 1. \end{aligned} \tag{II.3.8}$$

Its Fourier transform $\widehat{u}_0^\kappa(N_{x_1},N_y)$ is therefore supported in

$$U_0 := \{(N_{x_1},N_y) \mid N_{x_1} > 0,\ N_y^2 \leq 1\}.$$

The Fourier transform with respect to (x_1,y) of the corresponding solution of (II.3.7a) reads

$$\widehat{u}^\kappa(t,N_{x_1},N_y) = \hat{E}_0^\kappa(N_y)\hat{v}^\kappa(N_{x_1})\mathrm{e}^{-\mathrm{i}\kappa(1-|N|^2)t}, \tag{II.3.9}$$

with $N = (N_{x_1},N_y)$. In the sense of oscillatory integrals, one has

$$\int \widehat{u}^\kappa(t,N_{x_1},N_y)dt = \frac{2\pi}{\kappa}\hat{E}_0^\kappa(N_y)\hat{v}^\kappa(N_{x_1})f^*\delta_0, \tag{II.3.10}$$

where $f^*\delta$ is the pull-back of the Dirac delta distribution by the function

$$\begin{aligned} f : U_0 &\longrightarrow \mathbb{R} \\ N &\longmapsto 1 - |N|^2. \end{aligned} \tag{II.3.11}$$

With these definitions, and reminding that N satisfies the dispersion relation $|N|^2 - 1 = 0$, one has (cf., [30], Theorem 6.1.5)

$$f^*\delta_0 = \frac{1}{2N_{x_1}}\delta(N_{x_1} - \sqrt{1 - N_y^2}),$$

where the last expression should be interpreted as a distribution that acts on a test-function φ as

$$\langle f^*\delta_0, \varphi\rangle = \frac{1}{2N_{x_1}} \int_{-1}^{+1} \varphi\left(\sqrt{1 - N_y^2}, N_y\right) dN_y.$$

Therefore, one can write the integral of (II.3.9) as

$$\int \widehat{u}^\kappa(t, N_{x_1}, N_y) = \frac{\pi}{\kappa N_{x_1}} \hat{E}_0^\kappa(N_y)\delta(N_{x_1} - \sqrt{1 - N_y^2}).$$

To conclude the proof it is sufficient to use an analogous argument to compute the Fourier transform $\widehat{E}^\kappa(N_{x_1}, N_y)$ of the unique solution of (II.3.2) found in Proposition (II.3.1), which returns the same quantity as the right hand side of this last equation. □

The following observations link the results above to the idea of building a method based on the theory of Hagedorn wave packets:

1. The initial condition u_0^κ satisfying the requirements of Proposition II.5 is in $\mathcal{S}(\mathbb{R}^2)$, so that it can be decomposed in the $L^2(\mathbb{R}^2)$-basis of Hagedorn functions.

2. The numerical tests in the next Chapter follow this idea in order to reconstruct Gaussian boundary data: the initial condition for Schrödinger equation is taken in the form of the fundamental Hagedorn function (II.2.3)

with diagonal matrices P and Q such that the part in y coincides with E_0^κ and the function v_1^κ is also Gaussian, with parameters chosen in order to satisfy (II.3.8).

II.3.2 Helmholtz equation in 2d with linear potential

In this section a cut-off point is introduced in the equation, and a potential $V(x) = x_1 - 1$ and $d = 2$ is considered, for which one can formulate the following boundary value problem:

$$\begin{cases} \dfrac{1}{\kappa^2}\Delta E^\kappa(x) - (x_1 - 1)E^\kappa(x) = 0, & x \in \Omega = \mathbb{R}_+ \times \mathbb{R}, \quad \text{(II.3.12a)} \\ E^\kappa|_\Sigma = \mathcal{B}_{lin} E_0^\kappa, & \Sigma = \{(0, y) \mid y \in \mathbb{R}\}. \quad \text{(II.3.12b)} \end{cases}$$

The boundary datum E_0^κ is assumed to be in $\mathcal{W}_\kappa(\mathbb{R}))$ (cf., (II.3.3), and the boundary operator $\mathcal{B}_{lin}$ acts on a function $f \in \mathcal{W}_\kappa(\mathbb{R})$ as

$$\mathcal{B}_{lin} f = \mathcal{F}_\kappa^{-1}\left(\mathrm{Ai}(-\kappa^{2/3}(1 - N_y^2))g^\kappa(N_y)\hat{f}(N_y)\right) \tag{II.3.13}$$

where $\hat{f}(N_y) = \mathcal{F}_\kappa(f(y))$, and

$$g^\kappa(N_y) = 2\sqrt{\pi}\kappa^{1/6}(1 - N_y^2)^{1/4}\mathrm{e}^{\mathrm{i}\frac{2}{3}(1-N_y^2)^{3/2} - \mathrm{i}\frac{\pi}{4}}. \tag{II.3.14}$$

The following holds:

Proposition II.3.2. *Problem (II.3.12) admits a unique solution $E^\kappa \in C_b^\infty(\Omega)$, such that $y \mapsto E^\kappa(x_1, y)$ is in $\mathcal{W}_\kappa$ for every $x_1 \in \Omega$. The solution can be expressed as*

$$E^\kappa(x) = \mathcal{F}_\kappa^{-1}\left(c(N_y)\mathrm{Ai}(-\varphi(x_1, N_y))\right) \tag{II.3.15}$$

where Ai *is the Airy function,*

$$\varphi(x_1, N_y) = \kappa^{2/3}(1 - x_1 - N_y^2), \tag{II.3.16}$$

and

$$c(N_y) = g^\kappa \hat{E}_0^\kappa(N_y), \tag{II.3.17}$$

with g^κ given by (II.3.14).

Proof. In general bounded solutions of (II.3.12a) satisfy (II.3.15)-(II.3.16) (cf., [30], 7.6), and it is immediate to verify that condition (II.3.12b) implies (II.3.17). □

Notice that the boundary operator (II.3.13) is consistent with the more heuristic formulation given in Chapter II.1, in the form (II.1.2). To this purpose a stationary phase argument can be used, to approximate the Airy function in the limit $\varphi \to \infty$ as

$$\mathrm{Ai}(-\varphi) \sim \frac{1}{2\sqrt{\pi}}\varphi^{-1/4}\left(\mathrm{e}^{-\mathrm{i}\frac{2}{3}\varphi^{3/2}+\mathrm{i}\frac{\pi}{4}} + \mathrm{e}^{\mathrm{i}\frac{2}{3}\varphi^{3/2}-\mathrm{i}\frac{\pi}{4}}\right). \tag{II.3.18}$$

One can identify incident and reflected branches of the wave field, which correspond to the first and second exponential on the right hand side, respectively, so that

$$\hat{E}_{in}^\kappa(x_1, N_y) = c(N_y)\frac{1}{2\sqrt{\pi}}\varphi^{-1/4}\mathrm{e}^{-\mathrm{i}\frac{2}{3}\varphi^{3/2}+\mathrm{i}\frac{\pi}{4}}. \tag{II.3.19}$$

Substituting $c(N_y)$ as given in (II.3.17) and evaluating $\hat{E}_{in}^\kappa$ on Σ one obtains, after inverse Fourier transform, $E_{in}^\kappa(0, y) = E_0^\kappa(y)$.

The associated Schrödinger equation takes the form

$$\begin{cases} \dfrac{\mathrm{i}}{\kappa}\dfrac{\partial u^\kappa}{\partial t} + \dfrac{1}{\kappa^2}\Delta u^\kappa - (x_1 - 1)u^\kappa = 0, & t \in \mathbb{R}, \quad \text{(II.3.20a)} \\ u^\kappa(0, x) = u_0^\kappa(x), & x = (x_1, y) \in \mathbb{R}^2, \quad \text{(II.3.20b)} \end{cases}$$

and the rest of this section is dedicated to prove the analogous to Proposition II.5 for this case:

Theorem II.6. *Given $u_0^\kappa \in \mathcal{S}(\mathbb{R}^2)$, being u^κ the corresponding solution of (II.3.20a), the map $t \mapsto u^\kappa(t, x)$ is in $L^1(\mathbb{R})$ for every $x \in \mathbb{R}^2$. Moreover, there exists u_0^κ such that time integration of u^κ reconstructs the unique solution (II.3.15)-(II.3.17), i.e., $\int_{-\infty}^{+\infty} u^\kappa(t, x)dt = E^\kappa(x)$ for every $x \in \Omega$.*

The proof here will be divided into two three steps, due to the lengthy calculation: first of all the solution of (II.3.20) for a general initial condition $u_0^\kappa \in \mathcal{S}(\mathbb{R}^2)$ will be computed, followed by the computation of the reconstructed beam. The existence of the desired u_0^κ will follow by comparison with the exact solution of (II.3.12).

Solution of the initial value problem

After Fourier transform with respect to both spatial variables of equation (II.3.20a) one gets

$$\frac{\mathrm{i}}{\kappa}\left(\frac{\partial}{\partial t} - \frac{\partial}{\partial N_{x_1}}\right)\widehat{u}^\kappa(t, N_{x_1}, N_y) + (1 - N_{x_1}^2 - N_y^2)\widehat{u}^\kappa(t, N_{x_1}, N_y) = 0, \quad \text{(II.3.21)}$$

where the double hat denotes the Fourier transform with respect to (x_1, y) and (N_{x_1}, N_y) are the corresponding conjugate variables. A solution can be found by means of the method of characteristics, which in this case can be integrated analytically:

$$\begin{cases} \dfrac{dN_{x_1}}{dt} = -1 \\ \dfrac{dN_y}{dt} = 0, \end{cases} \Longrightarrow \begin{cases} N_{x_1}(t) = N_{x_1,0} - t \\ N_y(t) = N_{y,0}, \end{cases} \quad \text{(II.3.22)}$$

being $N_{x_1,0}$ and $N_{y,0}$ the starting points. The total time derivative of $\widehat{u}^\kappa$ will then satisfy

$$\begin{aligned} \frac{d}{dt}\widehat{u}^\kappa\left(t, N_{x_1}(t), N_y(t)\right) &= \frac{\partial \widehat{u}^\kappa}{\partial t} - \frac{\partial \widehat{u}^\kappa}{\partial N_{x_1}} \\ &= \mathrm{i}\kappa\left(1 - N_{x_1}(t)^2 - N_y(t)^2\right)\widehat{u}^\kappa\left(t, N_{x_1}(t), N_y(t)\right), \end{aligned}$$

which can be solved analytically, giving

$$\begin{aligned} \widehat{u}^\kappa(t, N_{x_1}(t), N_y(t)) &= \widehat{u}_0^\kappa(N_{x_1,0}, N_{y,0}) \exp\left(\int_0^t 1 - N_{x_1}(s)^2 - N_y(s)^2 ds\right) \\ &= \widehat{u}_0^\kappa(N_{x_1,0}, N_{y,0}) \exp\left(\mathrm{i}\kappa(1 - N_{y,0}^2)t - \mathrm{i}\kappa(N_{x_1,0}^2 t - t^2 N_{y,0}) - \mathrm{i}\kappa\frac{t^3}{3}\right). \end{aligned}$$

After substitution of (II.3.22) one finally gets

$$\begin{aligned}\widehat{u}^\kappa(t, N_{x_1}, N_y) &= \widehat{u}_0^\kappa(N_{x_1} + t, N_y) \\ &\quad \times \exp\left(\mathrm{i}\kappa(1 - N_y^2)t - \mathrm{i}\kappa(N_{x_1}^2 t + t^2 N_{x_1}) - \mathrm{i}\kappa\frac{t^3}{3}\right).\end{aligned} \tag{II.3.23}$$

For each fixed (N_{x_1}, N_y) the above expression is a function of t which is in $L^1(\mathbb{R})$, as follows from the fact that both u_0^κ and the exponential multiplying it are in $\mathcal{S}$, which proves the first statement in Proposition II.6.

Reconstructed wave beam

The time integral of (II.3.23) can be computed, in order to obtain a "reconstructed wave beam", which can be then compared to equation (II.3.15). One gets

$$\begin{aligned}\int_{-\infty}^{+\infty} &\widehat{u}^\kappa(t,N_{x_1}, N_y)dt \\ &= \int_{-\infty}^{+\infty} \widehat{u}_0^\kappa(s, Ny) \exp\left(\mathrm{i}\kappa(1 - N_y^2)(s - N_{x_1}) - \mathrm{i}\kappa\frac{s^3 - N_{x_1}^3}{3}\right) ds \\ &= C(N_y) \exp\left(-\mathrm{i}\kappa(1 - N_y^2)N_{x_1} + \mathrm{i}\kappa\frac{N_{x_1}^3}{3}\right),\end{aligned} \tag{II.3.24}$$

where $s = N_{x_1} + t$ and

$$C(N_y) = \int_{-\infty}^{+\infty} \widehat{u}_0^\kappa(s, N_y) \exp\left(\mathrm{i}\kappa(1 - N_y^2)s - \mathrm{i}\kappa\frac{s^3}{3}\right) ds. \tag{II.3.25}$$

Proof of Theorem II.6. The time integrability of the solution of (II.3.20a) was already shown above, so that the second part of the statement is left. The Fourier transform with respect to (x_1, y) of (II.3.15 yields

$$\widehat{E}^\kappa(N_{x_1}, N_y) = c(N_y) \exp\left(-\mathrm{i}\kappa(1 - N_y^2)N_{x_1} + \mathrm{i}\kappa\frac{N_{x_1}^3}{3}\right), \tag{II.3.26}$$

where $c(N_y)$ is given by (II.3.17). A comparison with (II.3.24) shows that

an exact matching between the reconstructed solution and the exact one is obtained if $C(N_y) = c(N_y)$, that is

$$\int_{-\infty}^{+\infty} \widehat{u}_0^\kappa(s, N_y) \exp\left(\mathrm{i}\kappa(1 - N_y^2) - \mathrm{i}\kappa\frac{s^3}{3}\right) ds = c(N_y), \tag{II.3.27}$$

so that the problem of the existence of u_0^κ as in the statement is reduced to the possibility to invert the expression in (II.3.27). But of course the map

$$\begin{aligned} \mathcal{S}(\mathbb{R}^2) &\longrightarrow \mathcal{W}_\kappa(\mathbb{R}), \\ g(\sigma, \eta) &\longmapsto f(\eta) = \int_{\mathbb{R}} g(\sigma, \eta) d\sigma \end{aligned}$$

is surjective, as for every $f \in \mathcal{W}_\kappa(\mathbb{R})$ one can take $g(\sigma, \eta) = f(\eta)h(\sigma)$, where $h \in \mathcal{S}(\mathbb{R})$ has unit integral. □

Some observations can be made here also, in relation to the idea of having u_0^κ in the form of (superposition of) Hagedorn wave packets.

1. The initial condition u_0^κ found in Proposition II.6 is in $\mathcal{S}(\mathbb{R}^2)$, so that it can be decomposed in the $L^2(\mathbb{R}^2)$-basis of Hagedorn functions.

2. If one looks for an initial condition u_0^κ of the form

   $$u_0^\kappa(x_1, y) = v_1^\kappa(x_1) v_2^\kappa(y),$$

   equation (II.3.27) can be written as

   $$\int_{-\infty}^{+\infty} \hat{v}_1^\kappa(s) \exp\left(\mathrm{i}\kappa(1 - N_y^2) - \mathrm{i}\kappa\frac{s^3}{3}\right) ds \hat{v}_2^\kappa(N_y) = c(N_y).$$

   The right hand side contains a factor $\hat{E}_0^\kappa(N_y)$, so that the choice

   $$v_2^\kappa(y) = E_0^\kappa(y)$$

   reduces the problem to that of finding v_1^κ only, which is possible according to the same argument used in the proof of Proposition (II.6).

3. For what concerns the numerical tests in the next Chapter, Gaussian boundary data will be considered. The initial condition for Schrödinger equation is taken in the form of the fundamental Hagedorn function (II.2.3) with diagonal matrices P and Q such that the argument of point 2 applies, and the function v_1^κ is also taken Gaussian, with suitable parameters in order to satisfy (II.3.27) with a certain accuracy.

The initial data u_0^κ identified in Proposition II.6 also satisfies the requirements as formulated in Problem II.1. This will be shown heuristically, looking at the profile of the wave packet $u^\kappa(t, x)$ as a function of time, evaluated at a point $x_* = (0, y) \in \Sigma$. One can distinguish two passages of the wave packet

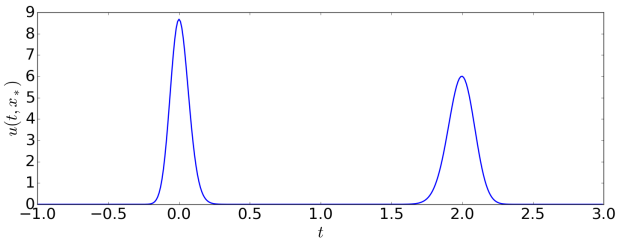

Figure II.3.1: Wave packet $u^\kappa(t, x_*)$, with $x_* = (0, 0)$, corresponding to a solution of (II.1.3) with initial condition u_0^κ given by (II.2.3), originating at x_* and propagating towards the r.h.s. orthogonal to $\Sigma = \{(0, y) \mid y \in \mathbb{R}\}$.

through the point x_*, corresponding in chronological order to the incident and reflected contribution to the wave field. Integrating the wave packet over an interval $I \subseteq \mathbb{R}$ which accounts for the first passage only, will return the incident field E_{in}^κ whose spectrum is defined in (II.3.19).

II.3.3 Description of the algorithm

In the previous sections problem (II.1.1) was formulated with more precision in some particular cases. Moreover for linear and constant potentials rigorous results were presented concerning the general idea of reconstructing wave beams with wave packets in presence of a cut-off point. These results though

are not very handy on the practical side, as in particular they only provide a proof of existence of a solution of (II.1).

Going back to the general idea of using Hagedorn wave packets, three main steps can be identified to reconstruct wave beams:

- Choose of the initial condition for the initial value problem.
- Solve of the ODEs describing the evolution of the parameters which define Hagedorn packets.
- Integrate the wave packet solution in time for all points in the spatial domain.

These are the building blocks of the numerical scheme presented here and used for the numerical tests in the next chapter.

Choice of the initial condition

This is the main point of the whole method, as emerges already from the formulation of Problem II.1, for which in general an analytic solution cannot be found explicitly. A more practical way of choosing the initial condition u_0^κ of (II.1.1) is described here. In particular this is based on the choice of u_0^κ that admits a separation of variables, so that the factor depending on y can be taken equal to the boundary condition E_0^κ in (II.1.2). The part in x_1 will be partially determined by the boundary conditions as well, in order to select the right direction of propagation (cf., sections II.3.1 and II.3.2). Nevertheless, it will also depend on some free parameters $(a_1, \dots, a_n)$, so that one can write

$$u_0[a_1, \dots, a_n](x) = v[a_1, \dots, a_n](x_1)E_0(y), \tag{II.3.28}$$

At this point one can reformulate Problem II.1 as an optimization problem, in the following way:

Problem II.2 (Optimal initial condition)**.** *Find parameters* $a_1, \dots, a_n \in \mathbb{R}$ *that minimize the functional*

$$F(a_1, \dots, a_n) := \left\| \int_{\mathbb{R}} u[a_1, \dots, a_n](t, x) dt \big|_{\Sigma} - E_0(y) \right\|_{L^2(\mathbb{R}^{d-1})}, \qquad \text{(II.3.29)}$$

where $u[a_1, \dots, a_n](t, x)$ *is the solution of Schrödinger equation with initial condition (II.3.28).*

For example, in the case of a Gaussian boundary condition E_0, it is reasonable to build the initial condition u_0 by assuming it to be Gaussian in the x_1 direction as well, depending on parameters like amplitude, width and radius of curvature. More details will be provided in the next chapter, when presenting the numerical experiments.

This procedure produces an optimal initial condition, such that the error of the correspondent stationary solution at the boundary is minimal. Such an error still exists though, and and its propagation in the whole spatial domain is a point one has to be careful about.

Solution of the ODEs

The solution of Schrödinger equation is found via the method of Hagedorn wave packets. In general, using the expansion in the Hagedorn basis, one can identify parameters (q, p, Q, P) such that

$$u_0(x) \approx \sum_{k \in \mathcal{K}} c_k \varphi_k^{\kappa}[q, p, Q, P](x),$$

for some finite set of multi-indexes $\mathcal{K}$. For the case of Gaussian beams, which covers a large set of interesting applications, this reduces to

$$u_0(x) \propto \varphi_0^{\kappa}[q, p, Q, P](x).$$

The corresponding solution of (II.1.3) will be then given by evolving the parameters (q, p, Q, P) according to

$$\dot{q} = 2p, \qquad \dot{p} = -\nabla V(q), \tag{II.3.30a}$$

$$\dot{Q} = 2P, \qquad \dot{P} = -D^2V(q)Q, \tag{II.3.30b}$$

and by multiplication by a factor $\exp(\mathrm{i}\kappa S(t))$, where

$$S(t) = \int_0^t \left(|p(s)|^2 - V\left(q(s)\right)\right) ds. \tag{II.3.31}$$

In some of the cases treated in this work (i.e., constant and linear potentials) the ODEs can be solved analytically.

Time integration

Once the wave packet solution of (II.1.3) is found, one needs to compute

$$\int_{-\infty}^{+\infty} u^\kappa(t, x) dt$$

for every $x \in \Omega$ in order to reconstruct the stationary solution of (II.1.1). Notice that at each point in space the solution is computed independently. This is a useful feature of this method, as in many applications one is interested in the field in a limited subset of the whole physical domain.

More details on the actual implementation of the numerical scheme will be given in the next chapter.

II.3.4 Conservation of the Poynting flux and error propagation

A quantity of interest from both the physical and mathematical point of view is the beam energy flux through a certain surface (Poynting flux). For prob-

lem (II.1.1), considering the surface $\{x_1 = x_1^*\}$, such quantity is given by

$$\mathcal{P}_{E^\kappa}(x_1^*) := \frac{1}{\kappa}\int_{-\infty}^{+\infty} \Im\left(\bar{E}^\kappa \partial_{x_1} E^\kappa\right)|_{x_1=x^*}\, dy. \tag{II.3.32}$$

The following classical result holds:

Theorem II.7. *Let E^κ be a $C^2(\Omega)$ solution of Helmholtz equation (II.1.1) satisfying $E^\kappa(x_1,\cdot) \in \mathcal{S}(\mathbb{R})$. Then the Poynting flux (II.3.32) is constant.*

Proof. The field E^κ satisfies

$$\begin{aligned} \frac{1}{2\mathrm{i}\kappa}\bar{E}^\kappa \Delta E^\kappa + \frac{\mathrm{i}\kappa}{2} V|E^\kappa|^2 = 0, \\ -\frac{1}{2\mathrm{i}\kappa} E^\kappa \Delta \bar{E}^\kappa - \frac{\mathrm{i}\kappa}{2} V|E^\kappa|^2 = 0. \end{aligned} \tag{II.3.33}$$

Summing the two, and using the identity,

$$\bar{E}^\kappa \Delta E^\kappa - E\Delta\bar{E}^\kappa = 2\mathrm{i}\nabla\cdot\left(\Im\bar{E}^\kappa \nabla E^\kappa\right), \tag{II.3.34}$$

one gets

$$\nabla\cdot\left(\frac{1}{\kappa}\Im\bar{E}^\kappa\nabla E^\kappa\right) = 0.$$

Integration with respect to y leads to

$$\partial_{x_1}\mathcal{P}_{E^\kappa}(x_1) = 0,$$

which concludes the proof. □

It is therefore reasonable to check whether the proposed method of Hagedorn wave-packets provides a solution of (II.1.1) that retains this property. The following holds:

Proposition II.3.3. *Let $u^\kappa = u^\kappa(t,x) = \psi_0^\kappa(t,x)$ be the Hagedorn wave-packet as given in (II.2.11), with $(q(t),p(t),Q(t),N(t))$ solution of (II.3.30a)-(II.3.30b)*

and $S(t)$ given by (II.3.31). Then u satisfies

$$\frac{\mathrm{i}}{\kappa}\frac{\partial u^\kappa}{\partial t}(t,x)+\frac{1}{\kappa^2}\Delta u^\kappa(t,x)-V_{mod}(t,x)u^\kappa(t,x)=0, \tag{II.3.35}$$

where the modified potential has the form

$$\begin{aligned} V_{mod}(t,x)=V(q(t))+\nabla V(q(t))\cdot(x-q(t))+\\ \frac{1}{2}(x-q(t))\cdot D^2V(q(t))(x-q(t)). \end{aligned} \tag{II.3.36}$$

Proof. Denoting by $a(t)$ the amplitude factor in (II.2.11), which is

$$a(t)=\sqrt{\frac{\kappa}{\pi}}(\det Q(t))^{-1/2},$$

and $\Psi=PQ^{-1}$, one has

$$\Delta u^\kappa=\left(-\kappa^2p^2-2\kappa^2p\cdot\Psi(x-q)-\kappa^2(x-q)\cdot\Psi^2(x-q)+\mathrm{i}\kappa\mathrm{tr}\Psi\right)u^\kappa, \tag{II.3.37}$$

where $\mathrm{tr}\Psi$ is the trace of the matrix Ψ, and

$$\begin{aligned} \frac{\partial u^\kappa}{\partial t}=\Bigg(\frac{\dot a}{a}+\mathrm{i}\kappa\left(\dot S+\dot p\cdot(x-q)-p\cdot\dot q\right)\\ +\frac{\mathrm{i}\kappa}{2}(x-q)\cdot\dot\Psi(x-q)-\mathrm{i}\kappa\dot q\cdot A(x-q)\Bigg)u^\kappa. \end{aligned} \tag{II.3.38}$$

In the above expressions the time dependence of the parameters q,p,Q,P and S is implied, and the dot indicates the derivative with respect to t. It follows that

$$\begin{aligned} \frac{\mathrm{i}}{\kappa}\frac{\partial u^\kappa}{\partial t}+\frac{1}{\kappa^2}\Delta u^\kappa=\Bigg\{&\frac{\mathrm{i}}{\kappa}\frac{\dot a}{a}+\frac{\mathrm{i}}{\kappa}\mathrm{tr}\Psi\\ &-(\dot S-p\cdot\dot q+p^2)\\ &-(\dot p-\dot q\Psi+2p\Psi)\cdot(x-q)\\ &-(x-q)\cdot(\Psi^2+\frac{1}{2}\dot\Psi)(x-q)\Bigg\}u^\kappa. \end{aligned}$$

Using the formula

$$\frac{d}{dt}\det Q = \det Q \mathrm{tr}(Q^{-1}\dot{Q}),$$

together with the equations for the parameters (q, p, Q, P) and S given in (II.2.4)-(II.2.6), one gets

$$\begin{aligned}
\frac{\dot{a}}{a} &= -\mathrm{tr}\Psi, \\
\dot{S} - p\cdot\dot{q} + p^2 &= -V(q), \\
\dot{p} - \dot{q}\Psi + 2p\Psi &= -\nabla V(q), \\
\frac{1}{2}\dot{\Psi} + \Psi^2 &= -\frac{1}{2}D^2V(q),
\end{aligned}$$

from which it follows that

$$\frac{\mathrm{i}}{\kappa}\frac{\partial u^\kappa}{\partial t} + \frac{1}{\kappa^2}\Delta u^\kappa = V_{mod}u^\kappa,$$

and the proof is concluded. □

In the case of a quadratic potential V equation (II.3.35) reduces to the standard Schrödinger equation (II.1.3a), coherently with Theorem II.3. For the general case, the Hagedorn wave-packet also satisfies a Schrödinger-type equation, with a time-dependent potential which is the quadratic approximation of V in the neighborhood of the trajectory $q(t)$. This result comes to hand for the derivation of the following result on the Poynting flux for the Hagedorn solution of Helmholtz equation:

Proposition II.3.4. *Let $\tilde{E}^\kappa$ be the field reconstructed from the Hagedorn packet $u^\kappa(t,x) = \psi_0^\kappa(t,x)$, that is,*

$$\tilde{E}^\kappa(x) = \int_{-\infty}^{+\infty} u(t,x)dx.$$

Then the Poynting flux of $\tilde{E}^\kappa$ as defined in (II.3.32) satisfies

$$\frac{\partial \mathcal{P}_{E^\kappa}}{\partial x_1} = -\frac{\mathrm{i}\kappa}{2}\int_{-\infty}^{+\infty}\left(\int_{-\infty}^{+\infty}(V_{mod}-V)\left(\bar{\tilde{E}}^\kappa u^\kappa - \tilde{E}^\kappa\bar{u}^\kappa\right)\,dt\right)\,dy. \qquad \text{(II.3.39)}$$

Proof. From Proposition II.3.3 it follows that

$$\frac{1}{\kappa^2}\Delta\tilde{E}^\kappa - \int_{-\infty}^{+\infty} V_{mod}u^\kappa \, dt = 0.$$

By simple algebraic passages, and multiplying by $(-\mathrm{i}\kappa)\bar{\tilde{E}}^\kappa$, one obtains

$$\frac{1}{\mathrm{i}\kappa}\bar{\tilde{E}}^\kappa\Delta\tilde{E}^\kappa - \mathrm{i}\kappa V|\tilde{E}^\kappa|^2 + \mathrm{i}\kappa\bar{\tilde{E}}^\kappa\int_{-\infty}^{+\infty}(V_{mod}-V)u^\kappa \, dt = 0.$$

By summing the above expression to its complex conjugate, and using the identity (II.3.34), equation (II.3.39) follows immediately by integrating with respect to y all the resulting terms. □

Remark II.3.4.1. *The right hand side of (II.3.39) can actually be estimated, using the fact that, being u^κ in the form of the Hagedorn packet ψ_0^κ,*

$$|(V_{mod}-V)u^\kappa| \leq c_0\kappa^{-3/2}.$$

As a consequence, the x_1-derivative of the Poynting flux is $\mathcal{O}(\kappa^{-1/2})$.

The above result is also consistent with the results on Hagedorn packets in the case of a quadratic potential:

Corollary 2. *If the potential V is quadratic, then the Poynting flux of the field reconstructed with the method of Hagedorn wave-packets is constant.*

Proof. This follows immediately observing that the modified potential V_{mod} defined in (II.3.36) is the second order truncation of the Taylor expansion of V around the trajectory $q(t)$. □

It is therefore possible to quantify exactly the variation of the Poynting flux the x_1-axis for the wave field reconstructed using the fundamental Hagedorn packet ψ_0^κ. This is constant equal to zero only in the case of quadratic potentials, and traces some limits of applicability of the method of Hagedorn wave-packets, in the sense that one cannot expect it to provide a satisfactory

solution (namely, whose flux is conserved) if the difference between the potential and its quadratic approximation is too large. Notice that this can be hopefully improved by including higher order wave packets in the approximation of the solution of Schrödinger equation. Proposition II.3.4 also provides a solid test for the numerical experiments that will be presented in the next chapter, where the scheme introduced below is implemented. In particular, for the case of quadratic potentials conservation of the Poynting flux is expected, while the identity in (II.3.39) can be used to understand the behaviour of the Hagedorn solution for the non-quadratic cases.

II.3.5 Asymptotic solution for smooth increasing potentials

In this section Problem (II.1.1) is formulated for a class of potentials which are close to the typical profiles that one finds in the intended applications framework. In particular, V is chosen in the form $V(x) = a(x_1) - 1$, with $a \in C^\infty(\mathbb{R})$ such that

$$\begin{aligned} &a'(x_1) > 0, \\ &\lim_{x_1 \to -\infty} a(x_1) = 0, \\ &\lim_{x_1 \to +\infty} a(x_1) = a_\infty > 1. \end{aligned} \tag{II.3.40}$$

This class of potentials produces a cut-off for Helmholtz equation at points which are solutions of the algebraic problem $a(x_1) = 1$. The properties of a listed in (II.3.40) imply that there is a unique cut-off point in $\mathbb{R}_+$. The notation

$$a_{N_y} = 1 - N_y^2$$

will be used in what follows, together with the concept of *turning point* x_{N_y}, which is defined as the solution of the non-linear algebraic problem

$$a(x_1) = a_{N_y}.$$

Notice that if $N_y = 0$ the turning point coincides exactly with the cut-off point.

The following boundary value problem is considered:

$$\begin{cases} \dfrac{1}{\kappa^2}\Delta E^\kappa(x) - (a(x_1)-1)E^\kappa(x) = 0, & x \in \Omega = \mathbb{R}_+ \times \mathbb{R}, \quad \text{(II.3.41a)} \\ E^\kappa|_\Sigma = \mathcal{B}_{gen} E_0^\kappa & \Sigma = \{(0,y) \mid y \in \mathbb{R}\}, \quad \text{(II.3.41b)} \end{cases}$$

with boundary datum $E_0^\kappa \in \mathcal{W}_\kappa(R))$ (cf., (II.3.3)). The boundary operator $\mathcal{B}_{gen}$ acts on a function $f \in \mathcal{W}_\kappa(\mathbb{R})$ as

$$\mathcal{B}_{gen} f = \mathcal{F}_\kappa^{-1}\left(\mathrm{Ai}\left(\frac{3\kappa}{2}\sigma_0\right) g^\kappa(N_y)\hat{f}(N_y)\right) \tag{II.3.42}$$

with the multiplier g^κ defined as

$$g^\kappa(N_y) = 2\sqrt{\pi}\left(\frac{3\kappa}{2}\sigma_0\right)^{1/6} \mathrm{e}^{\mathrm{i}\kappa\sigma_0 - \mathrm{i}\frac{\pi}{4}}, \tag{II.3.43}$$

where the notation

$$\sigma_0 = \int_0^{x_{N_y}} (a_{N_y} - a(x_1))^{1/2} dx_1$$

is introduced.

No attempt is made here to make rigorous statements on the well-posedness of (II.3.41), and one may refer to the classical textbook of Wasow [100] for similar problems. The analytic part for this class of problems is restricted to the following asymptotic result:

Proposition II.3.5. *Let V be a potential of the form $V(x) = a(x_1) - 1$, where a satisfies (II.3.40). Then, for every κ and N_y there exists a real-valued function $\varphi = \varphi(x_1, N_y)$ such that, for every $c \in \mathcal{S}$,*

$$E^\kappa(x) = \mathcal{F}_{N_y \mapsto y}^{-1}\left(c(N_y)\mathrm{Ai}(-\varphi(x_1, N_y))\right), \tag{II.3.44}$$

satisfies

$$\frac{1}{\kappa^2}\Delta E^\kappa - (a(x_1)-1)E^\kappa = \mathcal{O}(\kappa^{-4/3}) \tag{II.3.45}$$

in the semiclassical limit $\kappa \to \infty$. Moreover, the choice

$$c(N_y) = g^{\kappa}(N_y)\hat{E}_0^{\kappa}(N_y) \tag{II.3.46}$$

implies that (II.3.44) satisfies the boundary condition (II.3.41b).

A brief discussion on the reminder follows the numerical tests for which this asymptotic solution is used as a reference solution (cf., II.4.6.1). The following result will be used for the proof of the main proposition:

Lemma II.3.1. *Let $a = a(x_1)$ satisfy (II.3.40). Consider the equation*

$$\rho'(x_1)^2\rho(x_1) = \kappa^2(a(x_1) - a_{N_y}), \tag{II.3.47}$$

with condition

$$\rho(x_{N_y}) = 0. \tag{II.3.48}$$

Then the function

$$\rho(x_1) = \begin{cases} -\left(\dfrac{3\kappa}{2}\displaystyle\int_{x_1}^{x_{N_y}} (a_{N_y} - a(s))^{1/2} ds\right)^{2/3}, & x_1 \le x_{N_y}, \\ \left(\dfrac{3\kappa}{2}\displaystyle\int_{x_{N_y}}^{x_1} (a(s) - a_{N_y})^{1/2}\right)^{2/3} & x_1 > x_{N_y} \end{cases} \tag{II.3.49}$$

satisfies (II.3.47)-(II.3.48).

Proof. Consider first the region of space $x_1 \le x_{N_y}$. The properties of a imply that int this region $a(x_1) - a_{N_y} < 0$, so that any function ρ satisfying (II.3.47) is also negative, and therefore one can write it for convenience as

$$\rho(x_1) = -\varphi(x_1),$$

for some positive function $\varphi(x_1)$. From (II.3.47) one obtains

$$\varphi(x_1)^{1/2}\varphi'(x_1) = \kappa(a_{N_y} - a(x_1))^{1/2} \Rightarrow \frac{2}{3}\left(\varphi(x_1)^{3/2}\right)' = \kappa(a_{N_y} - a(x_1))^{1/2},$$

from which

$$\frac{2}{3}\left(\varphi(x_1)^{3/2} - \varphi(0)^{3/2}\right) = \kappa \int_0^{x_1} (a_{N_y} - a(s))^{1/2} ds.$$

The condition (II.3.48) implies then that

$$\varphi(0)^{3/2} = -\frac{3\kappa}{2} \int_0^{x_{N_y}} (a_{N_y} - a(s))^{1/2} ds,$$

from which it follows that

$$\varphi(x_1)^{3/2} = -\frac{3\kappa}{2} \int_{x_1}^{x_{N_y}} (a_{N_y} - a(s))^{1/2} ds.$$

As for $s \in [x_1, x_{N_y}]$, $x_1 \in [0, x_{N_y}]$, the integrand is positive, in the complex plane one has

$$\varphi(x_1) = \mathrm{e}^{\mathrm{i}\frac{2\pi}{3} + \mathrm{i}\frac{4n\pi}{3}} \left[\frac{3\kappa}{2} \int_{x_1}^{x_{N_y}} (a_{N_y} - a(s))^{1/2} ds\right]^{2/3},$$

which has its only real root for $n = 1$:

$$\varphi(x_1) = \left[\frac{3\kappa}{2} \int_{x_1}^{x_{N_y}} (a_{N_y} - a(s))^{1/2} ds\right]^{2/3}.$$

which coincides with the first part in (II.3.49), recalling that $\rho = -\varphi$. An analogous argument can be used in the region $x_1 > x_{N_y}$, imposing the continuity of the function ρ at $x_1 = x_{N_y}$, in order to conclude the proof. □

Proof of Proposition II.3.5. Consider E^κ as in (II.3.44), with $\varphi = -\rho$, where ρ is given by (II.3.49). Notice that $a' > 0$ implies $\rho' \neq 0$. Applying Helmholtz

operator to $\hat{E}^\kappa$ one obtains

$$\begin{aligned}
&\frac{1}{\kappa^2}\hat{E}^{\kappa\prime\prime} - (N_y^2 + V(x_1))\hat{E}^\kappa \\
&\qquad = \frac{1}{\kappa^2} c(N_y) \left(\rho'' \mathrm{Ai}'(\rho) + (\rho')^2 \mathrm{Ai}''(\rho) - \kappa^2 (a - a_{N_y}) \mathrm{Ai}(\rho)\right) \\
&\qquad = \frac{1}{\kappa^2} c(N_y)(\rho')^2 \left(\frac{\rho''}{(\rho')^2} \mathrm{Ai}'(\rho) + \mathrm{Ai}''(\rho) - \rho \mathrm{Ai}(\rho)\right) \\
&\qquad = \frac{\rho''}{\kappa^2} c(N_y) \mathrm{Ai}'(\rho),
\end{aligned}$$

where the second equality follows from Lemma II.3.1 and the last one is a result of the fact that Ai satisfies Airy equation

$$F''(\rho) - \rho F(\rho) = 0.$$

From (II.3.49) one can observe that $\rho'' \sim \kappa^{2/3}$, while the term $c(N_y)\mathrm{Ai}'(\rho)$ is bounded in κ, so that

$$\frac{\rho''}{\kappa^2} c(N_y) \mathrm{Ai}'(\rho) = \mathcal{O}(\kappa^{-4/3}),$$

which proves the first part of the statement. The fact that the choice of $c(N_y)$ as in (II.3.46) implies that (II.3.44) satisfies the boundary condition (II.3.41b) is of immediate verification. □

Using the asymptotic expansion of the Airy function given in (II.3.18) one can show, with exactly the same argument as in Section II.3.2, that the boundary operator (II.3.41b) selects the incident branch of the wave field on Σ, so that the datum E_0^κ corresponds to the incident part only.

Remark II.3.5.1 (Linear potential)**.** *In the proof of Proposition II.3.5 the only constraint needed on a is $a'(x_1) > 0$. Therefore the result can also be applied to the case of a linear potential, namely, $a(x_1) = x_1$. In this case the solution is exact, and it coincides with the one found in Section II.3.2.*

On the side of the associated Schrödinger equation, as well as for what concerns the reconstructed wave beam, no comment will be made here. Some

numerical tests will be performed by means of the scheme introduced in the next section, and the asymptotic solution computed above will serve as a reference solution.

II.4 Numerical experiments on Helmholtz equation in 2D

In this chapter the method presented in the previous sections is applied to a two-dimensional Helmholtz equation (II.1.1) with different potentials. This should be looked at as a motivation to continue developing both theoretical and computational aspects of the method. In particular, in the future it will be interesting to study its applicability to more general cases of problem (0.2.1), in order to also cover more realistic scenarios which are relevant in the framework of fusion research.

II.4.1 Boundary conditions for Gaussian beams

To test the method of Hagedorn wave packets, a two-dimensional Helmholtz equation was chosen as test model. A particular interest is devoted to Gaussian beams, which are employed in the vast majority of the envisaged applications. Therefore, with respect to problem (II.1.1)-(II.1.2) in two dimensions ($d = 2$), a Gaussian boundary condition is considered, namely,

$$E_0^\kappa(y) = \exp\left(\mathrm{i}\kappa N_{0,y}(y - y_0) - \frac{1}{2}A_0(y - y_0)^2\right), \tag{II.4.1}$$

being $N_{0,y}$ the y-component of the refractive index vector, y_0 the center on the y-axis, and $A_0 \in \mathbb{C}$. One can write A_0 as

$$A_0 = \frac{2}{\kappa w_y^2} + \mathrm{i}\frac{\kappa}{R_y},$$

where w_y and R_y represent the beam width and radius of curvature of the phase front in the y-direction, respectively.

Remark II.4.1.1. *In the previous chapter the boundary datum was assumed to belong to $\mathcal{W}_\kappa(\mathbb{R})$ as defined by (II.3.3). Gaussians do not belong to this space, so that in the applications the evanescent tails, corresponding to the part of the spectrum $N_y^2 > 1$, are cut. The numerical error introduced by this procedure can be neglected in the considered cases.*

In order to find a solution of this boundary-value problem, the initial-value problem (II.1.3) is introduced, where the initial condition is taken in the form

$$u_0^\kappa(x) = a\sqrt{\frac{\kappa}{\pi}}\left(\frac{\kappa}{2}w_{x_1}w_y\right)^{-1/2}\exp\left(\mathrm{i}\kappa N_{0,x_1}(x_1 - x_{0,1}) - \frac{(x_1 - x_{0,1})^2}{\kappa w_y^2}\right)E_0(y),$$

where the center on the x_1-axis $x_{0,1}$ is arbitrary, and the refractive index vector component N_{0,x_1} is such that $N_0 = (N_{0,x_1}, N_{0,y})$ satisfies the dispersion relation

$$-|N_0|^2 - V(x) = 0. \tag{II.4.2}$$

In general, given the potential V and N_y, there will be two solutions of (II.4.2) for N_{x_1}, and the correct branch must be selected consistently with the boundary conditions (cf., Chapter II.3). The parameters a and w_{x_1} are positive scalars which are determined by the optimization step as described in section II.3.3, namely, minimizing the functional

$$F(a, w_{x_1}) := \left\| \int_{\mathbb{R}} u^\kappa[a, w_{x_1}](t, x)dt\big|_\Sigma - E_0(y)\right\|_{L^2(\mathbb{R})}, \tag{II.4.3}$$

where $u^\kappa(t, x)$ is the solution of (II.1.3) with initial condition u_0^κ.

Remark II.4.1.2 (Initial refractive index)**.** *The only constraints on the choice of the initial refractive index N_0 is arbitrary are the dispersion relation and the boundary condition (precisely, the definition of the incident field). Once one of the components is chosen, the other is therefore univocally determined. As N_0 points in the direction of propagation, one can introduce the notion of*

injection angle ϑ *(cf., Section II.1.2), as the angle between the vector* N_0 *and the y-axis. In this way* $N \propto (sin\vartheta, cos\vartheta)$.

II.4.1.1 Solution in the Hagedorn form

Again, one can write u_0^κ as

$$u_0^\kappa(x) = a\sqrt{\frac{\kappa}{\pi}}\left(\frac{\kappa}{2}w_{x_1}w_y\right)^{-1/2}\exp\left(\mathrm{i}\kappa N_0\cdot(x-x_0) - \frac{1}{2}(x-x_0)\cdot A(x-x_0)\right),$$

where $A \in \mathbb{C}^{2\times 2}$. Following the standard description of Gaussian wave packets, one can express A as

$$A = \kappa\phi - \mathrm{i}\kappa S,$$

where ϕ and S, defined as

$$\phi = \begin{pmatrix} \frac{2}{\kappa w_{x_1}^2} & 0 \\ 0 & \frac{2}{\kappa w_{x_1}^2} \end{pmatrix}, \quad S = \begin{pmatrix} 0 & 0 \\ 0 & \frac{1}{R_y} \end{pmatrix} \tag{II.4.4}$$

are the so called width and curvature matrices, respectively. More interestingly, one can show that the matrix $(\mathrm{i}/\kappa)A$ is Hermitian with positive definite imaginary part, so that in virtue of Lemma II.2.1 one can write $A = -\mathrm{i}\kappa PQ^{-1}$, where the matrices Q and P satisfy the symplecticity relations (II.2.2). One can find such decomposition, which gives

$$Q = \begin{pmatrix} \sqrt{\frac{\kappa}{2}}w_{x_1} & 0 \\ 0 & \sqrt{\frac{\kappa}{2}}w_y \end{pmatrix}, \quad P = \begin{pmatrix} \mathrm{i}\sqrt{\frac{2}{\kappa w_{x_1}^2}} & 0 \\ 0 & \mathrm{i}\sqrt{\frac{2}{\kappa w_{x_1}^2}} - \sqrt{\frac{\kappa}{2}}\frac{w_y}{R_y} \end{pmatrix}. \tag{II.4.5}$$

Thanks to this the initial condition u_0^κ can be rewritten as

$$u_0^\kappa(x) = a\sqrt{\frac{\kappa}{\pi}}(\det Q)^{-1/2}\exp\left(\mathrm{i}\kappa N_0\cdot(x-x_0) + \frac{\mathrm{i}\kappa}{2}(x-x_0)\cdot PQ^{-1}(x-x_0)\right),$$

so that actually

$$u_0^\kappa(x) = a\varphi_0^\kappa[x_0, N_0, Q, P](x)$$

is expressed in the Hagedorn form. This means that the Hagedorn wave packet

$$u^\kappa(t,x) = a\mathrm{e}^{\mathrm{i}\kappa S(t)}\varphi_0^\kappa[x(t),N(t),Q(t),P(t)](x) \tag{II.4.6}$$

is an approximation of the solution of (II.1.3), which is exact for the case of a quadratic potential, being $(x(t),N(t),Q(t),P(t))$ solution of (II.3.30) and $S(t)$ given by (II.3.31).

This is the solution computed in the numerical experiments presented in this chapter, and it is then compared to the analytic solution (exact or asymptotic) of Helmholtz equation as computed for the various cases in the previous chapter. In the future more elements of the L^2-basis $\{\varphi_k^\kappa\}$ can be added to the Hagedorn solution to increase the accuracy of the approximation for the non-quadratic cases (cf., equation (II.2.12)).

II.4.2 Details on the implementation

The numerical tests that follow this section are the result of a prototype-implementation of the scheme presented in section II.3.3. The code is written in `Python`, and there was so far no real effort to optimize its performance. Here are some details concerning the different building blocks of the scheme as presented in the previous chapter.

Optimization of the initial condition

As in general it is not possible to solve Problem II.2 analytically, which is, to find minima of the functional (II.4.3), a routine for numerical optimization is used. So far the choice was to use the `scipy` routine `scipy.optimize.minize` [79]. It gives the possibility to choose among different minimization algorithms, and the Nelder-Mead [59] algorithm is the one picked for the simulations included in this work.

Notice that the optimization procedure actually requires to solve (II.1.3) at each step with a different initial condition, and to integrate the solution in time, until convergence. The fact that this procedure can be performed

independently at each point in space, allows one to restrict the calculations for this step to points on Σ.

Solution of the ODEs

For the case of constant and linear potentials the ODEs can be integrated analytically (cf., sections II.4.3 and II.4.4. When no analytic solution is available, the order 5 Runge-Kutta integrator `dopri5` from the `scipy.integrate.ode` class is used [78].

Time integration

In general it is not possible to time-integrate the solution u^κ of (II.1.3) analytically, so that some quadrature formula is necessary in order to reconstruct the stationary field. First of all a finite time interval where the wave packet is localized needs to be identified and discretized. Then the choice so far was to use a standard trapezoid formula, and currently one can choose between two different implementations, each with its advantages and disadvantages:

- **Using `numpy`** The first possibility is to allocate the whole wave packet, evaluated on an array t and a grid (x_1, y) into a multidimensional `numpy` array, and then use the routine `numpy.trapz` [60] to integrate along the dimension corresponding to t. This method is pretty fast, as it exploits the optimized operations of `numpy`, but highly memory-consuming. This procedure could be parallelized in the future, by subdividing the wave packet array among different CPUs. This has not been attempted so far.

- **Performing a swipe in time** The second possibility is to run a swipe over time, and deposit the contribution to the integral at points on the grid at each discrete time t_j. More precisely, for each time t_j the quantity

$$\frac{\Delta t}{2}(u(t_j, x_k) + u(t_{j+1}, x_k))$$

  is added to the value of the integral at each point x_k on the spatial grid.

This way of proceeding is more time-consuming, but on the other side it uses way less memory than the first one. It also seems suitable for parallelization, by assigning time sub-intervals to different CPUs. This possibility has not been explored yet.

The use of a simple trapezoid rule does not appear optimal: in case of very high frequency, smaller integration steps are required, so that in the case of large computations one might want to improve performance. One could dig in the direction of quadrature formulas specifically designed for highly oscillatory functions, or look for clever approximations of the integrand such that analytic calculations can be done. That said, as briefly mentioned above, parallelization is also a practicable way.

II.4.3 Numerical tests I: constant potential

The simplest scenario that can be considered is that of an electromagnetic wave propagating in free space. In terms of equations, problem (II.3.2) - and therefore (II.3.7) - is being considered. In this case (II.4.6) is an exact solution of (II.3.7). The ODEs describing the parameters are trivial to integrate, giving

$$x(t) = x_0 + 2N_0 t, \qquad N(t) = N_0, \tag{II.4.7a}$$

$$Q(t) = Q + 2Pt, \qquad P(t) = P, \tag{II.4.7b}$$

and the action integral amounts to

$$\begin{aligned} S(t) &= \int_0^t \Big(|N(s)|^2 - V\big(x(s)\big) \Big) ds \\ &= (|N_0|^2 + 1)t = 2t, \end{aligned} \tag{II.4.8}$$

as N_0 must satisfy the dispersion relation which in this case has the form

$$|N|^2 = 1.$$

The central trajectory of the beam is a straight line, whose direction is given by the initial refractive index vector (and therefore, by the injection angle ϑ). For simplicity scenarios of perpendicular propagation ($\vartheta = 90°$) will be considered. As mentioned above, in this simple framework some interesting phenomena can already be observed. In particular, the choice of a finite radius of curvature R_y will produce a focused beam, the focus being a caustic, which for example the standard WKB-method (ray tracing) fails to resolve. Other methods (e.g., beam tracing, wave kinetic equation) are able to reconstruct the field in the focus region, but still this is a first test for the method of Hagedorn wave packets applied to wave beams.

Quantity	**Symbol**	**Value**
Semiclassical parameter	κ	$2.36 \cdot 10^2$
Beam center	x_0	$(0, 0)$
Refractive index	N_0	$(1, 0)$
Beam width	w_y	0.18
Injection angle	ϑ	$90°$
Integration time-step	Δt	$5 \cdot 10^{-3}$
Spatial domain	(x_1, y)	$\in [0, 1.3] \times [-\pi, \pi]$
Number of points in x_1	$nptx$	1024
Number of points in y	$npty$	2048

Table II.4.1: Parameters common to all simulations for the case $V(x) = -1$. Different scenarios will be considered, corresponding to different choices of the radius of curvature R_y.

Two different scenarios will be analyzed in what follows, corresponding to different choices of the radius of curvature R_y. The parameters which are common to all simulations are reported in Table II.4.1. Note that the beam parameters (κ and the beam width w_y) are chosen as the typical parameters of the electron-cyclotron beams in ASDEX-Upgrade [97, 50].

II.4.3.1 Non-diffracting wave beam: $1/R_y = 0$

The first case considered is the simplest one, where no caustic is present and the beam parameters are such that diffraction does not alter the beam structure. This case is characterized by wave fronts with zero curvature, corresponding to the choice $1/R_y = 0$. As R_y appears always at the denominator in the equations, the terms containing it are neglected in this case.

Optimal initial condition and reconstructed boundary profile

The optimization routine reconstructs the boundary conditions with parameters given in Table II.4.1 and $R_y = 10^9$, returning the optimal parameters a and w_{x_1} for the initial wave packet u_0, which are reported in Table II.4.2, together with the L^∞-norm error they produce at the boundary. The reconstructed boundary condition together with the difference with the designed launched beam are represented in Figure II.4.1a-II.4.1b.

Quantity	**Symbol**	**Value**
Amplitude factor	a	1.4447
Packet width (x_1-direction)	w_{x_1}	0.0899
L^∞-norm error		$\sim 10^{-4}$

Table II.4.2: Optimal wave-packet parameters and corresponding L^∞-norm error at the boundary, for the case of a straight beam ($R_y \to \infty$).

Wave packet dynamics

The wave-packet, whose parameters in this case can be computed analytically (cf., (II.4.7)-(II.4.8)), is subject only to diffraction effects. The absence of curvature ($1/R_y = 0$) and the large value of κ result in a pretty simple dynamics, with no focusing and no significant diffractive broadening, as shown in Figure II.4.1c.

Reconstructed wave beam

Time integration of the wave packet provides the reconstructed wave beam, as shown in Figure II.4.1d. This can be compared to the exact solution of Helmholtz equation, and the corresponding error (absolute value of the difference) is shown in Figure II.4.1e. Notice that the scheme does not produce any additional error to the one at the boundary (cf., Figure II.4.1b), whose structure is simply translated through the whole domain. It is not surprising in this case, as the Hagedorn wave packet is an exact solution of Schrödinger equation, and therefore no error propagation is expected.

Constant potential, $1/R_y = 0$

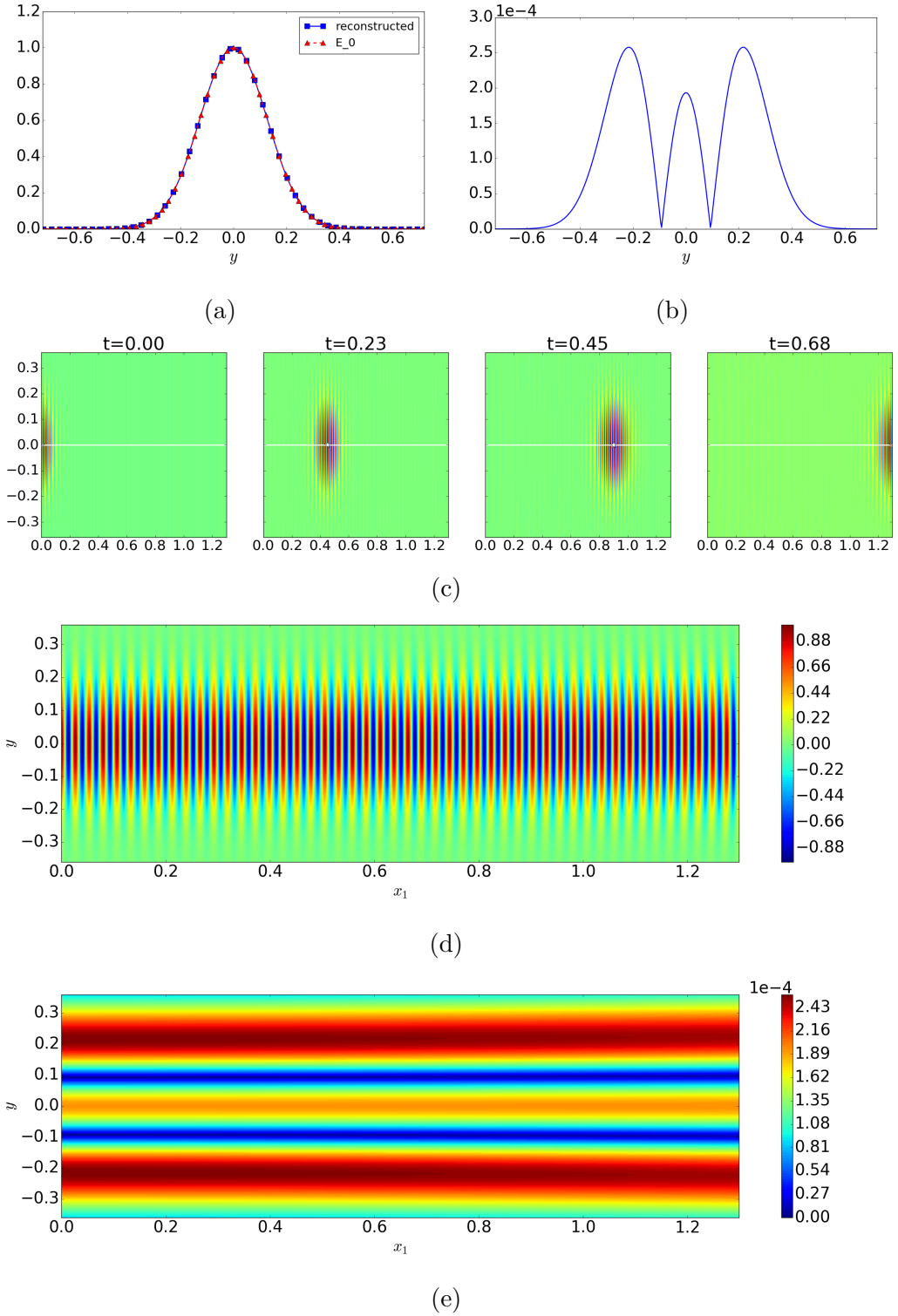

Figure II.4.1: Non-diffracting beam ($1/R_y = 0$) (a) Launched beam and reconstructed boundary data, and (b) difference between the two. (c) Wave packet at different times. (d) Reconstructed wave beam and (e) absolute value of the difference with respect to the exact solution.

II.4.3.2 Focused beam: $R_y = 0.5$

The case of a focused beam faces the method proposed in this work with a caustic - the focal point - which sees standard ray-tracing methods fail. Being the method of Hagedorn wave packets similar in many aspects to beam tracing, it is not surprising that this singularity can be reproduced without problems.

Optimal initial condition and reconstructed boundary profile

In this case the optimization routine is aimed to reconstruct the boundary condition with $R_y = 0.5$. It returns the values a and w_{x_1} for the optimal initial wave packet u_0 reported in Table II.4.3, together with the L^∞-norm error they produce at the boundary (cf., Figure II.4.2a-II.4.2b).

Quantity	**Symbol**	**Value**
Amplitude factor	a	5.5040
Packet width (x_1-direction)	w_{x_1}	0.0233
L^∞-norm error		$\sim 10^{-2}$

Table II.4.3: Optimal wave-packet parameters and corresponding L^∞-norm error at the boundary, for the case of a focused beam ($R_y = 0.5$)

Wave packet dynamics

The wave packet dynamics is represented by the snapshots in Figure II.4.2c. A narrowing of the packet in the vicinity of the focus can be observed, as one can expect looking at the analytic solution of the ODEs (II.4.7)-(II.4.8), keeping in mind that now a non-zero term $1/R_y$ is present in the expression for the matrices (cf., (II.4.5)).

Reconstructed wave beam

The reconstructed focused beam is represented in Figure II.4.2d. It is again interesting to notice that the structure of the error at the boundary is con-

served in the whole domain, as one can notice comparing Figure II.4.2b to Figure II.4.2e.

In absolute terms, the accuracy of the reconstructed boundary condition is significantly lower than in the previous case. This reflects in a higher error on the reconstructed beam in the whole domain. This is due to the oscillating tails of the profile, determined by the effect of the non-trivial curvature radius, and can be fixed in the future with a more efficient implementation of the algorithm to increase resolution on the y-axis. For the scope of this work, it is sufficient to notice how the error in the whole spatial domain is of the same order of that at the boundary.

Constant potential, $R_y = 0.5$

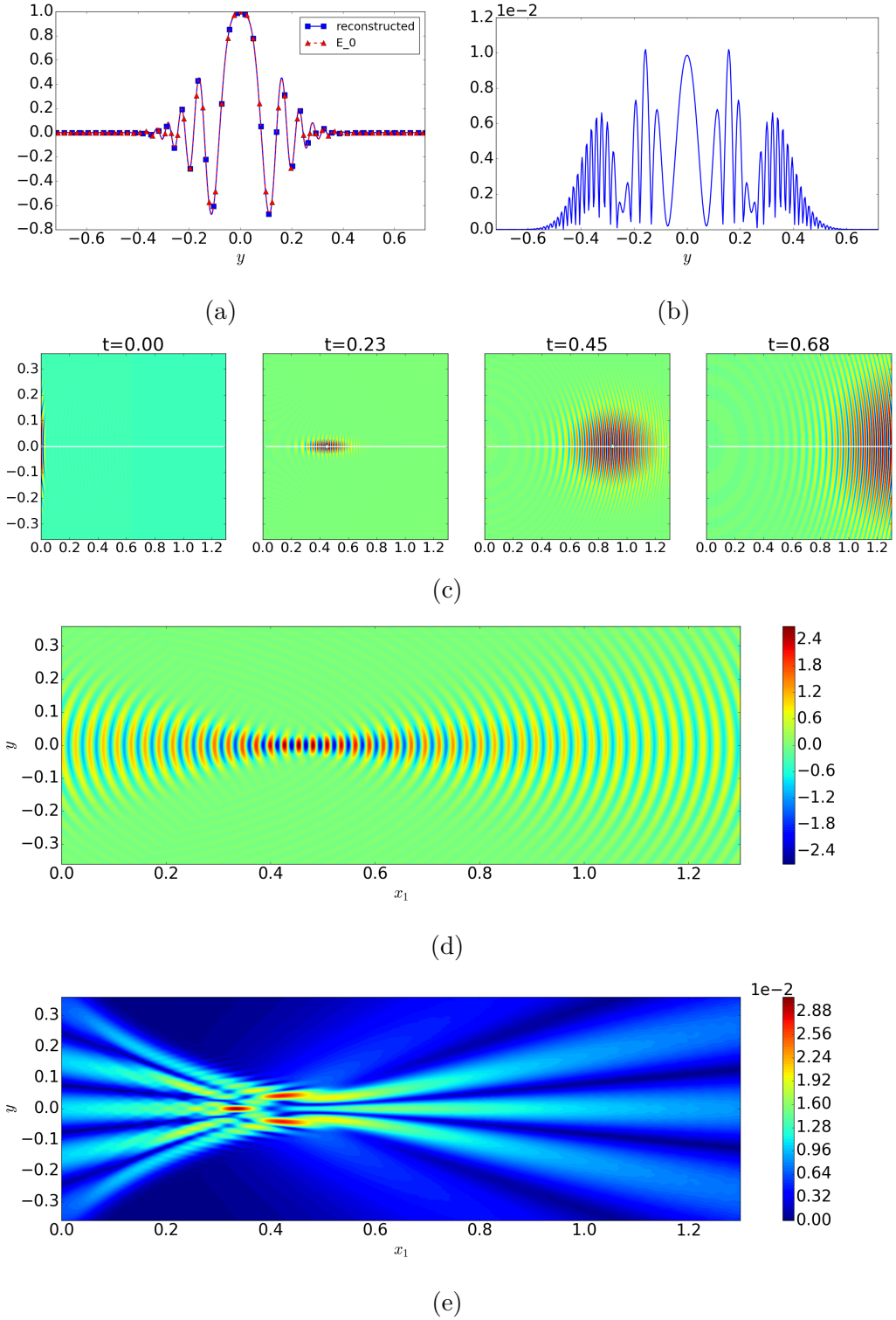

Figure II.4.2: Focused beam ($R_y = 0.5$) (a) Launched beam and reconstructed boundary data, and (b) difference between the two. (c) Wave packet at different times. (d) Reconstructed wave beam and (e) absolute value of the difference with respect to the exact solution.

II.4.4 Numerical tests II: linear potential

The second scenario considered is that of a linear potential $V(x) = x_1 - 1$, namely, (II.3.12). The wave beam is reflected at a cut-off located at the position $x_1 = 1$. Again, the Hagedorn packet (II.4.6) is an exact solution of the associated Schrödinger equation (II.3.20). The ODEs describing the parameters can be integrated analytically, giving

$$x_1(t) = x_{0,1} + 2N_{0,x_1}t - t^2, \qquad N_{x_1}(t) = N_{0,x_1} - t, \tag{II.4.9a}$$

$$y(t) = y_0 + 2N_{0,y}t, \qquad N_y(t) = N_{0,y}, \tag{II.4.9b}$$

$$Q(t) = Q + 2Pt, \qquad P(t) = P, \tag{II.4.9c}$$

and the action integral is given by

$$\begin{aligned} S(t) &= \int_0^t \Big(|N(s)|^2 - V\big(x(s)\big)\Big) ds \\ &= (|N_0|^2 + 1)t - 2N_{0,x_1}t^2 + \frac{2t^3}{3}. \end{aligned} \tag{II.4.10}$$

In this case the dispersion relation is given by $|N|^2 - 1 - x_1 = 0$, so that if for instance one chooses $x_{0,1} = 0$, then one has $|N_0|^2 = 1$ and therefore the action can be rewritten as

$$S(t) = 2t - 2N_{0,x_1}t^2 + \frac{2t^3}{3}.$$

This will be the case for all the tests presented here. In particular this implies that it is sufficient to give the injection angle ϑ as an input (cf., Remark II.4.1.2), and N_0 will be given by

$$N_0 = (\sin\vartheta, \cos\vartheta). \tag{II.4.11}$$

The central trajectory of the beam in the considered case is a parabola, which reaches its maximum $\bar{x} = (x_{0,1} + N_{0,x_1}^2, y_0 + 2N_{0,x_1}N_{0,y})$ at $t = N_{0,x_1}$. This can

be expressed in terms of the angle ϑ as well, giving

$$\bar{x}_1 = \sin^2\vartheta, \quad \bar{y} = y_0 + \sin 2\vartheta. \tag{II.4.12}$$

Being y_0 also a free parameter, we choose $y_0 = -\sin 2\vartheta$, so that the turning point will be at $\bar{y} = 0$ and the reflected beams will present symmetry with respect to the x_1-axis independently from the injection angle ϑ.

Quantity	**Symbol**	**Value**
Semiclassical parameter	κ	$2.36 \cdot 10^2$
Beam center	x_0	$(0, -\sin 2\vartheta)$
Refractive index	N_0	$(\sin\vartheta, \cos\vartheta)$
Beam width	w_y	0.18
Phase front curvature	$1/R_y$	0
Integration time-step	Δt	5×10^{-3}
Spatial domain	(x_1, y)	$\in [0, 1.2] \times [-\pi, \pi]$
Number of points in x_1	$nptx$	1024
Number of points in y	$npty$	2048

Table II.4.4: Parameters common to all simulations, for the case of a linear potential $V(x) = x_1 - 1$. Different scenarios are identified with the choice of the injection angle ϑ.

Different scenarios will now be considered, corresponding to different choices of the angle ϑ.

II.4.4.1 Small angle (BT validity limit): $\vartheta = 60°$

The first case considered corresponds to a scenario which is still included within the limits of validity of beam-tracing [50], being the radius of curvature of the beam central trajectory large enough with respect to the transversal beam width, so that no significant interference pattern occurs.

Optimal initial condition and reconstructed boundary profile

The minimization routine returns the value a and w_{x_1} which characterize the optimal initial wave packet. Such values are reported in Table II.4.5, together with the error on the launching condition (boundary value of the incoming branch of the wave beam). The launched beam profile, and its reconstruction with the Hagedorn packets method, are presented in Figure II.4.3a-II.4.3b.

Quantity	**Symbol**	**Value**
Amplitude factor	a	5.8229
Packet width (x_1-direction)	w_{x_1}	0.0193
L^∞-norm error		$\sim 10^{-2}$

Table II.4.5: Optimal wave-packet parameters and corresponding L^∞-norm error at the boundary on the launching condition, for the case of an injection angle of 60°.

Wave packet dynamics

The wave packet is entirely described by equations (II.4.9)-(II.4.10): the center of the packet follows the parabolic trajectory in (II.4.9a), which is represented by the white line in Figure II.4.3c, while the evolution of its amplitude, width and curvature is described by the other above mentioned equations.

Reconstructed wave beam

As a consequence of the packet dynamics, the reconstructed beam is reflected at the cutoff (cf., Figure II.4.3d), being the turning point as described in II.4.12. The error with respect to the exact solution is in the whole domain of the same order of magnitude as at the boundary, as one can observe comparing Figures II.4.3b and II.4.3e.

In this case as well the value at the boundary is reconstructed with low accuracy. This is due to the fact that the beam is Gaussian on a plane which has a positive angle with respect to the domain boundary, so that the projection on the $\{x_1 = 0\}$ axis presents the oscillating tails that can be observed in

Figure II.4.3a. This issue can be fixed by implementing a suitable coordinate transformation, but at present it is sufficient to observe again how the error in the whole domain is of the same order as the one at the boundary.

Linear potential, $\vartheta = 60°$

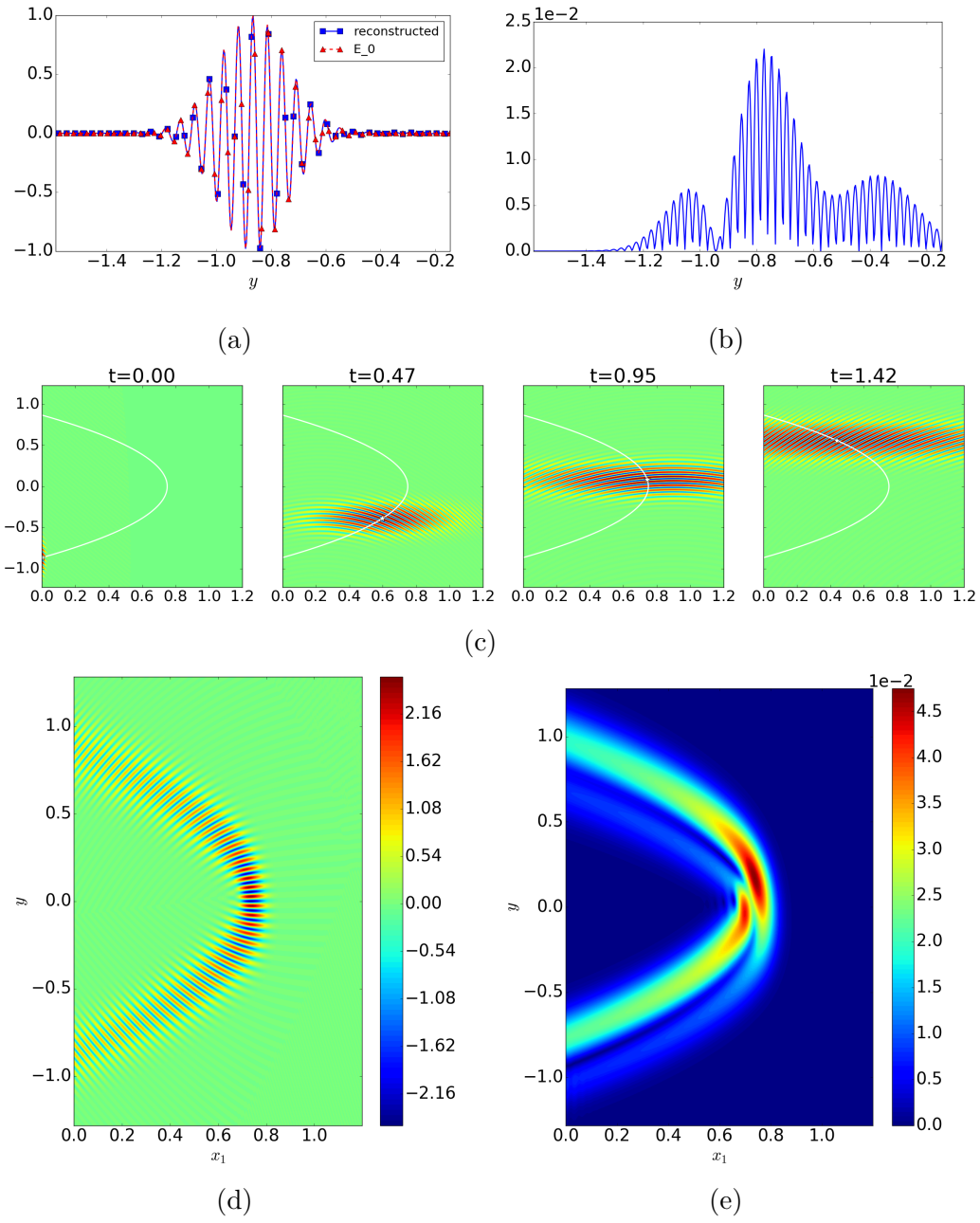

Figure II.4.3: Injection angle $\vartheta = 60°$. (a) Launched beam and reconstructed boundary data, and (b) difference between the two. (c) Wave packet at different times and trajectory of the wave packet center (white line). (d) Reconstructed wave beam and (e) absolute value of the difference with respect to the exact solution.

II.4.4.2 Larger angle (BT breaks): $\vartheta = 80°$

A case of injection angle close to normal to the cutoff is also considered. As mentioned in section II.1.2, this is a critical case for beam tracing methods, due to the presence of an interference region (cf., Figure II.1.2).

Optimal initial condition and reconstructed boundary profile

The optimal initial wave packet amplitude and width are reported in Table II.4.6, together with the error on the launching condition, whose reconstruction is shown in Figure II.4.4a-II.4.4b.

Quantity	**Symbol**	**Value**
Amplitude factor	a	6.9099
Packet width (x_1-direction)	w_{x_1}	0.0184
L^∞-norm error		$\sim 10^{-2}$

Table II.4.6: Optimal wave-packet parameters and corresponding L^∞-norm error at the boundary on the launching condition, for the case of an injection angle of 80°.

Wave packet dynamics

The wave packet follows the dynamic described by equations (II.4.9)-(II.4.10), as shown in Figure II.4.4c, where the parabolic center trajectory is represented with a white line. The dynamics induces a strong curvature of the phase fronts and broadening of the wave packet in the x_1-direction.

Reconstructed wave beam

The time integration successfully reconstructs the beam in the whole domain, including the region where the injected and reflected branches interfere (cf., Figure II.4.4d). The wave packets method overcomes the limitations of beam tracing, and it is suitable for a broader range of reflectometry applications.

Linear potential, $\vartheta = 80°$

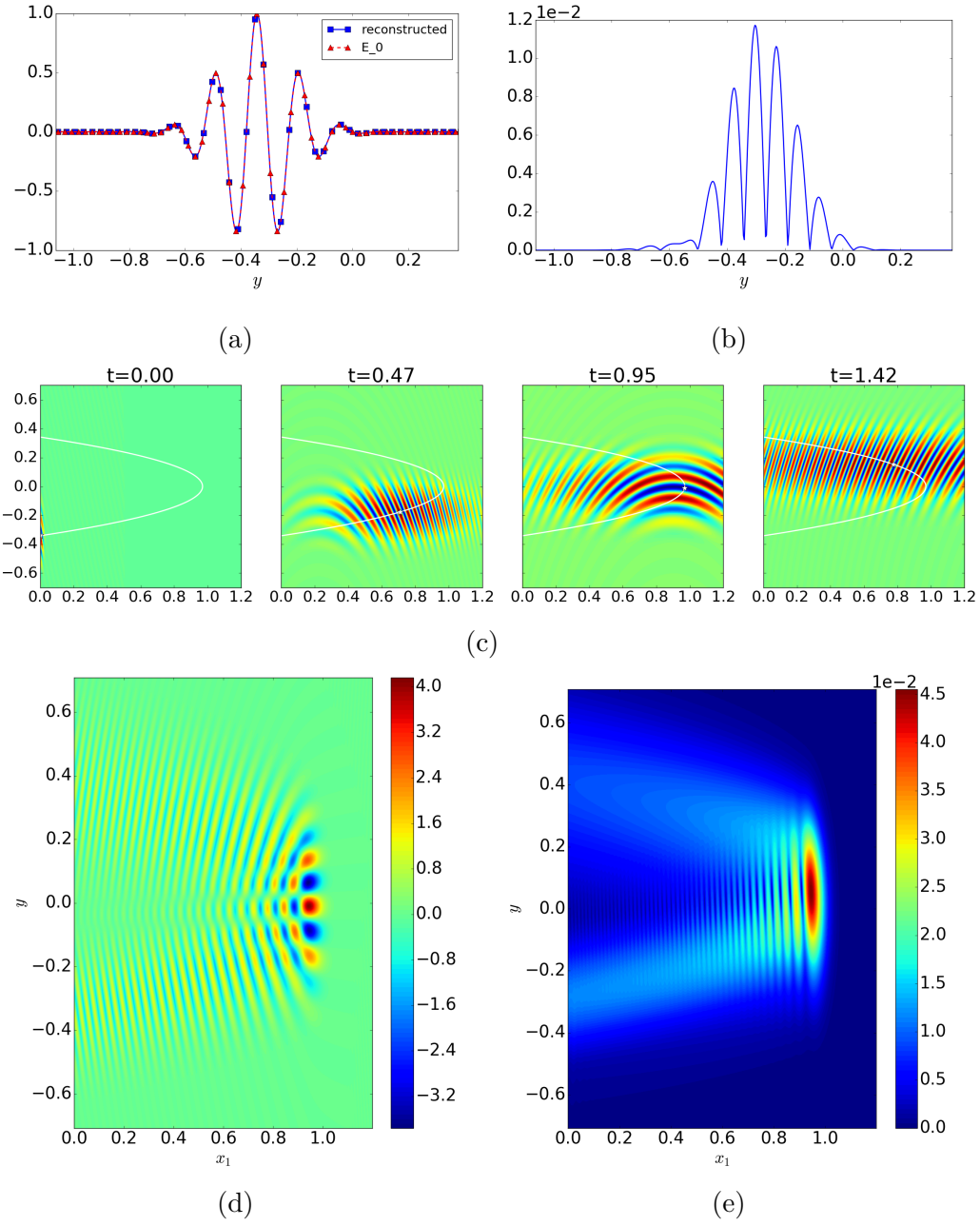

Figure II.4.4: Injection angle $\vartheta = 80°$. (a) Launched beam and reconstructed boundary data, and (b) difference between the two. (c) Wave packet at different times and trajectory of the wave packet center (white line). (d) Reconstructed wave beam and (e) absolute value of the difference with respect to the exact solution.

II.4.4.3 Perpendicular injection: $\vartheta = 90°$

As a last test-case, an injection angle of 90° is considered, corresponding to a wave beam perpendicular to the cutoff, with phase fronts parallel to it. In this case the beam is reflected in such a way that the incoming and reflected branches are overlapped in the whole domain. Beam tracing methods fail to reconstruct the beam at any point in the domain in this case.

Optimal initial condition and reconstructed boundary profile

The optimal initial condition parameters are reported in Table II.4.7, together with the error on the launching condition (cf., Figure II.4.6a-II.4.6b).

Quantity	**Symbol**	**Value**
Amplitude factor	a	7.0418
Packet width (x_1-direction)	w_{x_1}	0.0184
L^∞-norm error		$\sim 10^{-4}$

Table II.4.7: Optimal wave-packet parameters and corresponding L^∞-norm error at the boundary on the launching condition, for the case of an injection angle of 90°.

An issue arises for this case, due to the broadening of the packet in the x_1-direction (cf., Figure II.4.6c). As shown in Figure II.4.5, if one looks at the time-profile of the wave packet at a fixed position, the two peaks - corresponding to the incoming and reflected components, respectively - are slightly overlapped. One must be careful selecting the time interval to integrate on during the optimization step, in order to isolate the incoming branch as much as possible.

Wave packet dynamics

Equations (II.4.9)-(II.4.10) describe the wave packet, whose center follows the straight line (degenerate parabola) represented by the white line in Figure II.4.6c. Notice the strong broadening in the x_1-direction, which is due

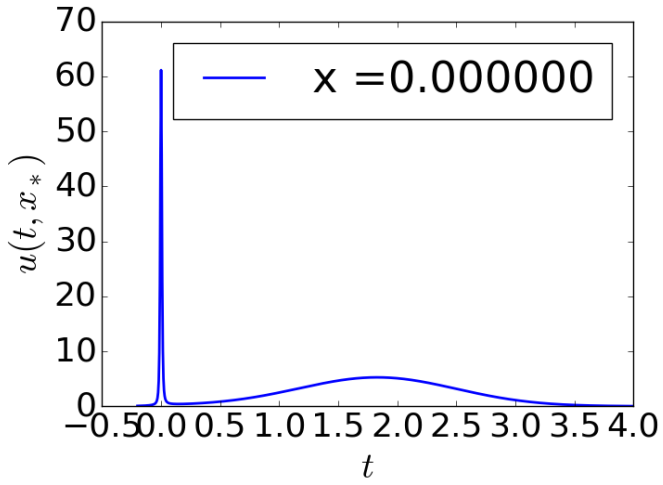

Figure II.4.5: Wave packet as a function of time at a fixed position in space $x = (0, 0)$.

to the extremely small beam-width resulting from the optimization step (cf., Table II.4.7). Also here the phase fronts develop a strong curvature.

Reconstructed wave beam

The wave field is successfully reconstructed even in this limit reflectometry test, as shown in Figure II.4.6d. The propagation of the boundary error in the domain could be explained by the discussion around Figure II.4.5.

Linear potential, $\vartheta = 90°$

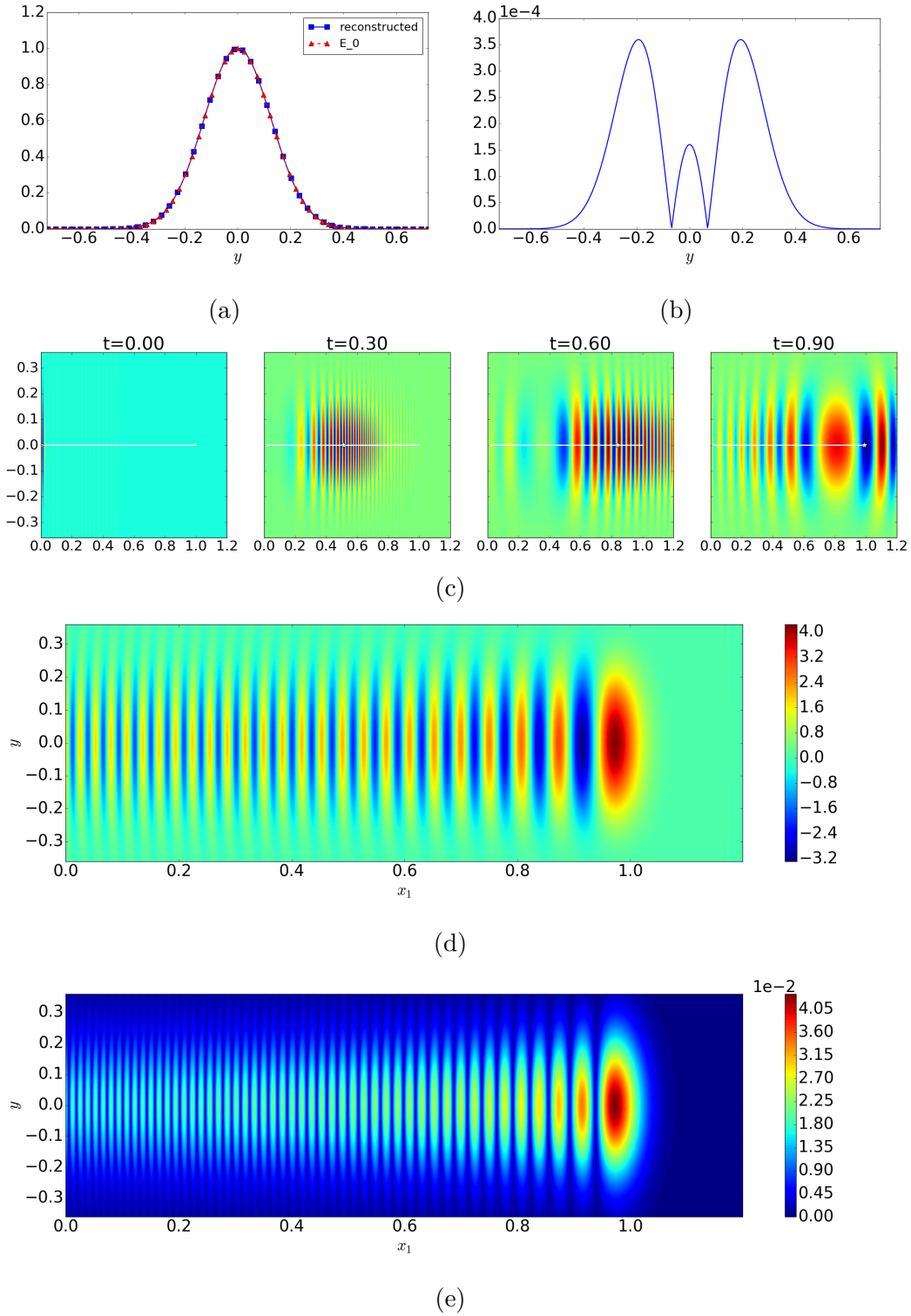

Figure II.4.6: Injection angle $\vartheta = 90°$. (a) Launched beam and reconstructed boundary data, and (b) difference between the two. (c) Wave packet at different times and trajectory of the wave packet center (singular parabola, white line). (d) Reconstructed wave beam and (e) absolute value of the difference with respect to the exact solution.

II.4.5 Numerical tests III: non-quadratic potential

In the numerical tests presented in the previous two sections the Hagedorn wave packet is an exact solution of Schrödinger equation with the considered (constant or linear) potential. That means that the only sources of error were the optimization of the initial condition and numerical errors related to the quadrature of the time integral. If the potential is non-quadratic, the Hagedorn wave packet does not satisfy the Schrödinger equation exactly, and a new source of error is introduced. This section is aimed to explore its impact on the reconstructed wave beam, having Propositions II.3.3 and II.3.4 in mind.

II.4.5.1 Model: smooth increasing potential

The Helmholtz equation with a potential of the form $V(x) = a(x_1) - 1$ is considered here (cf., (II.3.41)), with

$$a(x_1) = \alpha_c \left(\frac{1}{2} + \frac{1}{\pi} \arctan\left(\frac{x - x_p}{L} \right) \right), \tag{II.4.13}$$

where $\alpha_c > 1$, and parameters L and x_p. The function $a = a(x_1)$ has the properties listed in (II.3.40), and as discussed in Section II.3.5 a cut-off point for the associated Helmholtz equation exists, solution of $a(x_1) = 1$. This type of potential is often used to describe electron density profiles in fusion plasmas, and L represents the scale of variation of the medium. For the simulations below $\alpha_c = 2$ is taken, which implies a cut-off at $x_1 = x_p = 1$. Two cases are presented, corresponding to two choices of L, in order to show the behaviour of the method in relation to certain properties of the medium. The potentials V corresponding to the different choices of L are shown in (cf., Figure II.4.7). For the numerical test presented here, the common parameters are listed in Table II.4.8.

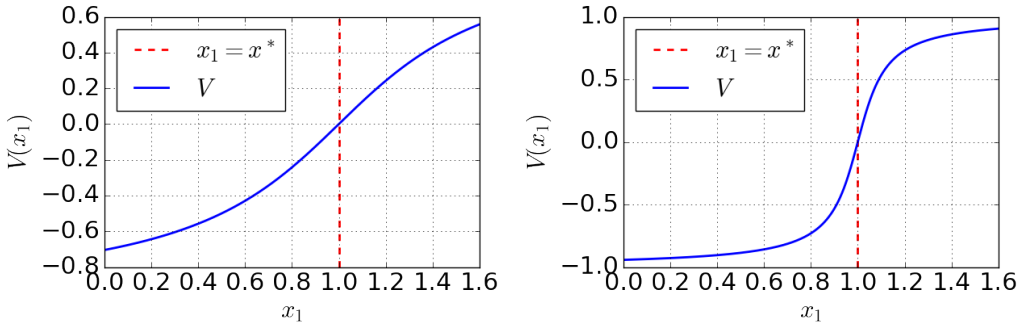

(a) (b)

Figure II.4.7: Potential profiles V defined in (II.4.13), with parameters $\alpha_c = 2$, $x_p = 1$ and (a) $L = 0.5$, and (b) $L = 0.09$.

Quantity	**Symbol**	**Value**
Semiclassical parameter	κ	$2.36 \cdot 10^2$
Beam center	x_0	$(0, 0)$
Refractive index	N_0	$(1, 0)$
Beam width	w_y	0.18
Phase front curvature	$1/R_y$	0
Injection angle	ϑ	$90°$
Integration time-step	Δt	$5 \cdot 10^{-3}$
Spatial domain	(x_1, y)	$\in [0, 1.] \times [-\pi, \pi]$
Number of points in x_1	$nptx$	2048
Number of points in y	$npty$	2048

Table II.4.8: Parameters of the simulation for the case of the non-quadratic potential defined in (II.4.13).

II.4.5.2 Slowly varying medium: $L = 0.5$

The first case considered corresponds to the choice $L = 0.5$, which corresponds to the potential in Figure II.4.7a.

Optimal initial condition and reconstructed boundary profile

The optimal parameters returned by the optimization routine are listed in Table II.4.9, together with the corresponding L^∞-norm error on the incident field evaluated at boundary (cf., Figure II.4.8a-II.4.8b).

Quantity	**Symbol**	**Value**
Amplitude factor	a	5.7508
Packet width (x_1-direction)	w_{x_1}	0.0189
L^∞-norm error		$\sim 10^{-4}$

Table II.4.9: $L = 0.5$ - Optimal wave-packet parameters and corresponding L^∞-norm error at the boundary on the launching condition.

Wave packet dynamics

The ODEs describing the wave packet parameters are integrated numerically, and the resulting dynamics is illustrated in Figure II.4.8c. One can observe the packet significantly spreading in the x_1-direction.

Reconstructed wave beam

The accuracy of the reconstruction is not satisfactory in this case, as one can observe in Figure II.4.8d-II.4.8e. The approximation error on the solution of Schrödinger equation here seems to play a role: the reconstructed solution presents a qualitative agreement with the analytic one (cf., Figure II.4.9), but still a significant error is introduced. Using a higher order Hagedorn functions in the approximation will help solving this issue, as one can expect by the results recalled in Chapter II.2.

Non-quadratic potential (II.4.13), $L = 0.5$

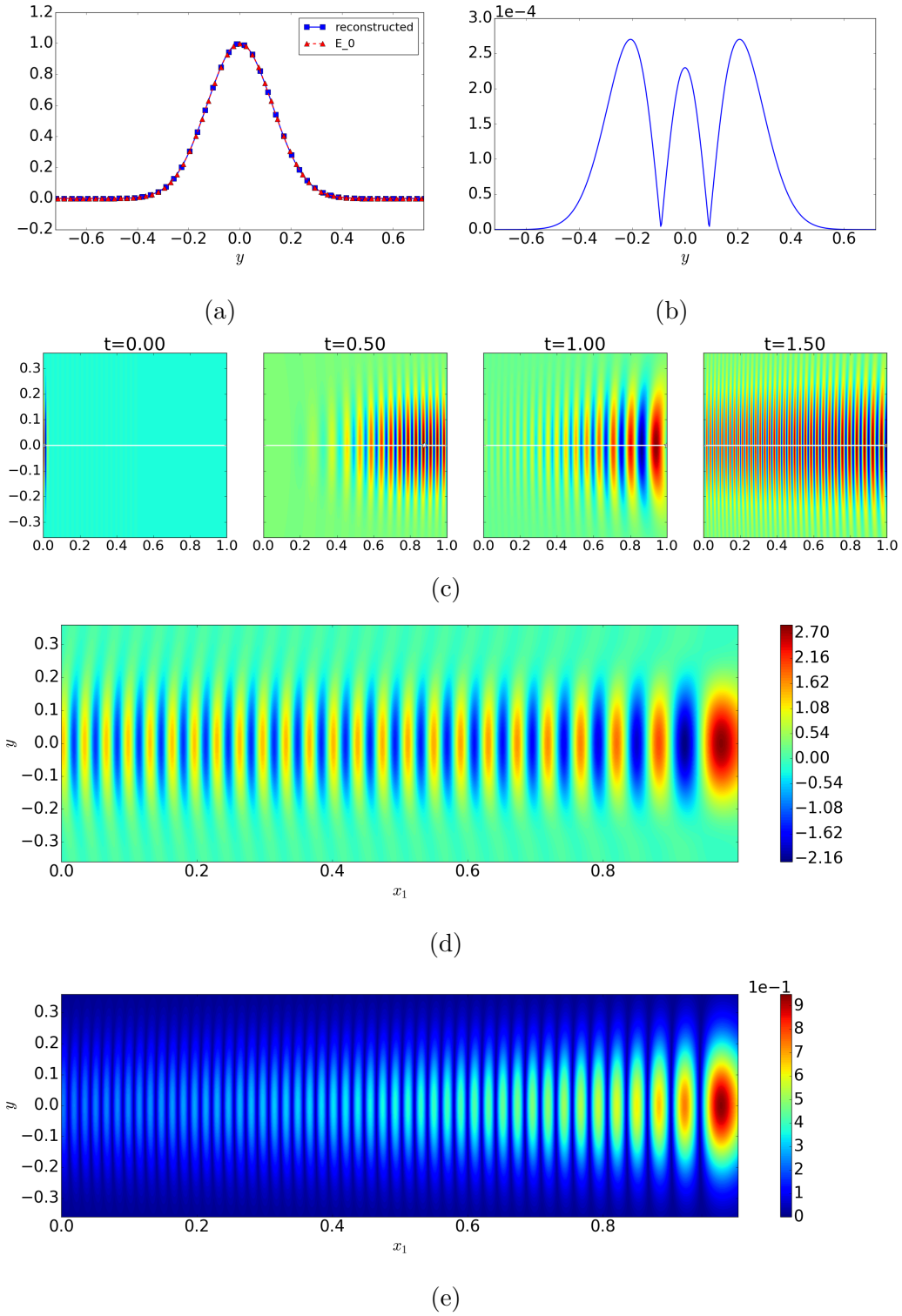

Figure II.4.8: (a) Launched beam and reconstructed boundary data, and (b) difference between the two. (c) Wave packet at different times and trajectory of the wave packet center (white line). (d) Reconstructed wave beam and (e) absolute value of the difference with respect to the exact solution.

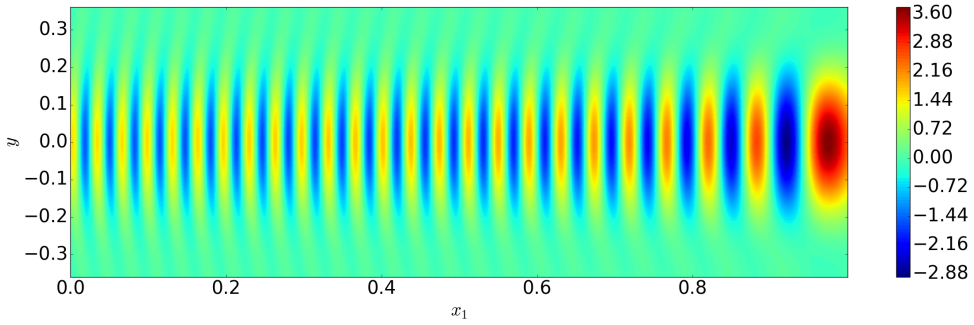

Figure II.4.9: Asymptotic solution of Helmholtz equation in the case $L = 0.5$ (cf., Section II.3.5).

II.4.5.3 Rapidly varying medium: $L = 0.09$

In this second case considered here the potential V has a steeper profile, corresponding to a larger deviation from its quadratic approximation. For this reason the ability of the method of Hagedorn wave packet to reconstruct the correct wave beam is compromised, and a large error is to be expected in the region of large variation of the potential.

Optimal initial condition and reconstructed boundary profile

The optimization step is run as in the previous test-cases, providing parameters for the initial condition which are expressed in Table II.4.10, together with the L^∞-norm error of the reconstructed boundary values with respect to data of the problem (cf., Figure II.4.11a-II.4.11b).

Quantity	**Symbol**	**Value**
Amplitude factor	a	4.5693
Packet width (x_1-direction)	w_{x_1}	0.0276
L^∞-norm error		$\sim 10^{-4}$

Table II.4.10: Optimal wave-packet parameters and corresponding L^∞-norm error at the boundary on the launching condition.

Wave packet dynamics

For what concerns the evolution of the parameters which define the wave packet, in this case numerical integration of the ODEs is necessary. The resulting wave packet is illustrated in Figure II.4.11c.

Reconstructed wave beam

The time integral in this case does not reconstruct the correct wave beam, as one can clearly see in Figure II.4.11d-II.4.11e. The reconstructed profile is clearly very different from what one can expect, namely, the asymptotic solution as computed in Section II.3.5 shown in Figure II.4.10c. The large difference with respect to the reference solution confirms the qualitative observation. The next section is dedicated to an analysis of the Poynting flux for the different cases presented here, based on the results of Section II.3.4. This will clarify how the failure of the method for this specific test-case is related to the mentioned results. The inaccuracy of the reconstructed solution though is localized in the region near the cut-off. A closer look to the solution on the "antenna plane" (i.e., the $\{x_1 = 0\}$ line), accounting for both the incident and reflected branches, shows how the beam profile at this location is reconstructed successfully, as it appears from Figure II.4.10a-II.4.10b. Therefore the reflected branch is correctly reproduced, and the error appears localized in a precise region of space (cf., Section II.4.6) and does not propagate.

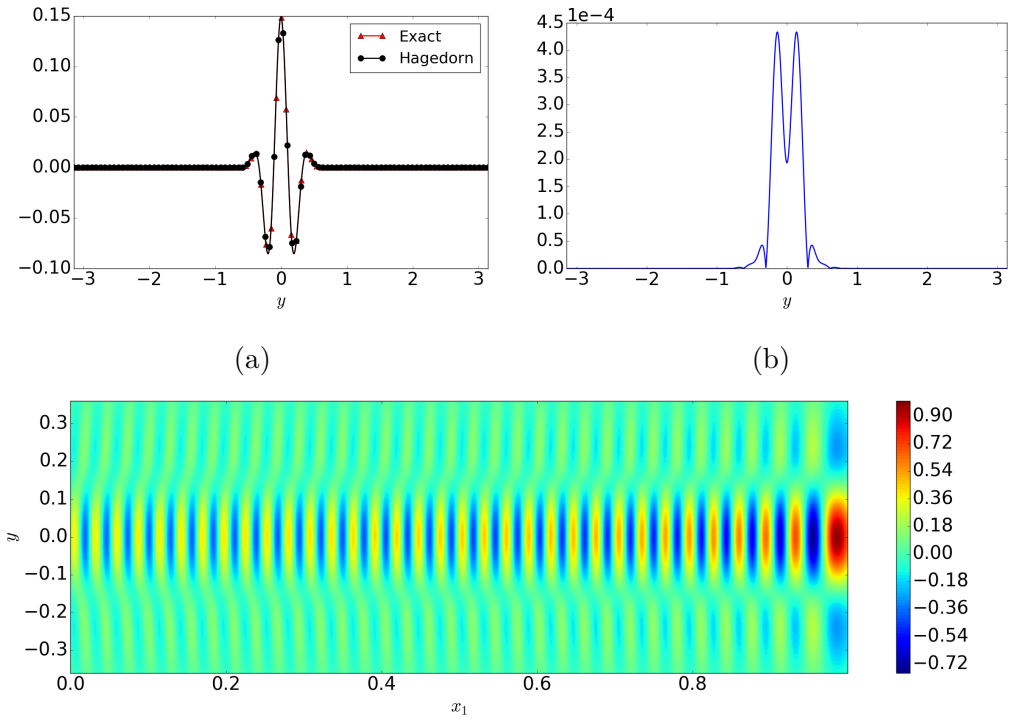

Figure II.4.10: $L = 0.09$. (a) Beam profiles on the "antenna plane" $\Sigma = \{x_1 = 0\}$, corresponding to the Hagedorn and reference solution. Both the incoming and reflected branch are accounted for. (b) Difference between the two. (c) Asymptotic solution of Helmholtz equation (cf., Section II.3.5).

Non-quadratic potential (II.4.13)

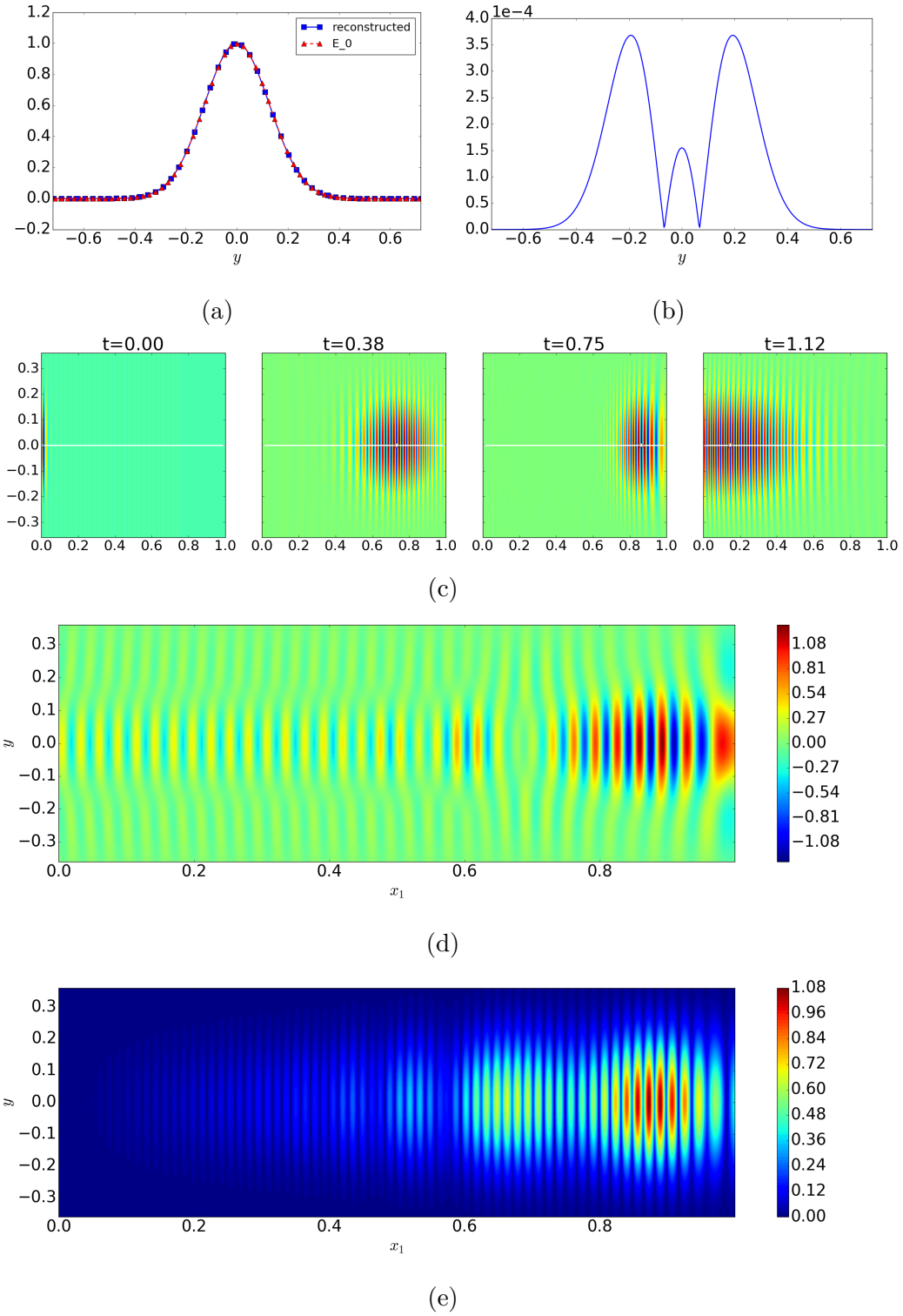

Figure II.4.11: (a) Launched beam and reconstructed boundary data, and (b) difference between the two. (c) Wave packet at different times and trajectory of the wave packet center (white line). (d) Reconstructed wave beam and (e) absolute value of the difference with respect to the exact solution.

II.4.6 Conservation of the Poynting flux

The results in Section II.3.4 provide useful information about the wave beam reconstructed with the method of Hagedorn wave packets. This information can be used as a diagnostic tool for the numerical tests presented in the previous sections. In particular, one expects that:

- The Poynting flux (II.3.32) is constant for the case of a constant or linear potential, being exactly zero for the latter.
- In the general case the identity (II.3.39) is satisfied instead.

II.4.6.1 Constant and linear potential

In Figure II.4.12 the Poynting flux (II.3.32) is plotted as a function of x_1 for two of the tests presented above, namely, the constant case with large R_y and the linear case with $\vartheta = 90°$. We can observe how the flux is constant, up to small oscillations whose amplitude can be reduced by increasing the resolution in both t and y. This confirms that for these cases the Hagedorn method is able to provide a correct numerical solution.

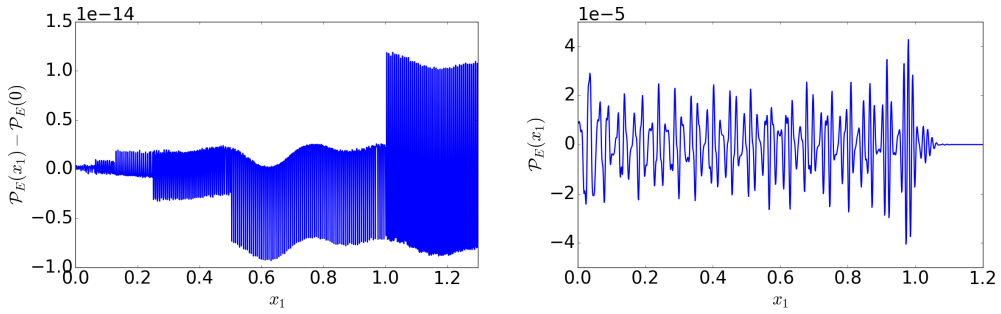

(a) (b)

Figure II.4.12: Poynting flux as a function of x_1 for the case of (a) constant and (b) linear potential, corresponding to the solutions represented in Figure II.4.1 and II.4.6, respectively.

II.4.6.2 Non-quadratic potential, $L = 0.09$

In the case of the non-quadratic potential (II.4.13) with short variation scale the numerical results (cf., Section II.4.5.3) were not at all satisfactory, and the structure of the Poynting flux confirms the fact that the reconstructed solution does not constitute a good solution of Helmholtz equation: a significant variation of the flux is present, as one can observe in Figure II.4.13a.

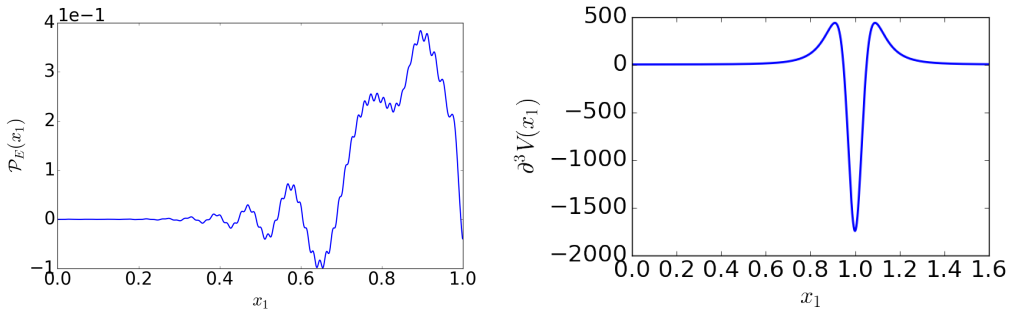

(a) (b)

Figure II.4.13: (a) Poynting flux of the reconstructed wave beam in the case of the non-quadratic potential V defined in II.4.13, with $L = 0.009$. The flux is not constant along the x_1-axis, and the reconstructed beam is not a solution of Helmholtz equation. (b) Third derivative of V. Notice that the large values of $\partial^3 V$ determine a larger variation in $\mathcal{P}_E$.

From a qualitative comparison between Figures II.4.13a, II.4.11e and II.4.7 it emerges that region where the numerical method fails coincides with the region where the potential starts increasing. In particular, in this region the difference between V and its quadratic approximation is large, as one can deduce observing the profile of the third derivative of V shown in Figure II.4.13b. To confirm the correlation between the inaccuracy of the numerical solution and the estimate on the variation of the Poynting flux given in equation (II.3.39), one may look at Figure II.4.14, where it is shown how both left- and right-hand side of (II.3.39) are non-trivial and they add to zero.

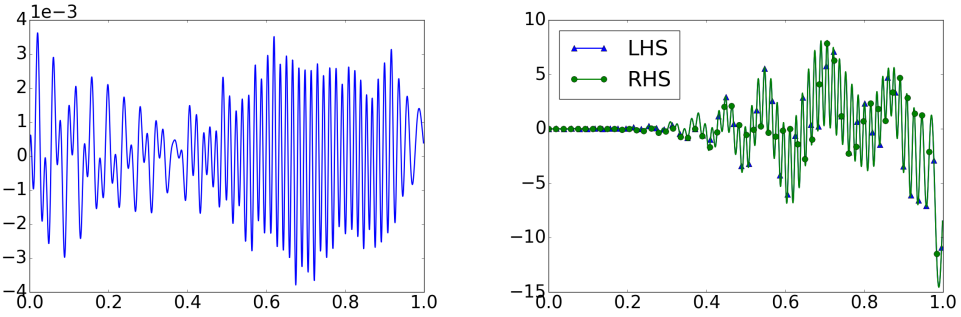

(a) (b)

Figure II.4.14: (a) The identity in (II.3.39) is verified with a certain accuracy (resolution dependent) by the Hagedorn solution in the case of a non-quadratic potential of the form (II.4.13). (b) Left- and right-hand side of (II.3.39) (LHS and RHS, respectively).

Remark II.4.6.1 (Exact solution)**.** *The reference solution used for this case is given by the asymptotic solution of the corresponding Helmholtz equation given in (II.3.44). The approximation error can actually be reabsorbed, and following the approach of Wasow [100] one can build an exact solution of (II.3.41a) in the form [42]*

$$E^{\kappa}(x) = \mathcal{F}^{-1}\Big\{ A\big[A_0^{\kappa}(x_1, N_y)\mathrm{Ai}(-\varphi(x_1, N_y)) + \kappa^{-2/3} A_1^{\kappa}(x_1, N_y)\mathrm{Ai}'(-\varphi(x_1, N_y))\big]. \tag{II.4.14}$$

For the case of interest to this work though, the asymptotic solution (II.3.44) is sufficiently accurate, and the analysis of the Poynting flux - which is conserved by the reference solution - fully explains the large difference with the reconstructed solution. Such difference comes therefore from the error in the Hagedorn solution of Schrödinger equation, which can be reduced in the future by constructing a more accurate approximation by adding higher-order wave packets.

II.5 Conclusions and outlook

In this part some initial results for the method of Hagedorn wave packets to reconstruct wave beams have been presented, in particular for what concerns wave beam solutions of Helmholtz equation in two dimensions. From the point of view of the envisaged applications, the presented results provide indeed motivation to pursue the research in the direction traced in this work. A possible agenda for future work is sketched in what follows.

Development of the theory

The results of Chapter II.3 are limited to Helmholtz equation in $2d$, and a complete statement could be done for the case of constant and linear potentials only. The only result for the more general case of a smooth increasing potential (cf., Proposition II.3.4) clearly indicates that more complex and realistic problems cannot be solved by means of a single wave packet. Therefore, using the approximation results presented in Chapter II.2, one could investigate how the approximation error on the solution of Schrödinger equation propagates to the reconstructed beam.

The next step would be to generalize the results obtained for Helmholtz equation to more physically relevant problems (for instance, equation I.2.1).

Development of the numerics

On the numerics side, so far no major effort was made to optimize the implementation. All steps - optimization of the initial condition, solution of the ODEs, time integration - can be addressed again with the intent of improving quality and efficiency. The `Python` prototype code is probably not the ideal

framework for optimal implementation, and in the future the method could be implemented in a compiled language. `Fortran` would be the natural choice, for compatibility reasons with most of the codes used in the fusion community. In particular, the analogies between the method of Hagedorn wave packets and beam tracing make it eligible for an implementation in the framework of TORBEAM [65]: one could equip the beam tracing code with a reflectometry-dedicated module, which implements the method of Hagedorn wave packets in a framework that allows for realistic tokamak simulations.

Acknowledgements

There is a number of people whom I feel thankful to, and therefore I would like to spend a few words for them, as this thesis would not exist without their scientific and human support:

- ⋆ I honestly think I couldn't have wished for a better supervision then the one given by my advisor Omar Maj, with his incredibly broad scientific knowledge and peerless kindness. His office door was always opened during these years, and I have never walked out of it on empty hands - bringing with me either the right reference I was looking for (usually Hörmander's book!), or some piece of code (ok, more than just "some"), or some smart ideas or interesting point of view on the work. I will always be thankful and probably never stop thinking that I learned from him only a small fraction of what I could have.

- ⋆ My sincere thankfulness goes to my supervisor Eric Sonnendrücker, who gave me the possibility to work at IPP in the first place, and always showed interest in my progress.

- ⋆ The collaboration with physicists from the institute was an enriching experience during these years, and I thank Emanuele Poli, Alf Köhn and Antti Snicker for the interesting discussions, which helped collocating the somewhat abstract maths in a real-world context. Hannes Weber also fully deserves a mention, as without his nicely written thesis life would have been way harder for me at the beginning.

- ⋆ I also would like to thank Brunello Tirozzi and Alessandro Cardinali, who first introduced me to nuclear fusion and plasma physics, and gave me the possibility to get a taste of how actual research works, when I was just a master student asking for some topic for his thesis.

On a personal level the list of people who sooner or later contributed to this achievement would require a thesis of its own, so I will stick to those who accompanied these last years I spent in Munich.

⋆ My parents Mauro and Daniela and my siblings Emiliano and Francesca are on top of the list: nonostante le diverse salite che avete (o abbiamo) dovuto affrontare in questi anni, ho sempre sentito il vostro sostegno, in ogni singola scelta, e spero che mi sentiate vicino anche solo una piccola parte di quanto io sento vicini voi. Così come sento sempre vicina mia nonna Franca, perché i Krapfen saranno anche buoni, ma senza le ricette per il tiramisù e la crostata vivere qui non sarebbe così facile!

⋆ This brings me to my roman-german family Daniele, Giorgia, Fulvio and Miriam: every single "pranzo della domenica" we share, with home-made "nonna food", makes Munich feel like home, and I wouldn't have gone through these years so easily without this feeling.

⋆ I feel lucky for having met a special person like Mustafa: I can't wait for you to start philosophising for hours about this thesis after reading half of the abstract! Lunch breaks with you and Edoardo made life at the office enjoyable even during difficult times.

⋆ A special mention goes to the Gypsy-Jazz family: you are the "bass" of this work, without you in the background this whole gig wouldn't have been possible.

⋆ Last (but only in order of appearance!) I am grateful for Sophia having entered the scene, and having switched the metronome of these last months from an enjoyable *andante* to a joyful *allegretto*.

Bibliography

[1] Aleynikov, P., and Marushchenko, N. 3d full-wave modelling and mode conversion in realistic w7-x plasmas. *EPJ Web of Conferences 149* (01 2017), 03007.

[2] Babic, V., Kuester, E., and Buldyrev, V. *Short-Wavelength Diffraction Theory: Asymptotic Methods*. Springer Series on Wave Phenomena. Springer Berlin Heidelberg, 2011.

[3] Babich, V. M. The construction of gaussian beams with exponentially small residual. *Journal of Mathematical Sciences 79*, 4 (Apr 1996), 1169–1171.

[4] Balakin, A. A., Bertelli, N., and Westerhof, E. Wave beam propagation through density fluctuations. *IEEE Transactions on Plasma Science 39*, 11 (Nov 2011), 3012–3013.

[5] Born, M., Wolf, E., Bhatia, A. B., Clemmow, P. C., Gabor, D., Stokes, A. R., Taylor, A. M., Wayman, P. A., and Wilcock, W. L. *Principles of Optics: Electromagnetic Theory of Propagation, Interference and Diffraction of Light*, 7 ed. Cambridge University Press, 1999.

[6] Bornatici, M., Cano, R., Barbieri, O. D., and Engelmann, F. Electron cyclotron emission and absorption in fusion plasmas. *Nuclear Fusion 23*, 9 (1983), 1153.

[7] Boyd, J. P. The devil's invention: Asymptotic, superasymptotic and

hyperasymptotic series. *Acta Applicandae Mathematica 56*, 1 (Mar 1999), 1–98.

[8] Brambilla, M. *Kinetic Theory of Plasma Waves: Homogeneous Plasmas*. International Series of Monographs on Physics. Clarendon Press, 1998.

[9] Brookman, M. W., Austin, M. E., and Petty, C. C. Finding evidence for density fluctuation effects on electron cyclotron heating deposition profiles on diii-d. *AIP Conference Proceedings 1689*, 1 (2015), 090005.

[10] Brookman, M. W., Austin, M. E., Gentle, K. W., Petty, C. C., Ernst, D. E., Peysson, Y., Decker, J., and Barada, K. Experimental measurement of ech deposition broadening: Beyond anomalous transport. *EPJ Web Conf. 147* (2017), 03001.

[11] Chellaï, O., Alberti, S., Baquero-Ruiz, M., Furno, I., Goodman, T., Labit, B., Maj, O., Ricci, P., Riva, F., Guidi, L., Poli, E., and the TCV team. Millimeter-wave beam scattering by edge-plasma density fluctuations in tcv. *Plasma Physics and Controlled Fusion 61*, 1 (2019), 014001.

[12] Chellaï, O., Alberti, S., Baquero-Ruiz, M., Furno, I., Goodman, T., Manke, F., Plyushchev, G., Guidi, L., Koehn, A., Maj, O., Poli, E., Hizanidis, K., Figini, L., and Ricci, D. Millimeter-wave beam scattering by field-aligned blobs in simple magnetized toroidal plasmas. *Phys. Rev. Lett. 120* (Mar 2018), 105001.

[13] Chib, S., and Greenberg, E. Understanding the metropolis-hastings algorithm. *The American Statistician 49*, 4 (1995), 327–335.

[14] Conway, G., Angioni, C., Dux, R., Ryter, F., Peeters, A., Schirmer, J., Troester, C., Group, C. R., and the ASDEX

Upgrade team. Observations on core turbulence transitions in asdex upgrade using doppler reflectometry. *Nuclear Fusion 46*, 9 (2006), S799.

[15] Da Silva, F., Campos Pinto, M., Després, B., and Heuraux, S. Stable explicit coupling of the yee scheme with a linear current model in fluctuating magnetized plasmas. *Journal of Computational Physics 295* (04 2015).

[16] Da Silva, F., Heuraux, S., Ribeiro, T., and Scott, B. Development of a 2d full-wave je-fdtd maxwell x-mode code for reflectometry simulation. *Proceedings of the 9th International Reflectometry Workshop (IRW9)* (2009).

[17] Duistermaat, J. *Fourier Integral Operators*, vol. 130 of *Progress in Mathematics*. Birkhäuser, 1996.

[18] Duistermaat, J. J. Oscillatory integrals, lagrange immersions and unfolding of singularities. *Communications on Pure and Applied Mathematics 27*, 2 (1974), 207–281.

[19] Faou, E., Lubich, C., and Gradinaru, V. Computing semiclassical quantum dynamics with Hagedorn wavepackets. *SIAM Journal on Scientific Computing 31*, 4 (2009), 3027–3041.

[20] Farina, D. A quasi-optical beam-tracing code for electron cyclotron absorption and current drive: Gray. *Fusion Science and Technology 52*, 2 (2007), 154–160.

[21] Freidberg, J. P. *Plasma Physics and Fusion Energy*. Cambridge University Press, 2007.

[22] Gérard, P., Markowich, P. A., Mauser, N. J., and Poupaud, F. Homogenization limits and wigner transforms. *Communications on Pure and Applied Mathematics 50*, 4 (1997), 323–379.

[23] Guidi, L., Maj, O., Weber, H., Köhn, A., Snicker, A., and Poli, E. Cross-polarization scattering of diffracting electron-cyclotron beams in a turbulent plasma with the wkbeam code. *Journal of Physics: Conference Series 1*, 775 (2016), 012005.

[24] Hagedorn, G. A. Semiclassical quantum mechanics. i. the $\hbar \to 0$ limit for coherent states. *Comm. Math. Phys. 71*, 1 (1980), 77–93.

[25] Hagedorn, G. A. Semiclassical quantum mechanics. iii. the large order asymptotics and more general states. *Annals of Physics 135*, 1 (1981), 58 – 70.

[26] Hagedorn, G. A. Raising and lowering operators for semiclassical wave packets. *Annals of Physics 269*, 1 (1998), 77 – 104.

[27] Hartfuss, H., and Geist, T. *Fusion Plasma Diagnostics with mm-Waves: An Introduction*. EBL-Schweitzer. Wiley, 2013.

[28] Henderson, M., Heidinger, R., Strauss, D., Bertizzolo, R., Bruschi, A., Chavan, R., Ciattaglia, E., Cirant, S., Collazos, A., Danilov, I., Dolizy, F., Duron, J., Farina, D., Fischer, U., Gantenbein, G., Hailfinger, G., Kasparek, W., Kleefeldt, K., Landis, J.-D., Meier, A., Moro, A., Platania, P., Plaum, B., Poli, E., Ramponi, G., Saibene, G., Sanchez, F., Sauter, O., Serikov, A., Shidara, H., Sozzi, C., Spaeh, P., Udintsev, V., Zohm, H., and Zucca, C. Overview of the iter ec upper launcher. *Nuclear Fusion 48*, 5 (2008), 054013.

[29] Henderson, M., Saibene, G., Darbos, C., Farina, D., Figini, L., Gagliardi, M., Gandini, F., Gassmann, T., Hanson, G., Loarte, A., Omori, T., Poli, E., Purohit, D., and Takahashi, K. The targeted heating and current drive applications for the iter electron cyclotron system. *Physics of Plasmas 22*, 2 (2015), 021808.

[30] Hörmander, L. *The analysis of linear partial differential operators I.* Classics in Mathematics. Springer-Verlag, 2003.

[31] Igochine, V. *Active Control of Magneto-hydrodynamic Instabilities in Hot Plasmas.* Springer Series on Atomic, Optical, and Plasma Physics. Springer Berlin Heidelberg, 2016.

[32] International Energy Agency. Key world energy statistics. *https://www.iea.org/publications/freepublications/publication/KeyWorld2017.pdf* (2018).

[33] Ioannidis, Z. C., Ram, A. K., Hizanidis, K., and Tigelis, I. G. Computational studies on scattering of radio frequency waves by density filaments in fusion plasmas. *Physics of Plasmas 24*, 10 (2017), 102115.

[34] ITER. https://www.iter.org.

[35] Karal, F. C., and Keller, J. B. Elastic, electromagnetic, and other waves in a random medium. *Journal of Mathematical Physics 5*, 4 (1964), 537–547.

[36] Kasparek, W., Doelman, N., Stober, J., Maraschek, M., Zohm, H., Monaco, F., Eixenberger, H., Klop, W., Wagner, D., Schubert, M., Schütz, H., Grünwald, G., Plaum, B., Munk, R., Schlüter, K., and Team, A. U. Ntm stabilization by alternating o-point ec current drive using a high-power diplexer. *Nuclear Fusion 56*, 12 (2016), 126001.

[37] Köhn, A., Cappa, A., Holzhauer, E., Castejòn, F., Fernández, A., and Stroth, U. Full-wave calculation of the o–x–b mode conversion of gaussian beams in a cylindrical plasma. *Plasma Physics and Controlled Fusion 50*, 8 (2008), 085018.

[38] Kravtsov, Y. A., and Orlov, Y. I. *Geometrical Optics of Inhomogeneous Media.* Springer Berlin Heidelberg, 1990.

[39] Köhn, A., Guidi, L., Holzhauer, E., Maj, O., Poli, E., Snicker, A., and Weber, H. Microwave beam broadening due to turbulent plasma density fluctuations within the limit of the born approximation and beyond. *Plasma Physics and Controlled Fusion 60*, 7 (2018), 075006.

[40] Köhn, A., Holzhauer, E., Leddy, J., Thomas, M. B., and Vann, R. G. L. Influence of plasma turbulence on microwave propagation. *Plasma Physics and Controlled Fusion 58*, 10 (2016), 105008.

[41] La Haye, R. J. Neoclassical tearing modes and their control. *Physics of Plasmas 13*, 5 (2006), 055501.

[42] Lafitte, O. Private communication, 2018.

[43] Lapeyre, B., Pardoux, E., and Sentis, R. *Introduction to Monte Carlo Methods for Transport and Diffusion Equations*. Oxford texts in applied and engineering mathematics. Oxford University Press, 2003.

[44] Lasser, C., and Troppmann, S. Hagedorn wavepackets in time-frequency and phase space. *Journal of Fourier Analysis and Applications 20*, 4 (Aug 2014), 679–714.

[45] Laviron, C., Donné, A. J. H., Manso, M. E., and Sanchez, J. Reflectometry techniques for density profile measurements on fusion plasmas. *Plasma Physics and Controlled Fusion 38*, 7 (1996), 905.

[46] Liu, H., Ralston, J., Runborg, O., and Tanushev, N. M. Gaussian beam methods for the helmholtz equation. *SIAM Journal on Applied Mathematics 74*, 3 (2014), 771–793.

[47] Lubich, C. *From Quantum to Classical Molecular Dynamics: Reduced Models and Numerical Analysis*. Zurich lectures in advanced mathematics. European Mathematical Society, 2008.

[48] Maj, O. The relationship between the wigner-weyl kinetic formalism and the complex geometrical optics method. *Journal of Mathematical Physics 46*, 8 (2005), –.

[49] Maj, O., Mariani, A., Poli, E., and Farina, D. The wave energy flux of high frequency diffracting beams in complex geometrical optics. *Physics of Plasmas 20*, 4 (2013), 042122.

[50] Maj, O., Pereverzev, G. V., and Poli, E. Validation of the paraxial beam-tracing method in critical cases. *Physics of Plasmas 16*, 6 (2009), 062105.

[51] Manso, M. E. Reflectometry in fusion devices. *Plasma Physics and Controlled Fusion 35*, SB (1993), B141.

[52] Martinez, A. *An Introduction to Semiclassical and Microlocal Analysis*. CMS Books in Mathematics. Springer, 2002.

[53] Maslov, V., and Fedoriuk, M. *Semi-Classical Approximation in Quantum Mechanics*. Mathematical Physics and Applied Mathematics. Dordrecht, 1981.

[54] Maslov, V. P. *The Complex WKB Method for Nonlinear Equations I: Linear Theory*. Birkhser, Basel, 1994.

[55] McDonald, S. W. Phase-space representations of wave equations with applications to the eikonal approximation for short-wavelength waves. *Physics Reports 158*, 6 (1988), 337 – 416.

[56] McDonald, S. W. Wave kinetic equation in a fluctuating medium. *Phys. Rev. A 43*, 8 (Apr 1991), 4484–4499.

[57] McDonald, S. W., and Kaufman, A. N. Weyl representation for electromagnetic waves: The wave kinetic equation. *Phys. Rev. A 32* (Sep 1985), 1708–1713.

[58] Monk, P. *Finite Element Methods for Maxwell's equations*. Numerical Mathematics and Scientific Computation. Oxford Science Publications, 2003.

[59] Nelder, J. A., and Mead, R. A simplex method for function minimization. *The Computer Journal 7*, 4 (1965), 308–313.

[60] numpy.trapz. https://docs.scipy.org/doc/numpy-1.14.0/reference/generated/numpy.trapz.html.

[61] Pereverzev, G. V. Paraxial wkb solution of a scalar wave equation. *IPP Report 4/260* (1996).

[62] Pereverzev, G. V. Beam tracing in inhomogeneous anisotropic plasmas. *Physics of Plasmas 5*, 10 (1998), 3529–3541.

[63] Permitin, G., and Smirnov, A. Quasioptics of smoothly inhomogeneous isotropic media. *Journal of Experimental and Theoretical Physics 82*, 3 (1996), 395.

[64] Peysson, Y., Decker, J., Morini, L., and Coda, S. Rf current drive and plasma fluctuations. *Plasma Physics and Controlled Fusion 53*, 12 (2011), 124028.

[65] Poli, E., Bock, A., Lochbrunner, M., Maj, O., Reich, M., Snicker, A., Stegmeir, A., Volpe, F., Bertelli, N., Bilato, R., Conway, G., Farina, D., Felici, F., Figini, L., Fischer, R., Galperti, C., Happel, T., Lin-Liu, Y., Marushchenko, N., Mszanowski, U., Poli, F., Stober, J., Westerhof, E., Zille, R., Peeters, A., and Pereverzev, G. Torbeam 2.0, a paraxial beam tracing code for electron-cyclotron beams in fusion plasmas for extended physics applications. *Computer Physics Communications 225* (2018), 36 – 46.

[66] Poli, E., Peeters, A., and Pereverzev, G. Torbeam, a beam tracing code for electron-cyclotron waves in tokamak plasmas. *Computer Physics Communications 136*, 1-2 (2001), 90 – 104.

[67] Prater, R. Heating and current drive by electron cyclotron waves. *Physics of Plasmas 11*, 5 (2004), 2349–2376.

[68] Prater, R., Farina, D., Gribov, Y., Harvey, R., Ram, A., Lin-Liu, Y.-R., Poli, E., Smirnov, A., Volpe, F., Westerhof, E., Zvonkov, A., and the ITPA Steady State Operation Topical Group. Benchmarking of codes for electron cyclotron heating and electron cyclotron current drive under iter conditions. *Nuclear Fusion 48*, 3 (2008).

[69] Ralston, J. V. On the construction of quasimodes associated with stable periodic orbits. *Comm. Math. Phys. 51*, 3 (1976), 219–242.

[70] Ram, A. K., and Hizanidis, K. Scattering of radio frequency waves by cylindrical density filaments in tokamak plasmas. *Physics of Plasmas 23*, 2 (2016), 022504.

[71] Ramponi, G., Farina, D., Henderson, M., Poli, E., Sauter, O., Saibene, G., Zohm, H., and Zucca, C. Physics analysis of the iter ecw system for optimized performance. *Nuclear Fusion 48*, 5 (2008), 054012.

[72] Rauch, J. *Hyperbolic Partial Differential Equations and Geometric Optics*. Graduate studies in mathematics. American Mathematical Society, 2012.

[73] Richardson, A. S., Bonoli, P. T., and Wright, J. C. The lower hybrid wave cutoff: A case study in eikonal methods. *Physics of Plasmas 17*, 5 (2010), 052107.

[74] Rudin, W. *Real and Complex Analysis*. Higher Mathematics Series. McGraw-Hill, 1974.

[75] Ryzhik, L., Papanicolaou, G., and Keller, J. B. Transport equations for elastic and other waves in random media. *Wave Motion 24*, 4 (1996), 327 – 370.

[76] Sakharov, A. S. Two-dimensional full-wave simulation of propagation and absorption of a microwave beam in magnetized plasma. *Journal of Physics: Conference Series 1094*, 1 (2018), 012011.

[77] Sauter, O., Henderson, M. A., Ramponi, G., Zohm, H., and Zucca, C. On the requirements to control neoclassical tearing modes in burning plasmas. *Plasma Physics and Controlled Fusion 52*, 2 (2010), 025002.

[78] scipy.integrate.ode. https://docs.scipy.org/doc/scipy-0.18.1/reference/generated/scipy.integrate.ode.html.

[79] scipy.optmize.minimize. https://docs.scipy.org/doc/scipy/reference/generated/scipy.optimize.minimize.html.

[80] Scott, D. W. *Multivariate density estimation: theory, practice, and visualization*. John Wiley & Sons, 2015.

[81] Sebelin, E., Peysson, Y., Litaudon, X., Moreau, D., Miellou, J., and Lafitte, O. Uniqueness and existence result around lax-milgram lemma: application to electromagnetic waves propagation in tokamak plasmas. *INIS report EUR-CEA-FC* (1997), –1609.

[82] Smith, G. R., Cook, D. R., Kaufman, A. N., Kritz, A. H., and McDonald, S. W. Scattering of ordinary mode electromagnetic waves by density fluctuations in tokamaks. *Physics of Fluids B: Plasma Physics 5*, 12 (1993), 4299–4311.

[83] Snicker, A., Poli, E., Maj, O., Guidi, L., Köhn, A., Weber, H., Conway, G., Henderson, M., and Saibene, G. The effect of density fluctuations on electron cyclotron beam broadening and implications for iter. *Nuclear Fusion 58*, 1 (2018), 016002.

[84] Snicker, A., Poli, E., Maj, O., Guidi, L., Köhn, A., Weber, H., Conway, G. D., Henderson, M., and Saibene, G. Interaction of the electron density fluctuations with electron cyclotron waves from the equatorial launcher in iter. *Plasma Physics and Controlled Fusion 60*, 1 (2018), 014020.

[85] Spanier, J., and Gelbard, E. *Monte Carlo Principles and Neutron Transport Problems*. Dover Books on Mathematics Series. Dover Publications, 2008.

[86] Stegmeir, A., Conway, G., Poli, E., and Strumberger, E. Analysis of the iter low field side reflectometer employing the beam tracing method. *Fusion Engineering and Design 86*, 12 (2011), 2928 – 2942.

[87] Stern, A., Tong, Y., Desbrun, M., and E. Marsden, J. Variational integrators for maxwell's equations with sources. *PIERS Online 4* (04 2008).

[88] Stix, T. *Waves in Plasmas*. American Inst. of Physics, 1992.

[89] Swanson, D. *Plasma Waves, 2nd Edition*. Series in Plasma Physics. Taylor & Francis, 2003.

[90] Sysoeva, E., da Silva, F., Gusakov, E., Heuraux, S., and Popov, A. Electron cyclotron resonance heating beam broadening in the edge turbulent plasma of fusion machines. *Nuclear Fusion 55*, 3 (2015).

[91] Tao, T. *An Introduction to Measure Theory*. Graduate studies in mathematics. American Mathematical Society, 2011.

[92] Taylor, M. *Pseudodifferential Operators and Nonlinear PDE*. Progress in Mathematics. Birkhäuser Boston, 2012.

[93] TCV. http://spc.epfl.ch/research_TCV_Tokamak.

[94] TORPEX. http://spc.epfl.ch/research_basic_plasmas_torpex.

[95] Tracy, E., Brizard, A., Richardson, A., and Kaufman, A. *Ray Tracing and Beyond: Phase Space Methods in Plasma Wave Theory.* Cambridge University Press, 2014.

[96] Tsironis, C., Peeters, A. G., Isliker, H., Strintzi, D., Chatziantonaki, I., and Vlahos, L. Electron-cyclotron wave scattering by edge density fluctuations in iter. *Physics of Plasmas 16*, 11 (2009), 112510.

[97] Upgrade, A. https://www.ipp.mpg.de/16195/asdex.

[98] Villani, C. *Hypocoercivity.* Memoirs of the American Mathematical Soc. American Mathematical Soc., 2009.

[99] Wagner, D. H., Stober, J. K., Leuterer, F., Sips, G., Grunwald, G., Monaco, F., Munich, M. J., Poli, E., Schutz, H., Volpe, F., Treutterer, W., Zohm, H., Franke, T., Thumm, M., Heidinger, R., Gantenbein, G., Meier, A., Kasparek, W., Lechte, C., Litvak, A. G., Denisov, G. G., Chirkov, A., Tai, E., Popov, L., Nichiporenko, V., Myasnikov, V., Solyanova, E., and Malygin, S. Progress and first results with the new multifrequency ecrh system for asdex upgrade. *IEEE Transactions on Plasma Science 37*, 3 (2009), 395–402.

[100] Wasow, W. *Linear Turning Point Theory.* No. v. 54 in Applied Mathematical Sciences. Springer New York, 1985.

[101] Weber, H. Propagation of high-frequency waves in a fluctuating plasma. *IPP Report 5/134* (2013).

[102] Weber, H., Maj, O., and Poli, E. Scattering of diffracting beams of electron cyclotron waves by random density fluctuations in inhomogeneous plasmas. *EPJ Web of Conferences 87* (2015).

[103] Wesson, J., and Campbell, D. *Tokamaks*. International Series of Monographs on Physics. OUP Oxford, 2011.

[104] Westerhof, E. Requirements on heating or current drive for tearing mode stabilization by current profile tailoring. *Nuclear Fusion 27*, 11 (1987), 1929.

[105] Yee, K. Numerical solution of initial boundary value problems involving maxwell's equations in isotropic media. *IEEE Transactions on Antennas and Propagation 14*, 3 (May 1966), 302–307.

[106] Zohm, H., Gantenbein, G., Leuterer, F., Manini, A., Maraschek, M., Yu, Q., and the ASDEX Upgrade Team. Control of mhd instabilities by eccd: Asdex upgrade results and implications for iter. *Nuclear Fusion 47*, 3 (2007), 228.

[107] Zweben, S. J., Boedo, J. A., Grulke, O., Hidalgo, C., LaBombard, B., Maqueda, R. J., Scarin, P., and Terry, J. L. Edge turbulence measurements in toroidal fusion devices. *Plasma Physics and Controlled Fusion 49*, 7 (2007), S1.